Transport of plastic pollution by ocean waves

Ross Calvert

New College

University of Oxford

A thesis submitted for the degree of

Doctor of Philosophy

Trinity 2020

In memory of Mum

Acknowledgements

I would like to express appreciation for my supervisors Prof. Ton van den Bremer and Prof. Alistair Borthwick who have not just offered academic guidance, but all round support, encouragement and understanding on many levels. Their expert knowledge certainly guided the work in this thesis, but their kindness and empathy has been essential to me finishing it. I'm grateful to all of my family, my parents and siblings, who along the way have heard me moan and celebrate, sometimes in the same breath. Special thanks goes to; Jess, for the support and important supplier of silliness and belly laughs that kept me sane; Sacha without your support I wouldn't be finishing this and without the adventures I wouldn't have been as happy or productive, and; all of Pyroceltica as a collective, for getting me out of my head. I extend huge thanks to all those who have listened to me talk about things I wasn't even sure if I understood yet.

Abstract

Ocean waves are one of the drivers of ocean transport of floating and submerged particles, including microplastics, oil droplets, sediment, and wreckage. This thesis examines the wave-induced transport of purely Lagrangian particles by wave packets and the effect of changing size and density of floating objects on their transport by regular waves. Particle tracking velocimetry is used to examine Lagrangian particle trajectories under deep-water wave packets in a laboratory flume. Particle motions are dominated by Stokes drift near the free surface, and the Eulerian return flow at depth. Close agreement is achieved between experimental measurements and leading-order solutions of the irrotational water wave equations. A multiple-scales solution is derived for Eulerian mean flow under wave packets that applies to all water depths. The solution is validated against experimental data, using particle tracking velocimetry corrected for background and paddle wave generation errors. It is found that the magnitude of the horizontal return flow is enhanced by divergence of the Stokes transport at wave packet scale and the confining effect of the mean set-down underneath the packet. This enhanced return flow has potentially large ramifications for the transport of particles in coastal waters. A combination of analytical, numerical and experimental approaches are used to examine the transport of inertial, spherical objects (representing large marine debris) by Stokes drift in regular waves. It is found that such objects are transported at different rates depending on their size and density, and that larger objects experience increased drift compared with Lagrangian tracers. The mechanism for increased drift comprises the variable submergence and the corresponding dynamic buoyancy force components in the direction perpendicular to the local water surface, which leads to an amplification of Stokes drift when averaged over the wave cycle. Using an expansion in wave steepness, a closed-form approximation is derived for this increased drift, which can be included in ocean-scale models of marine litter transport.

Contents

0.1 Background 9

0.1.1 Stokes drift and Eulerian return flow 11

0.1.2 Extension to finite depth 12

0.1.3 Drift of large floating marine debris 13

0.2 Aims and Objectives 14

0.2.1 Aim 14

0.2.2 Objectives 14

0.3 Layout and author's contribution 15

0.3.1 Author's contribution 16

1 Stokes drift and Eulerian mean flow under deep-water wave packets 17

1.1 Introduction 18

1.2 Irrotational water wave theory for wave groups 22

1.2.1 Governing equations and leading-order solutions 22

1.2.2 Net Lagrangian displacements 24

1.3 Experimental methodology 26

1.3.1 Set-up, wave generation and data acquisition 26

1.3.2 Matrix of experiments 28

1.3.3 Data processing and removal of background motion . . . 30

1.4 Results 31

1.4.1 Particle trajectories 31

1.4.2 Net Lagrangian displacements 33
1.4.3 Repeatability 36
1.5 Conclusions 36

Appendices 39

1.A Measured free surface elevation signals 39
1.B Experimental procedure and data processing 39
1.B.1 Camera settings and calibration 39
1.B.2 Image processing and particle tracking 40
1.B.3 Removal of background motion 41

2 Eulerian mean flow under finite-depth wave packets 42

2.1 Introduction 43
2.2 Second-order theory 48
2.2.1 Governing equations 48
2.2.2 Solutions using perturbation methods 48
2.2.3 Lagrangian displacements 52
2.3 Experimental methodology 55
2.3.1 Setup and data acquisition 55
2.3.2 Wave generation 56
2.3.3 Matrix of experiments 57
2.3.4 Data processing and removal of background motion . . . 57
2.4 Results 60
2.4.1 The subharmonic free-surface elevation: Set-down and error waves 60
2.4.2 Particle trajectories 62
2.4.3 Horizontal Lagrangian displacements 64
2.5 Conclusions 66

Appendices 70

2.A Analysis of poles in wave-number integral 70

2.B Comparison with existing literature 70

2.B.1 Shallow return flow: $k_0 d = O(1)$ and $d/\sigma \ll 1$ 70

2.B.2 Deep return flow: $k_0 d \gg 1$ and $d/\sigma \gg 1$ 71

2.C Trajectory processing 72

2.D Vertical Lagrangian displacements 73

3 Mechanism for the increased transport of large floating marine debris 75

3.1 Introduction 76

3.2 Mathematical model 79

3.2.1 Equation of motion of a floating object 79

3.2.2 Fluid velocity for surface gravity waves 86

3.3 Perturbation theory for viscous drag 86

3.3.1 Zeroth-order in wave steepness: $\mathcal{O}(\alpha^0)$ 87

3.3.2 First-order in wave steepness: $\mathcal{O}(\alpha^1)$ 88

3.3.3 Second-order in wave steepness: $\mathcal{O}(\alpha^2)$ 92

3.3.4 Limitation on validity of viscous drag 98

3.4 Numerical solutions 98

3.4.1 Viscous drag 99

3.4.2 Non-viscous drag 99

3.5 Wave flume experiments 102

3.5.1 Set-up and data acquisition 102

3.5.2 Matrix of experiments 104

3.5.3 Data processing 105

3.6 Comparison between theory and experiments 107

3.6.1 First-order in wave steepness: $\mathcal{O}(\alpha)$ 107

3.6.2 Second-order in wave steepness: $\mathcal{O}(\alpha)$ 109

3.7 Conclusions 109

Appendices **113**

3.A Equations of motion 113

3.B Wavepackets vs. periodic waves 114

3.C Limiting behaviour of the numerical solutions 114

3.C.1 The Lagrangian limit 116

3.C.2 Small-object limit 116

4 Conclusions and recommendations **118**

4.1 Conclusions 118

4.1.1 General conclusions 118

4.1.2 Stokes drift and Eulerian mean flow under deep-water wave packets 118

4.1.3 Extension to arbitrary depth 119

4.1.4 Mechanism for the increased transport of large floating marine debris 120

4.2 Impact of research 121

4.3 Recommendations for future work 121

Introduction

0.1 Background

An understanding of the transport of floating or suspended solid pollutants in the ocean is important for many applications including the clean-up of plastics, removal of debris, mitigation of oil spills, and in directing search and rescue missions seeking wreckage and survivors of marine disasters. Several mechanisms play a role in transporting contaminated material in the ocean, including currents, wind, surface and internal waves, thermal upwelling and/or downwelling, salinity gradients, and turbulence. This thesis will address one of these modes of transport: the transport of floating or suspended solid objects by waves in the ocean.

Plastic pollution of the ocean has quickly become one of the largest environmental issues worldwide [Eriksen et al., 2014], causing particular issues for marine eco-systems [Law, 2017]. The longevity of plastic waste material in the ocean [Andrady, 2011] and the buoyancy of a large proportion of plastic particles [Geyer et al., 2017] enable such particles to travel very large distances. The calculated global budget of floating plastic pollution in the ocean, estimated at less than 0.3 million tonnes [van Sebille et al., 2015, Cózar et al., 2014, Eriksen et al., 2014] is orders of magnitude less than the predicted plastic that enters the sea, 5-12 million tonnes yr^{-1} [Jambeck et al., 2015]. The trend over the last few decades in field measurements of plastic in the ocean [Lebreton et al., 2019, Ostle et al., 2019, Wilcox et al., 2019] does not follow the increase in plastic production [Goldstein et al., 2012, Geyer et al., 2017].

Ocean surface gravity waves are generated when wind blows over the sea surface. At any time and location, the wave field comprises a superposition of waves generated earlier and at different locations. Wave models, such as

WaveWatch III [Tolman et al., 2009] can predict the propagation and strength of waves, allowing successful estimation of wave-induced transport [Webb and Fox-Kemper, 2011, Breivik et al., 2014].

Wave motion is predominately forwards and backwards, as can be seen when an object floats on the ocean surface. However, the orbits traced by this motion do not quite close. This is because the forward velocity under the crest, where slightly more time is spent in the orbit, is larger than the return velocity under the trough of the wave. This creates a net drift (first defined by Stokes [1847], and thus called Stokes drift). Although the concept of Stokes drift is very well established, there is still debate as to how observable it is in the laboratory Monismith et al. [2007], a debate this thesis aims to resolve for wave packets.

For wave packets an Eulerian return flow is driven by divergence of Stokes drift and not by a no-flow boundary condition, as is the case for the undertow or rip currents in the coastal region. The undertow is a return flow required to balance the onshore momentum-flux of Stokes drift towards the shore bounded by the beach [Svendsen, 1984]. The undertow passes under the surface-bound Stokes drift resulting in an increased likelihood that larger plastic objects move on-shore, whereas smaller plastic objects, that can be driven under the surface by wave-turbulence, are more likely to be moved off-shore by the undertow [Isobe et al., 2014, Kataoka and Hinata, 2015]. Pasternak et al. [2018] reported that plastic bottles are more likely to be found within the surf zone than outside. Rip-currents are wave-induced currents that arise in the surf zone and flow seaward, growing in the breaking zone, and can extend all the way to the inner shelf. A balance between shore-ward momentum flux and rip-currents can trap floating material in the surf-zone [MacMahan et al., 2010, Fujimura et al., 2014].

Stokes drift is the most significant wave-induced transport mechanism, and scales with the wave amplitude squared and decays with depth. In the ocean, wave amplitude is irregular and so Stokes drift is different at different locations corresponding to changes in wave height. If wave height were to be formulated as an envelope that first increases, reaches a maximum, and then decreases, the resultant Stokes drift would be divergent. Water is incompressible and so this divergence in Stokes drift has to be physically balanced. In ocean waves, the balance is achieved by a return flow in the opposite direction to wave propagation, and which becomes more dominant as the depth increases. This Eulerian return flow can also transport pollution, crucially in the opposite direction to Stokes drift. Experimentally validated, analytical solutions for the transport by Stokes drift and Eulerian mean flow would greatly inform the debate how waves induce the transport of floating and suspended objects in the ocean.

Given that Stokes drift and Eulerian return flow are the mechanisms by which waves induce transport in the open ocean, these mechanisms can be used to show how a purely Lagrangian tracer would be transported under wave action. If a particle of pollution is very small and of the same density as water then the particle will behave as a Lagrangian tracer. However, as a particle grows in size and/or changes in density its behaviour may deviate from that of a tracer. If an object is positively buoyant, it will float on the free surface. Waves then exert forces on the floating object whose response is defined by its inertial and other properties. It is obviously important to establish exactly how the properties of an object change its wave-induced transport.

Note that the background discussion here is deliberately brief because further details are given at the start of each of the relevant chapters.

0.1.1 Stokes drift and Eulerian return flow

As mentioned above, Lagrangian particles undergoing oscillatory motion beneath surface gravity waves also experience a net drift in the direction of wave propagation called Stokes drift [Stokes, 1847]. For wave packets, Stokes drift becomes divergent at packet scale and induces a Eulerian return flow [Longuet-Higgins and Stewart, 1962b]. The total Lagrangian velocity is the sum of Stokes drift and the induced Eulerian flow.

In the ocean, Stokes drift can provide a significant contribution to the trajectories of drifters [Röhrs et al., 2012] and must be accounted for in search and recovery missions, an example being the search for debris from the presumed location of the 2014 MH370 airplane crash [Trinanes et al., 2016]. Stokes drift can be important in the local modelling of oil spills [Christensen and Terrile, 2009, Drivdal et al., 2014, Jones et al., 2016]. In the near-surface transport and dispersion of plastic pollution, Stokes drift plays a potentially important yet largely unexplored role (e.g. Lebreton et al. [2018]). Furthermore, Stokes drift contributes to global ocean circulation [McWilliams and Restrepo, 1999, Belcher et al., 2012], Langmuir turbulence [Craik and Leibovich, 1976, D'Asaro et al., 2014, Sullivan and McWilliams, 2010] and sub-mesoscale ocean instability [Haney et al., 2015, McWilliams, 2016].

Experimentally, many authors have considered Stokes drift in laboratory wave flumes. As a visual illustration, van Dyke's (1982) *Album of Fluid Motion* reproduces Wallet and Ruellan's 1950 seminal image of orbits that do not quite close. Yet, there remains disagreement in the literature as to whether a net drift should be observed (see the discussion in Monismith et al. [2007], Weber [2011], Grue and Kolaas [2017], van den Bremer and Breivik [2017] and Deike et al. [2017]).

An experimental study of Lagrangian trajectories and transport by unidirectional, deep-water, small-amplitude, short-length yet quasi-monochromatic surface gravity wave packets is presented in Chapter 1. In doing so, the first (to the author's knowledge) experimental visualization of wave-induced Eulerian return flow for groups is presented. It is also shown that the experimental observations in this regime are in good agreement with leading-order solutions to the irrotational water wave equations. The experiments using short-length groups in an otherwise quiescent flume have the advantage of not generating a closed-flume return flow. This induced flow may transport vorticity, which is potentially unstable, and difficult to control experimentally. Furthermore, the experiments demonstrate the existence of a vertical component to the Stokes drift. This vertical component only exists for wave groups and results in a positive (temporary) vertical particle displacement underneath the centre of the group. This positive vertical displacement by the Stokes drift has been predicted by Herbers and Janssen [2016], illustrating that the set-down of the wave-averaged free surface in Eulerian records can appear as (significant) set-up in Lagrangian (buoy) records.

0.1.2 Extension to finite depth

Although set-down can be ignored in sufficiently deep water [McIntyre, 1981], the set-down of the wave-averaged free surface becomes important when the water depth is finite. Ignoring set-down or incorrectly reproducing it in numerical or laboratory experiments has been shown to lead to incorrect predictions of run-up on beaches [Orszaghova et al., 2014]. Generation of wave packets using linearly controlled wave paddles leads to spurious 'error waves' at the scale of the group. These erroneous waves travel ahead of the wave packet as free waves, typically at the shallow-water phase velocity in laboratory flumes [Whittaker et al., 2017] (see also the discussion by Nielsen and Baldock [2010], Orszaghova et al. [2014]). Second-order wave generation, where sub-harmonic frequencies represent the correct generation of the mean flow and the set-down of the wave-averaged free surface, has been proposed to remedy this [Schäffer, 1996, Leeuwen and Klopman, 1996]. However, implementation of second-order wave generation can be limited by the requirement of a large paddle stroke at the scale of the group [Whittaker et al., 2017].

Historically, several approaches have been taken to derive analytical solutions for the mean flow and the wave-averaged free surface under wave packets. These solutions can be classified on the basis of two scales: the water depth d relative to carrier wavelength, namely $k_0 d$ with k_0 denoting the carrier wavenumber, and the water depth relative to packet length, namely d/σ with σ denoting the packet length scale.

A new analytical solution to the Eulerian mean flow under small-steepness, narrow-banded wave packets is presented in chapter 2. The solution is shown to recover the results in all previous literature when the appropriate assumptions are made and is valid for all water depths. The Eulerian mean flow has then been validated using laboratory wave flume particle tracking velocimetry experiments.

0.1.3 Drift of large floating marine debris

Various studies have found that inertia and shape have an effect on the settling velocity of fully submerged particles. Eames [2008] and Santamaria et al. [2013] found that the settling velocity of particles under wave action was increased from the Stokes settling velocity which resulted in a change to their transport whilst falling or rising. Restrepo and Ramirez [2019] examined the transport of such particles due to the change in inertia and found larger particles travelled far less than smaller particles, although this was mostly due to faster settling velocities. DiBenedetto and Ouellette [2018a] showed that the shape of particles defined their orientation under waves, which changed the transport by altering the fluid drag exerted on particles [DiBenedetto et al., 2018].

If an object is infinitesimally small and the same density as water, it will behave as a purely Lagrangian tracer. Where the mean Lagrangian velocity comprised of any Eulerian mean currents the Stokes drift, where the Stokes drift is a found by integrating the linear velocity of a tracer along its linear trajectory and over a wavelength. As the object grows in size or changes density, it will no longer be a tracer, the object will then have its own inertia, and the fluid will exert drag on the object because there is relative velocity; moreover, the object may rise, sink, or float depending on its relative density and whether the object is floating on the free surface. The mean drift of such an object due to wave forcing can be considered a change to the Stokes drift. Both Stokes drift and an objects mean drift are calculated by following an object's linear velocities caused by wave forcing, then averaging over a wavelength. Previously, the motion of plastic pollution has all been considered to be purely Lagrangian [Isobe et al., 2014, Liubartseva et al., 2018]. To determine whether inertia is important for a floating object, an equation of motion accounting for all the forces on the object, including a dynamic buoyancy term to account for the free surface, and its oscillatory and mean components must be considered.

Chapter 3 presents an equation of motion that correctly models the forces on spherical marine debris, and properly accounts for the dynamic buoyancy of the sphere in the direction perpendicular to the wave surface. Mechanisms for a change in drift are highlighted through a Stokes-like perturbation scheme in steepness. The results of numerical solutions to the model developed are then compared to the enhanced wave-induced drift observed in wave flume experiments on scaled floating spherical objects.

0.2 Aims and Objectives

0.2.1 Aim

The aim of this thesis is to understand and develop suitable models for the mechanisms by which surface gravity waves transport marine debris is the open ocean.

0.2.2 Objectives

The objectives are:

1. To experimentally quantify horizontal and vertical Stokes drift, including,
   - determining the horizontal and vertical Stokes drift components and Eulerian mean flow under deep water wave packets.
2. To investigate the Eulerian mean flow under wave packets, which includes:
   - deriving an analytical solution for the Eulerian mean flow under wave packets valid for all water depths, and
   - understanding the mechanisms for increased return flow in finite water depth.
3. To investigate the wave-induced behaviour of floating marine debris as inertia becomes significant due to increase in size and change in density. This includes:
   - establishing a new equation of motion for spherical floating objects under wave action,
   - finding an analytical solution in the limit of viscous drag by which to interpret the mechanisms for wave-induced drift of larger marine debris, and
   - experimentally validating the change in drift of large spherical floating debris.

0.3 Layout and author's contribution

This thesis is structured as follows. Chapter 1 presents experimental work examining the transport under deep-water wave packets, which is extended in Chapter 2 to be applicable to finite depth wave packets. Chapter 3 examines how object size and density affects the wave-induced transport of floating marine debris. Finally, Chapter 4 presents the main conclusions and recommendations. Note that each chapter commences with a detailed literature review pertinent to the chapter.

0.3.1 Author's contribution

Chapter 1 has been reproduced from T. S. Van Den Bremer, C. Whittaker, R. Calvert, A. Raby, and P.H. Taylor. Experimental study of particle trajectories below deep-water surface gravity wave groups. *J. Fluid Mech.*, 879:168–186, 2019 [Van Den Bremer et al., 2019]. I am a contributing author in this paper for my contributions to the experimental analysis and data interpretation.

Chapter 2 is reproduced from R. Calvert, C. Whittaker, A. Raby, P.H. Taylor, A.G.L. Borthwick, and T. S. van den Bremer. Laboratory study of the wave-induced mean flow and set-down in unidirectional surface gravity wave packets on finite water depth. *Phys. Rev. Fluids*, 4(11):114801, 2019 [Calvert et al., 2019]. As the main author of this paper, I undertook all the mathematical modelling, carried out the experiments, processed the experimental data, and wrote the manuscript.

Chapter 3 is the latest piece of work and the most self-directed. I found the gap in literature, established the mathematical derivations, planned, conducted and analysed the experiments, and wrote the chapter, which has been submitted to the *Journal of Fluid Mechanics.*

Chapter 1

Stokes drift and Eulerian mean flow under deep-water wave packets

Abstract

Due to the interplay between the forward Stokes drift and the backward wave-induced Eulerian return flow, Lagrangian particles underneath surface gravity wave groups can follow different trajectories depending on their initial depth below the surface. The motion of particles near the free surface is dominated by the waves and their Stokes drift, whereas particles at large depths follow horseshoe-shaped trajectories dominated by the Eulerian return flow. For uni-directional wave groups, a small net displacement in the direction of travel of the group results near the surface, and is accompanied by a net particle displacement in the opposite direction at depth. For deep-water waves, we study these trajectories experimentally by means of Particle Tracking Velocimetry in a two-dimensional flume. In doing so, we provide visual illustration of Lagrangian trajectories under groups, including the contributions of both the Stokes drift and the Eulerian return flow to both the horizontal and the vertical Lagrangian displacements. We compare our experimental results to leading-order solutions of the irrotational water wave equations, finding good agreement.

1.1 Introduction

The oscillatory motion of Lagrangian particles below surface gravity waves is subject to a net drift in the direction of wave propagation known as Stokes drift [Stokes, 1847]. For wave groups, the net positive transport associated with the Stokes drift becomes divergent on the group scale and is accompanied by an opposing Eulerian return flow [Longuet-Higgins and Stewart, 1962b]. The total Lagrangian velocity is given by the sum of the Stokes drift and the induced Eulerian flow, and the resulting particle trajectories and displacements have been examined theoretically by van den Bremer and Taylor [2015, 2016].

In the ocean, Stokes drift can provide a significant contribution to the trajectories of drifters [Röhrs et al., 2012] and must be accounted for in search and recovery missions such as the search for debris from the presumed location of the 2014 MH370 airplane crash [Trinanes et al., 2016]. Stokes drift can be important in the local modelling of oil spills [Christensen and Terrile, 2009, Drivdal et al., 2014, Jones et al., 2016]. In the near-surface transport and dispersion of plastic pollution, Stokes drift plays a potentially important yet largely unexplored role (e.g. Lebreton et al. [2018]). Furthermore, Stokes drift is considered a mechanism driving global ocean circulation [McWilliams and Restrepo, 1999, Belcher et al., 2012], Langmuir turbulence [Craik and Leibovich, 1976, D'Asaro et al., 2014, Sullivan and McWilliams, 2010] and submesoscale ocean instability [Haney et al., 2015, McWilliams, 2016].

Experimentally, many authors have considered Stokes drift in laboratory wave flumes. As a visual illustration, Wallet & Ruellan's (1950) seminal image of orbits that do not quite close is reproduced in van Dyke's (1982) Album of Fluid Motion. Yet, there remains some confusion in the literature whether a net drift should be observed (see the discussion in Monismith et al. [2007], Weber [2011], Grue and Kolaas [2017], van den Bremer and Breivik [2017] and Deike et al. [2017]). To explain this, three effects must be taken into account: boundary layers, the origin of vorticity in the interior of the fluid and breaking.

Longuet-Higgins [1953] showed the mass-transport velocity can be significantly different from the irrotational theory of Stokes [1847], with additional net transport arising in the oscillating bottom and surface boundary layers. Explaining experiments by Bagnold [1947], Longuet-Higgins [1953] showed the Lagrangian transport in the boundary layers is positive and does not disappear in the limit of infinite Reynolds number. This boundary layer streaming has recently been studied for very steep waves by Grue and Kolaas [2017], who observed significant additional streaming and associated shear in both the bottom and free surface boundary layers, more than can be predicted by the boundary layer streaming solution of Longuet-Higgins [1953], which Grue and Kolaas [2017] noted may be invalid due to the large steepness of the waves.

For periodic waves, which are the focus of almost all experimental studies focussing on wave-induced mean flows, the net depth-integrated mass flux must be zero in a closed flume. The Stokes transport must be accompanied by a Eulerian return current driven by a setup in the direction downstream of wave propagation, which is conceptually distinct from the return flow forced by the packet structure examined herein. This closed-flume return flow is irrotational, unless vorticity can be transported into the interior of the fluid. Longuet-Higgins [1953] derived two classes of analytical solutions for this vorticity transport: a 'conduction' solution and a 'convection' solution. Depending on the ratio of the wave amplitude a to the thickness of the boundary layer δ, the transport of vorticity takes place by viscous 'conduction' (a^2/δ^2 small) from the bottom and free surface boundary layers, or convection with the mass-transport velocity (a^2/δ^2 large), from the wavemaker or the beach at the other end, where vorticity can be generated. If one considers a motion that is started from rest, the motion in the interior of the fluid will always be initially irrotational, and it will take considerable time for vorticity to be advected or diffused from the vertical or horizontal boundaries, respectively. Finally, as also pointed out by Longuet-Higgins [1953], the convection solution may not be stable.

In the conduction regime, Groeneweg and Klopman [1998] compare their more generally applicable generalized Lagrangian mean model for wave-current interaction to the conduction solution of Longuet-Higgins [1953], showing near perfect agreement, and to the laboratory measurements in a very shallow and long closed flume by Mei et al. [1972], finding good agreement for intermediate water depth ($kh = 1.0$), but less good agreement for deeper water ($kh = 1.8$). However, most experimental studies are in the convection regime. Swan [1990] demonstrated that convection indeed plays an important part within a relatively deep experimental wave flume: vorticity generated at the end conditions is convected backwards with the mass transport velocity and the near-shore region progressively influences the entire length of the wave flume, although the flow field is not always stable. By installing a plastic sheet at the toe of the beach, Swan and Sleath [1990] could obtain long-time stable conditions that agreed better with their 4th-order finite-depth extension of the irrotational solution for Lagrangian transport in a closed domain. Umeyama [2012] performed a similar expansion, but focused explicitly on particle trajectories and found reasonable agreement with experimentally obtained trajectories. Paprota et al. [2016], who took their measurements after a relatively short wave train of periodic waves in a relatively long flume, found good agreement with the irrotational theory of Stokes [1847], supplemented by a closed-flume return current. For waves of intermediate water depth ($kh = O(1)$) and very large steepness, Grue and Kolaas [2017] found good agreement with nonlinear irrotational theory in the interior of the fluid in a set of very high-quality experiments. Their experiments were stopped long before the first waves reach the end of their open-ended flume, but the length of their wave train remains long relative to the water depth. Based on their experiments, Monismith et al. [2007] have suggested a cancellation of the Stokes drift by a Eulerian mean flow that is equal and opposite at every depth. Their experiment were done in the presence of a pre-existing sheared current in a recirculating flume, which could help explain their observation. The current could also advect vorticity at a faster rate than the wave-induced mean flow.

If the waves are breaking, transport of Lagrangian particles near the surface will be considerably enhanced, as observed experimentally by Melville and Rapp [1988] and recently explained using numerical simulations and a scaling argument for breaking by Deike et al. [2017] with implications for surfing [Pizzo, 2017]. Breaking also has the capacity to transport vorticity into the interior of the fluid [Pizzo and Melville, 2013]. Surface waves can be considered to be the ‘gearbox’ between air-sea interactions. In particular, wave breaking plays an important role in many air–sea exchange and upper-ocean processes required to create sea state forecasts using satellite measurements under operation oceanography (see [Ardhuin et al., 2005] and the references within for a review).

The viscous boundary layer at the free surface can also induce a Eulerian mean flow by generating vorticity which is driven downwards and out of the the boundary layer [Longuet-Higgins, 1969]. This mechanism is termed virtual wave stress and is required to satisfy the Eulerian momentum equations established earlier [Longuet-Higgins, 1953]. Weber and Førland [1990] extended the theory to include rotating seas and the viscous effect of air, whilst Weber and Saetra [1995] included a thin visous film on the free surface. The theory was put to use by Ardhuin et al. [2004] to show how wind forces create and interact with waves and Christensen and Terrile [2009] showed the importance of virtual wave stress when modelling oil slicks. We note that the Eulerian mean flow induced by virtual wave stress grows in time and is thus less likely to affect wave packets.

This paper presents an experimental study of Lagrangian trajectories and transport by uni-directional, deep-water, small-amplitude, short-length yet quasi-monochromatic surface gravity wave groups. In doing so, we visualize experimentally for the first time the wave-induced Eulerian return flow for groups. We also show that our experimental observations in this regime are in good agreement with leading-order solutions to the irrotational water wave equations. Our experiments using short-length groups in an otherwise quiescent flume have the advantage of not generating a closed-flume return flow, which may transport vorticity, is potentially unstable, and difficult to control experimentally.

Furthermore, our experiments demonstrate the existence of a vertical component to the Stokes drift, which only exists for wave groups and results in a positive (temporary) vertical particle displacement underneath the centre of the group. This positive vertical displacement by the Stokes drift has been predicted by Herbers and Janssen [2016], who showed the set-down of the wave-averaged free surface in Eulerian records can appear as (significant) set-up in Lagrangian (buoy) records. Nevertheless, a vertical component to the Stokes drift (for groups) has been contentious in adaptations of the work by Craik and Leibovich [1976] in the context of ocean circulation and Langmuir circulation. McWilliams et al. [2004] noted that the vertical Stokes drift is zero and introduced a vertically-divergent vertical pseudo-velocity to compensate for the horizontal divergence of the Stokes drift. Although Mellor [2016] allows for a horizontally-divergent Stokes drift, he still requires the vertical Stokes drift component to be zero. We emphasize that the Stokes drift velocity is generally divergent for groups; this is consistent with generalized Lagrangian-mean theory [Andrews and McIntyre, 1978], as shown by McIntyre [1988]. Accordingly, a vertical Stokes drift component arises for groups, as can be easily derived for irrotational surface gravity waves and is confirmed experimentally herein.

This paper is laid out as follows. First, §1.2 briefly summarizes the irrotational solutions for wave groups, followed by a description of our experimental methodology in §1.3. We present results in §1.4, including illustrations of the Lagrangian orbits, a comparison with irrotational water wave theory and an assessment of the experimental error, and draw conclusions in §1.5.

1.2 Irrotational water wave theory for wave groups

1.2.1 Governing equations and leading-order solutions

In a two-dimensional body of water of depth d with coordinate system (x, z) and z the vertical coordinate measured from the undisturbed water level upwards, inviscid, incompressible and irrotational flow leads to Laplace $\nabla^2\phi = 0$ for $-d \leq z \leq \eta(x,t)$ as the governing equation, where the velocity vector $\mathbf{u} = \nabla\phi$ and $\eta(x,t)$ denotes the free surface. By retaining terms up to quadratic in the amplitude of the waves, the kinematic free surface boundary condition $(w - \partial\eta/\partial t - u\partial\eta/\partial x = 0)$ and the dynamic free surface boundary condition $(g\eta + \partial\phi/\partial t + (u^2 + w^2)/2 = 0)$, both at $z = \eta(x,t)$, can be combined into two forcing equations for the mean flow and the wave-averaged free surface, respectively (e.g. Longuet-Higgins and Stewart [1964], McAllister et al. [2018]):

$$\begin{aligned} \left(\frac{\partial}{\partial z} + \frac{1}{g}\frac{\partial^2}{\partial t^2}\right)\phi^{(2)}\Big|_{z=0} &= \overline{\frac{\partial}{\partial x}\left(u^{(1)}|_{z=0}\eta^{(1)}\right)} + \mathcal{O}(\alpha^2\epsilon^3), \\ \eta^{(2)} &= \frac{-1}{g}\frac{\partial\phi^{(2)}}{\partial t}\Big|_{z=0} + \mathcal{O}(\alpha^2\epsilon^3), \end{aligned} \qquad \text{(1.1a,b)}$$

where the superscripts denote the order in amplitude, and we only retain wave-averaged terms here, as indicated by the overlines on the right-hand side of (1.1a). The small parameter corresponding to amplitude, steepness, is denoted by $\alpha \equiv k_0|a_0|$, where a_0 is the typical amplitude of the surface elevation and k_0 the wavenumber of the carrier wave. Explicitly, we thus have for the Stokes expansion in α that $\phi = \phi^{(1)} + \phi^{(2)} + \mathcal{O}(\alpha^3)$ and $\eta = \eta^{(1)} + \eta^{(2)} + \mathcal{O}(\alpha^3)$, where we will only retain the wave-averaged terms in $\phi^{(2)}$ and $\eta^{(2)}$. In (1.1) we have made the additional assumption that $k_0 d \gg 1$, so that the set-down of the wave-averaged free surface $\eta^{(2)}$ does not directly affect the mean flow [McIntyre, 1981, McAllister et al., 2018]. More specifically, we set $\eta^{(1)} = \mathrm{Re}[A_0(X)\exp(\imath(k_0x - \omega_0t)) + \epsilon A_1(X)\exp(\imath(k_0x - \omega_0t))]$ and $\phi^{(1)} = \mathrm{Re}[B_0\exp(k_0z + \imath(k_0x - \omega_0t)) + \epsilon B_1\exp(k_0z + \imath(k_0x - \omega_0t))]$, where $X \equiv \epsilon(x - c_{g,0}t)$ with $\epsilon \equiv 1/(k_0\sigma)$, σ the characteristic length of the group and $c_{g,0} = d\omega_0/dk_0 = \omega_0/(2k_0)$ the group velocity. The linear ($\mathcal{O}(\alpha)$) polarization relationships at the zeroth and first order in ϵ are given in table 1.1.

Our focus is on leading-order terms; we ignore dispersion of the group (e.g. van den Bremer and Taylor [2016]), and the second-order equations in steepness (1.1) are accurate up to $\mathcal{O}(\epsilon^3)$ in the bandwidth parameter ϵ, as can be shown from the linear polarization relationships in table 1.1. The leading-order, non-dispersive mean flow solution is given by combining the linear polarization relationships in table 1.1 and solving Laplace $\nabla^2\phi^{(2)} = 0$ subject to the bottom boundary condition $\partial\phi^{(2)}/\partial z = 0$ at $z = -d$ and the surface forcing (1.1a) (see also van den Bremer and Taylor [2016])

$$\phi_{\mathrm{E}}^{(2)} = \frac{-\omega_0}{4\pi}\int_{-\infty}^{\infty}\frac{\cosh(|\omega|(z+d)/c_{g,0})}{\sinh(|\omega|d/c_{g,0})}\frac{\omega}{|\omega|}\frac{\imath\widehat{|A_0|^2}}{1-\frac{\omega^2c_{g,0}}{g|\omega|\tanh(|\omega|d/c_{g,0})}}\exp(i\omega\tilde{t})d\omega, \tag{1.2}$$

where we choose $c_{g,0} > 0$ and define $\tilde{t} \equiv t - x/c_{g,0}$. We have expressed the solution as an inverse Fourier transform in time to enable evaluation of the Fourier transform of the square of the leading-order packet $\widehat{|A_0|^2}$ directly from point measurements of the surface elevation. It is instructive to consider the shallow return flow limit $d/\sigma \ll 1$, in which case the velocity field corresponding to (1.2) becomes more simply

$$u_{\mathrm{E}}^{(2)} = -\frac{\omega_0}{2d}\frac{1}{1-1/(4k_0d)}|A_0|^2 \quad\text{and}\quad w_{\mathrm{E}}^{(2)} = -\frac{k_0}{1-1/(4k_0d)}\frac{d+z}{d}\partial_{\tilde{t}}|A_0|^2, \tag{1.3a,b}$$

where $1/(4k_0d)$ in the denominator will be small as $k_0d \gg 1$.

The mean motion of the Lagrangian particles we examine is determined by the sum of the Stokes drift $\boldsymbol{u}_{\mathrm{S}}$ and the wave-induced Eulerian mean flow $\boldsymbol{u}_{\mathrm{E}}$: $\boldsymbol{u}_{\mathrm{L}} = \boldsymbol{u}_{\mathrm{S}} + \boldsymbol{u}_{\mathrm{E}}$ (e.g. Bühler [2014]). The Stokes drift can be determined from the linear waves using the linear polarization relationships in table 1.1:

$$\boldsymbol{u}_{\mathrm{S}} \equiv \overline{\boldsymbol{\xi}^{(1)}\cdot\boldsymbol{\nabla}\boldsymbol{u}^{(1)}} = k_0\left(\omega_0, \frac{3}{2}\frac{\partial}{\partial\tilde{t}}\right)|A_0|^2\exp(2k_0z), \tag{1.4}$$

Field	$O(1)$	$O(\epsilon)$
$\xi_x^{(1)}$	$\imath A_0$	$\left(\frac{1}{2}+k_0z\right)\frac{1}{k_0}\epsilon\partial_X A_0$
$u^{(1)}$	$\omega_0 A_0$	$-\imath\left(1+k_0z\right)\frac{\omega_0}{k_0}\epsilon\partial_X A_0$
$\frac{\partial u^{(1)}}{\partial x}$	$\imath k_0\omega_0 A_0$	$\omega_0\left(2+k_0z\right)\epsilon\partial_X A_0$
$\frac{\partial u^{(1)}}{\partial z}$	$k_0\omega_0 A_0$	$-\imath\omega_0\left(2+k_0z\right)\epsilon\partial_X A_0$
$\xi_z^{(1)}$	A_0	$-\imath\left(\frac{1}{2}+k_0z\right)\frac{1}{k_0}\epsilon\partial_X A_0$
$w^{(1)}$	$-\imath\omega_0 A_0$	$-\left(1+k_0z\right)\frac{\omega_0}{k_0}\epsilon\partial_X A_0$
$\frac{\partial w^{(1)}}{\partial x}$	$k_0\omega_0 A_0$	$-\imath\omega_0\left(2+k_0z\right)\epsilon\partial_X A_0$
$\frac{\partial w^{(1)}}{\partial z}$	$-\imath k_0\omega_0 A_0$	$-\omega_0\left(2+k_0z\right)\epsilon\partial_X A_0$

Table 1.1: Expressions for the different linear (in $\alpha \equiv k_0|a_0|$) fields at $\mathcal{O}(\alpha^1\epsilon^0)$ and $\mathcal{O}(\alpha^1\epsilon^1)$. Values are given in terms of the leading-order amplitude envelope A_0 of the vertical displacement field. The actual fields are the real parts of the tabulated expressions after multiplication by $\exp(k_0z+\imath\varphi_0)$, where the phase is given by $\varphi_0 = k_0x-\omega_0t$. We denote $\eta^{(1)} \equiv \xi_z^{(1)}(z=0)$ as the free surface.

where $\boldsymbol{u}^{(1)}$ is the velocity field of the linear wave and $\boldsymbol{\xi}^{(1)}$ the corresponding linear displacement vector with components $\boldsymbol{\xi}^{(1)} = (\xi_x^{(1)}, \xi_z^{(1)})$, which can be evaluated from the linear velocity field according to $\partial\boldsymbol{\xi}^{(1)}/\partial t = \boldsymbol{u}^{(1)}$. For groups, it is evident from (1.4) that a non-zero vertical Stokes drift exists. Like their horizontal components, the vertical velocities of the return flow and Stokes drift are of opposite sign. Finally, we note that the Stokes drift velocity field is divergent, and (1.4) satisfies the identity for volume conservation $\nabla\cdot\mathbf{u}_\mathrm{S} = (1/2)\partial_{tzz}\overline{(\eta^{(1)})^2}$ from generalized Lagrangian-mean theory (equation (9.4) of Andrews and McIntyre [1978]), shown here correct to leading-order for our case (see also McIntyre [1988]).

1.2.2 Net Lagrangian displacements

After a single group has moved past, the net horizontal and the maximum vertical (positive) particle displacement arising from the Stokes drift (1.4) are given by

$$\Delta x_\mathrm{S} \equiv \int_{-\infty}^{\infty} u_\mathrm{S}d\tilde{t} = \omega_0k_0\exp(2k_0z)\int_{-\infty}^{\infty}|A_0|^2d\tilde{t} = 2\sqrt{\pi}\alpha^2\sigma\exp(2k_0z), \quad (1.5)$$

$$\Delta z_{\mathrm{S,max}} \equiv \int_{-\infty}^{0} w_{\mathrm{S}} d\tilde{t} = \frac{3\alpha^2}{2k_0} \exp(2k_0 z), \tag{1.6}$$

where $\tilde{t} = 0$ is chosen to correspond to the centre of the packet, where the maximum vertical displacement due to Stokes drift occurs. Whereas the first identity in (1.5) holds for a general packet shape, the final identity corresponds to a Gaussian packet $A_0 = a_0 \exp\left(-(x - c_{g,0}t)^2/2\sigma^2\right) = a_0 \exp\left(-c_{g,0}^2\tilde{t}^2/2\sigma^2\right)$ for illustration.

The net horizontal and the minimum vertical (negative) particle displacement arising from the return flow (1.2) are

$$\Delta x_{\mathrm{E}} \equiv \int_{-\infty}^{\infty} u_{\mathrm{E}} d\tilde{t} = -\frac{1}{2}\frac{\omega_0}{d}\frac{1}{1-1/(4k_0 d)}\int_{-\infty}^{\infty} |A_0|^2 d\tilde{t} = -\frac{\sqrt{\pi}\alpha^2\sigma}{k_0 d - 1/4}, \tag{1.7}$$

$$\Delta z_{\mathrm{E,min}} \equiv \int_{-\infty}^{0} w_{\mathrm{E}} d\tilde{t} = -\frac{1}{k_0}\frac{d+z}{d}\frac{\alpha^2}{1-1/(4k_0 d)}. \tag{1.8}$$

As for (1.5), the first identity in (1.7) holds for a general packet shape, whereas the final identity corresponds to a Gaussian packet of the form $A_0 = a_0 \exp\left(-(x - c_{g,0}t)^2/2\sigma^2\right) = a_0 \exp\left(-c_{g,0}^2\tilde{t}^2/2\sigma^2\right)$. In §1.4, we evaluate the net displacements from time integration of the measured surface elevation.

We note that the net horizontal displacement does not decay with depth, in contrast to the horizontal return flow velocity (1.2) for non-shallow return flows ($d/\sigma \not\ll 1$), whereas these horizontal displacements were erroneously shown to decay with depth in van den Bremer and Taylor [2016] due to insufficiently large limits on the time integral therein for very deep water.

From (1.5-1.8), the horizontal and vertical Stokes drift and return flow displacements become equal and opposite at the respective 'transition' depths $z_{\mathrm{T,H}}$ and $z_{\mathrm{T,V}}$

$$\begin{gathered} z_{\mathrm{T,H}} = -\frac{1}{2k_0}\log\left(2k_0 d\left(1 - \frac{1}{4k_0 d}\right)\right) \quad \text{and} \\ \frac{3}{2}\exp\left(2k_0 z_{\mathrm{T,V}}\right) = \frac{d + z_{\mathrm{T,V}}}{d}\frac{1}{1-1/(4k_0 d)}, \end{gathered} \tag{1.9a,b}$$

where $z_{\mathrm{T,V}}$ is defined implicitly, and the horizontal transition depth (1.9a) was derived previously by van den Bremer and Taylor [2016] albeit without the small $(1 - 1/(4k_0 d))$ term to correct for the set down. Figure 1.1 illustrates the dependence of these transition depths on $k_0 d$. The horizontal transition depth (continuous lines) can be a significant fraction of the water depth for

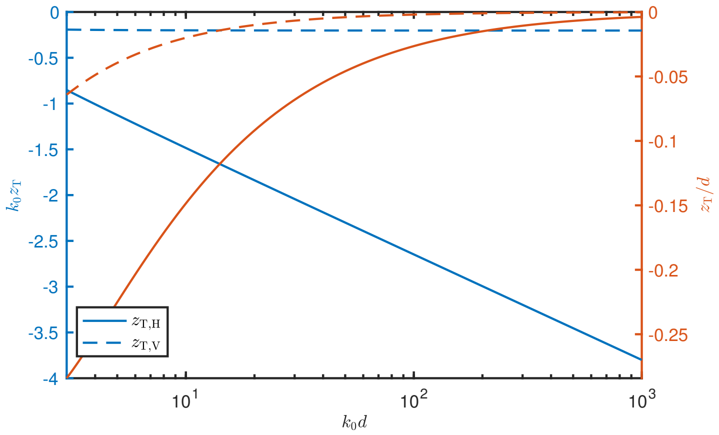

Figure 1.1: Transition depths (1.9) defined as the depths where the horizontal (continuous lines) and vertical Lagrangian (dashed lines) displacements are zero due to cancellation of their Stokes drift and Eulerian return flow components. The colours correspond to the left and right vertical axes, which are scaled differently.

moderate $k_0 d$ (up to $z_{\mathrm{T,H}}/d = -0.28$ for $k_0 d = 3$), whereas the vertical transition depth (dashed lines) is generally given by $k_0 z_{\mathrm{T,V}} \approx -\log(3/2)/2 = -0.20$, which becomes exact in the limit $k_0 d \to \infty$. In the shallow return flow limit ($d/\sigma \ll 1$), the transition depths (1.9) also correspond to the depths below which the horizontal Lagrangian velocity becomes negative and the vertical Lagrangian velocity becomes negative (in front of the packet) or positive (behind the packet), respectively (cf. (1.3)).

1.3 Experimental methodology

1.3.1 Set-up, wave generation and data acquisition

We carried out experiments in the 35 m flume in the COAST (Coastal, Ocean and Sediment Transport) Laboratory at the University of Plymouth, UK. Our visualisation experiments are illustrated in figure 1.2. The flume has a width of 0.6 m and was filled to a depth $d = 0.5$ m. We used a piston-type wavemaker to generate a focused wave group with a spectral shape that under linear evolution would focus to a Gaussian packet $A_0 = a_0 \exp\left(-(x_f - c_{g,0}t)^2/2\sigma^2\right)$ at a measurement zone located $x_f = 9.407$ m from the resting position of the wavemaker (measured free surface elevations are included in figure 1.9 in appendix 1.A). Although the paddles were controlled with a combination of first- and second-order signals based on Schäffer [1996], subharmonic error waves are not expected to play a significant role for the deep-water waves examined here [Whittaker et al., 2017]. A resistance-type wave gauge provided 128 Hz free surface elevation measurements at the focus location; the measured free surface signals provided the parameters used to predict the theoretical particle displacements for each experiment. A light-emitting diode (LED) light box located at the measurement zone (offset in the cross-flume direction from the wave gauge) illuminated the motions of small near-neutrally buoyant particles in a plane, which were captured by a camera located outside of the flume. Camera calibration details are given in appendix 1.B.1.

The 'Plascoat' particles were approximately 150 μm in diameter, small enough to be considered dynamically unimportant. Although the particles were slightly positively buoyant, their upward settling velocities were small or at least slowly varying compared to their motion beneath the free surface waves (see §1.3.3). The particles were effectively uniformly mixed throughout the measurement zone, which was achieved by adding new particles between experiments when necessary, mixing up the water column and waiting for the flume to become quiescent before starting experiments. Because of the light sheet, we only tracked a thin slice of particles in the (x-z)-plane. The camera field of view captured half the depth at a time. To obtain a complete distribution with depth, we thus repeated the same experiment twice.

After propagating through the measurement zone, the dispersed wave groups were absorbed by foam wedges within an 'absorption zone' located at the downstream end of the wave flume. The measurement zone was located far enough from the wavemaker to minimise the effects of evanescent modes from the wavemaker. To ensure near-quiescent initial conditions for each experiment the flume was allowed to settle for 10 minutes between experiments. Although negligible free surface motions remained after this time period, some slow circulations lingered within the subsurface velocity field; these 'background particle velocities' were removed during post-processing of the particle trajectories, as described below. The settling time of 10 minutes was short enough that the slightly positively-buoyant particles remained evenly distributed throughout the water column at the start of each experiment.

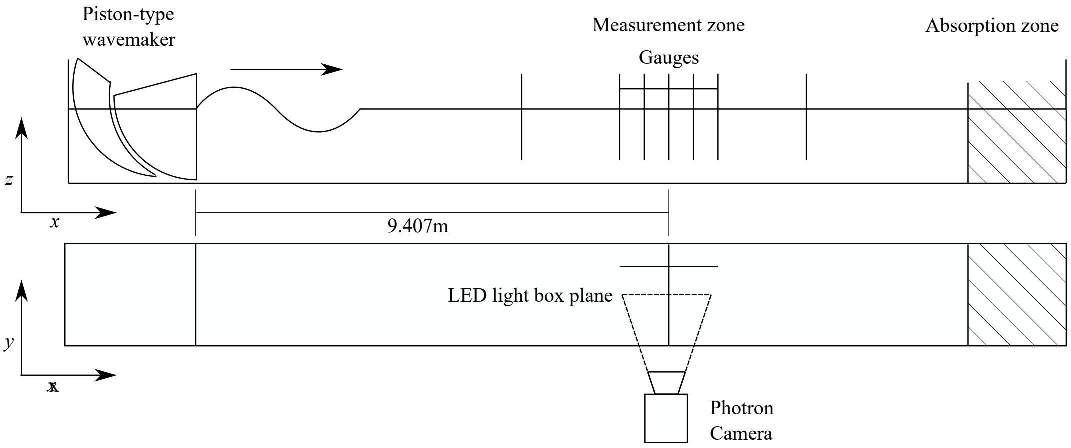

Figure 1.2: Experimental set-up used to obtain PTV measurements of trajectories below focused wave groups generated by a piston-type wavemaker in the 35 m flume in the COAST Laboratory at the University of Plymouth.

1.3.2 Matrix of experiments

We conducted 12 experiments, as outlined in table 1.2 with experiment 1 conducted 10 times to determine repeatability. Frequencies were chosen such that the water depth is deep ($k_0 d \gtrapprox 3$); amplitudes such that second-order motions are large enough to measure, but not too large so that effects beyond second-order play a role; and the bandwidth parameter $\epsilon = 1/(k_0\sigma)$ such that the wave group is still quasi-monochromatic (see van den Bremer and Taylor [2016]), but the wave groups not so long that reflections play a role. Having defined ϵ based on length scales in the physical domain and for a Gaussian group, we can obtain an estimate of the number of waves per group of $4\sigma/\lambda_0 = 2/(\pi\epsilon) \approx 2.5 - 4$ (cf. table 1.2 and figure 1.9 in appendix 1.A). We investigated both crest-focused (CF) and trough-focused (TF) wave groups, for which frequencies have phases of 0 or π at focus, respectively.

Experiment	f_0 [Hz]	$\alpha = k_0 a_0$	$\epsilon = (k_0\sigma)^{-1}$	$k_0 d$	Phase at focus [deg]	No. of raw trajectories	No. of post-processed trajectories
1	1.25	0.13	0.21	3.16	0	609	115
2	1.25	0.13	0.21	3.16	180	505	92
3	1.25	0.12	0.16	3.16	0	317	53
4	1.25	0.12	0.16	3.16	180	345	51
5	1.25	0.12	0.26	3.16	0	556	107
6	1.25	0.12	0.26	3.16	180	502	130
7	1.5	0.10	0.20	4.53	0	573	147
8	1.5	0.10	0.20	4.53	180	499	87
9	1.5	0.12	0.16	4.53	0	242	56
10	1.5	0.12	0.16	4.53	180	345	90
11	1.5	0.09	0.23	4.53	0	444	99
12	1.5	0.09	0.23	4.53	180	477	119

Table 1.2: Matrix of experiments.

1.3.3 Data processing and removal of background motion

The recorded images were processed using the Streams software package, a specialist package for flow visualisation applications [Nokes, 2014] (see appendix 1.B.2). Lagrangian paths were calculated for particles that had been continuously matched for at least $\pm 6T_g$ with $T_g = \sigma/c_{g,0}$ either side of the time of focus. Despite the settling time between experiments, we found persistent background motion of the particles on a time scale much greater than the linear motion and the motion associated with Stokes drift and the Eulerian return flow beneath the group.

This background motion consists of a combination of upward settling of particles, long waves or 'seiche modes' that decay very slowly in the flume and Ekman-type circulation that result from small air flows over the surface that cannot be entirely eliminated in the laboratory. We can estimate the (upward) Stokes settling velocity for our spherical particles as $w = (2/9)((\rho_w - \rho_p)/\rho_w)(gR^2/\nu) = 0.47\,\mathrm{mm/s}$, where we have used $\rho_p = 0.96\,\mathrm{g/cm^3}$, $\rho_w = 0.998\,\mathrm{g/cm^3}$, $\nu = 1.0 \times 10^{-6}\,\mathrm{m^2/s}$ and $R = 75 \times 10^{-6}\,\mathrm{m}$. We can also estimate the velocity associated with a linear long wave of amplitude $a = 0.1\,\mathrm{mm}$ (probably the smallest that can be detected by the gauges) to be $u = a\sqrt{g/d} = 0.44\,\mathrm{mm/s}$. For comparison, the Stokes drift near the surface ($z = 0$) and at the point of focus is $u_\mathrm{S} = c_{p,0}\alpha^2 = 21\,\mathrm{mm/s}$ for $c_{p,0} = 1.25\,\mathrm{m/s}$ ($f_0 = 1.25\,\mathrm{Hz}$) and $\alpha = 0.13$ (see table 2). For the same case, the return flow velocity is $u_\mathrm{E} = c_{p,0}\alpha^2/(2k_0 d - 1/2) = 3.6\mathrm{mm/s}$ for $d = 0.5\,\mathrm{m}$. Fortunately, all these background motions vary more slowly than the waves and their induced mean flows themselves and we can remove these by fitting to the background motion before and after the arrival of the group. The Lagrangian displacements were calculated after removal of this slow background motion, and the quality of the trajectories assessed, resulting in a smaller number of post-processed compared to raw trajectories, as reported in table 1.2.

When visually assessing the quality of the trajectories, we dismissed particles with incompletely recorded trajectories and particles for which our automatic criterion for identifying the focus time, namely the time at which the horizontal velocity reached a maximum, was not successful. The displacements were calculated between $t = -3T_g$ and $t = +3T_g$, with $t = 0$ corresponding to the focus point, $T_g = \sigma/c_{g,0}$ denoting the group period, and the limits chosen so that the overlying wave group has effectively zero amplitude. The trajectories

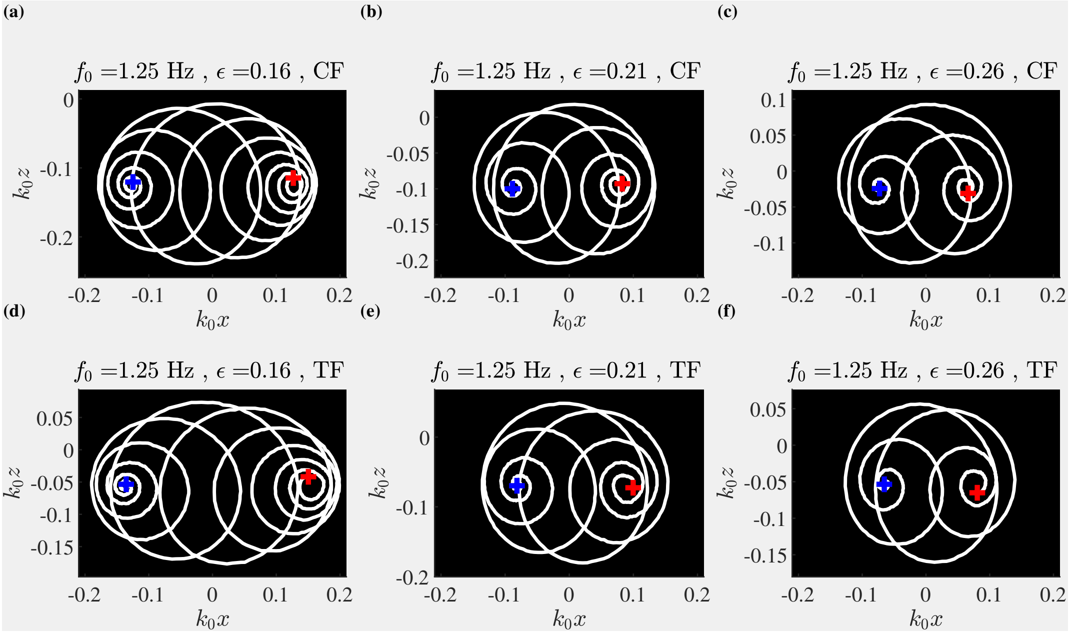

Figure 1.3: Experimental particle trajectories for particles near the surface below crest-focussed (CF, top row) and trough-focussed (TF, bottom row) wave groups for three different groups lengths σ (columns), as denoted by $\epsilon = 1/(k_0\sigma)$. The blue and red + symbols denote experimentally determined initial and final particle positions, respectively.

recorded for times outside this window, during which there was no overlying wave group, were then used to fit to and then remove background motion. To do so, we considered four fitting methods and selected the one that minimized the displacement due to the background motion over the window $t = \pm 3T_g$ (see appendix 1.B.3 for further details).

1.4 Results

1.4.1 Particle trajectories

Figure 1.3 shows representative measured particle trajectories near the surface for crest-focussed (CF, top row) and trough-focussed (TF, bottom row) experiments with three different bandwidths (columns). Near the surface, the Stokes drift is dominant, the trajectories for shorter groups (larger ϵ) are made up from fewer orbits with smaller net horizontal displacements, and the vertically-asymmetric relationship between crest-focussed and trough-focussed trajecto-

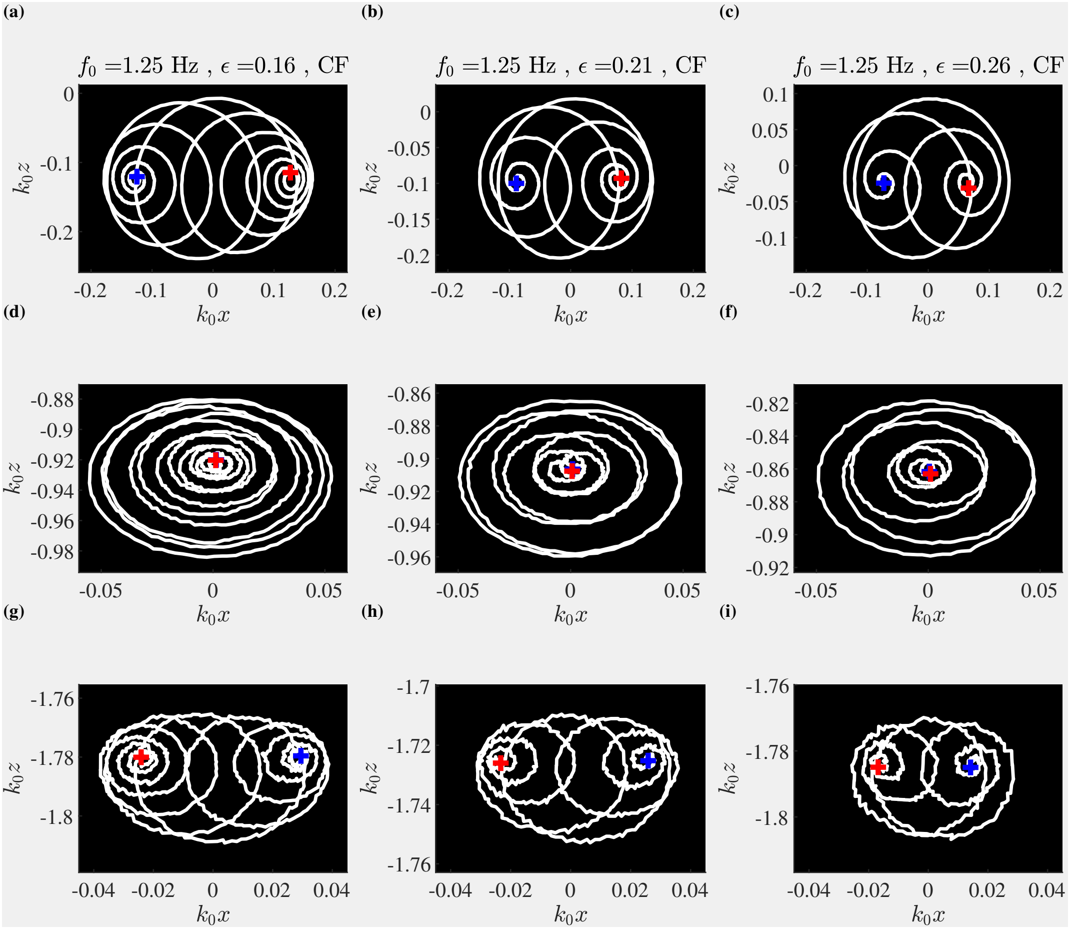

Figure 1.4: Experimental particle trajectories for particles at different depths (rows) for three different groups lengths σ (columns), as denoted by $\epsilon = 1/(k_0\sigma)$. The blue and red + symbols denote experimentally determined initial and final particle positions, respectively.

ries is clearest from comparing figures 1.3c and 1.3f. The different columns in figure 1.4 show how particle trajectories vary with depth. Descending in the fluid, the net horizontal displacement transitions from positive near the surface (top row), via zero (middle row) to negative at depth (bottom row). At all depths, the linear wave signature remains present, although the magnitude of the orbits decreases. The horseshoe-shaped mean motion induced by the return flow is evident at depth (fig. 1.4g-i). In both figures 1.3 and 1.4, the blue and red symbols respectively denote the experimentally determined initial and final particle positions, which will be examined for all orbits below.

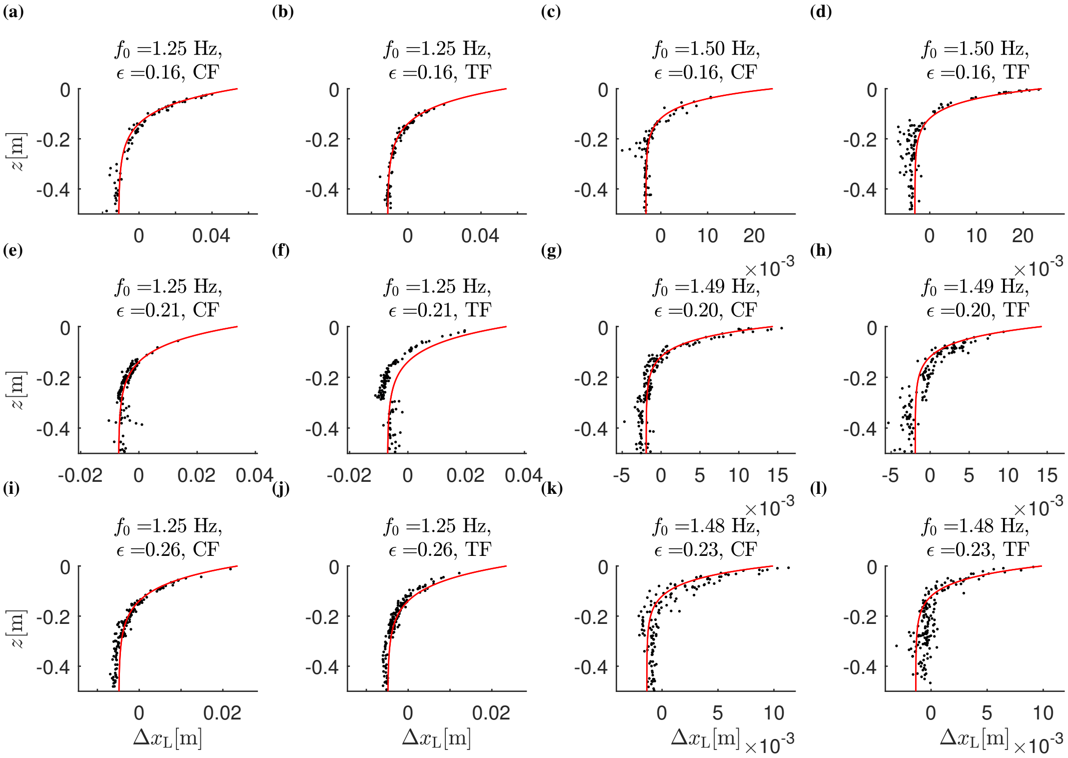

Figure 1.5: Net horizontal Lagrangian displacement from experiments (black dots) compared to theoretical predictions (red lines) for all experiments in table 1.2.

1.4.2 Net Lagrangian displacements

After removal of background motion, figure 1.5 compares net horizontal Lagrangian displacement from experiments (black crosses) to theoretical predictions (red lines) for all experiments. The theoretical predictions are evaluated from (1.5) and (1.7), where we evaluate ω_0 from the peak of the surface elevation spectrum and compute k_0 from the linear dispersion relationship. Instead of fitting a Gaussian functional form, we numerically evaluate the time integrals in (1.5) and (1.7) over the envelopes extracted from the surface elevation measurements from the gauge, where we first remove bound waves from the spectrum, which has well separated harmonics, using filtering. As expected based on irrotational theory for wave groups, the net positive displacements near the surface dominated by the Stokes drift are accompanied by opposing displacement at depth dominated by the return flow.

The changes in the net displacement due to changes in bandwidth (ϵ) that can be observed in figure 1.5 are indeed accurately predicted by our leading-

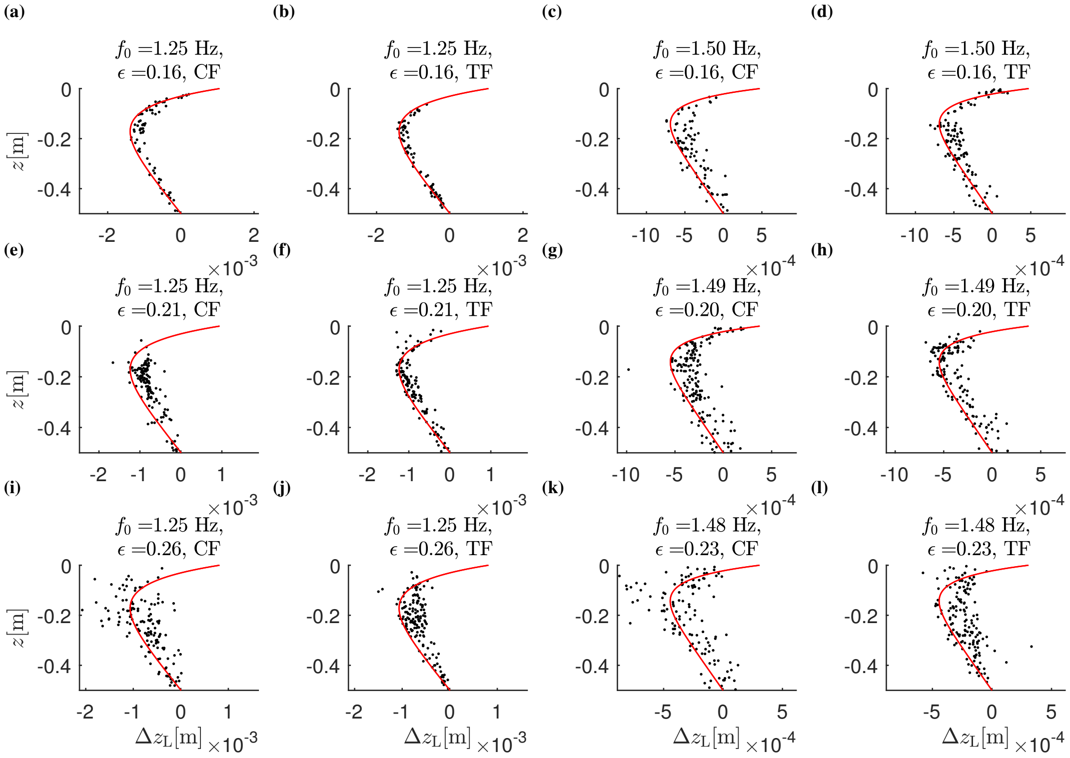

Figure 1.6: Maximum or minimum vertical Lagrangian displacement from experiments (black dots) compared to theoretical predictions (red lines) for all experiments in table 1.2.

order (in ϵ) results (1.5) and (1.7). Keeping k_0 constant, increasing ϵ amounts to a reduction in the group length σ with a consequent reduction in the net displacement, as predicted by (1.5) and (1.7). Although our expressions are only strictly valid in the narrow-banded limit $\epsilon \equiv 1/(k_0\sigma) \rightarrow 0$, higher-order terms only potentially arise at two orders higher in ϵ. Based on the values of ϵ considered here and the calculations performed in van den Bremer and Taylor [2016], we estimate the error associated with our narrow-banded assumption to be a few percent in the worst case.

Using a similar procedure, figure 1.6 compares the maximum or minimum vertical Lagrangian displacement underneath the centre of the group to their theoretical predictions (1.6) and (1.8). The upward displacement by the Stokes drift near the surface predicted by irrotational theory for groups is accompanied by the classical Eulerian set-down at greater depth and decreasing linearly with z to zero at the bottom (cf. (1.8)).

In both figures 1.5 and 1.6, the orbits near the surface are not always perfectly captured, which is a result of their larger size and the (reflective) free

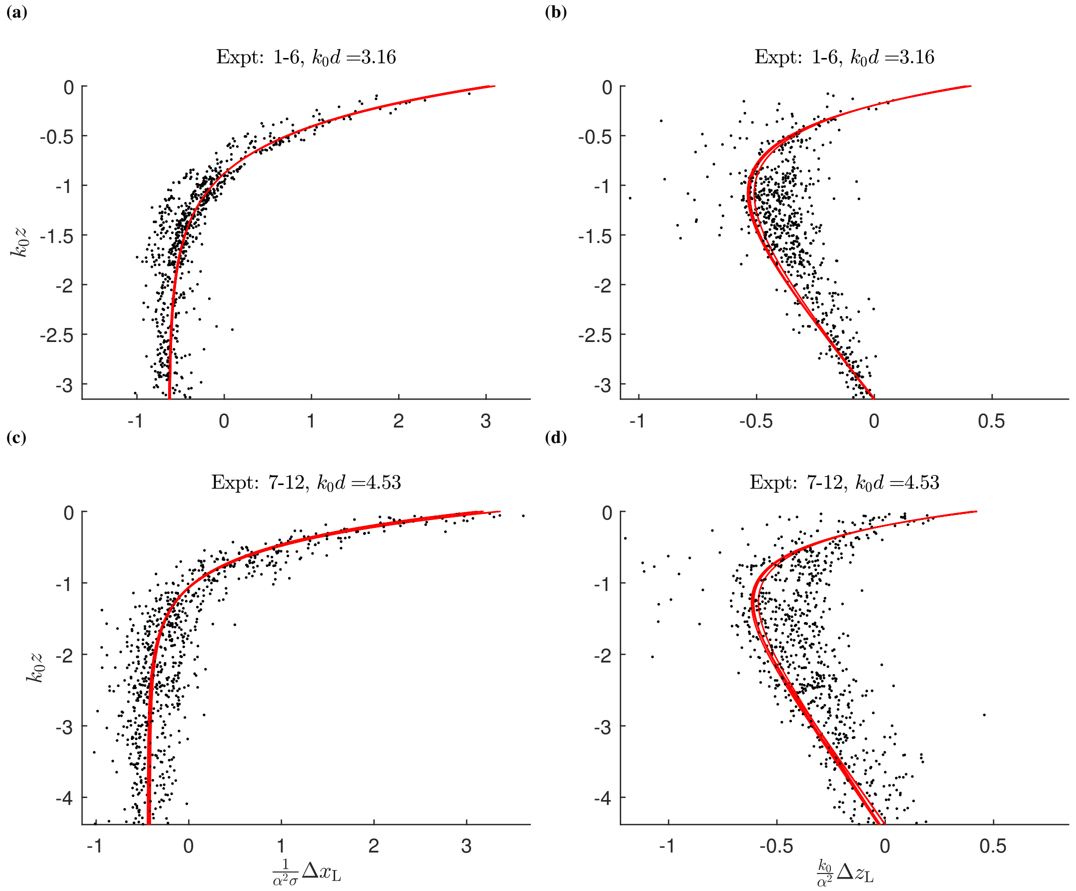

Figure 1.7: Scaled Lagrangian displacement from experiments (black dots) compared to theoretical predictions (red lines): the left column shows net horizontal displacement, the right column maximum or minimum vertical displacement. The rows correspond to k_0d =3.16 and 4.53, respectively, where k_0d is the only non-dimensional parameter that cannot be scaled out. Note that several very slightly different theoretical curves are shown due to small differences between the free surface elevation across experiments that cannot be scaled out.

surface moving through the camera window. Although the scatter in the data is not insignificant for some experiments (addressed in §1.4.3), they line up well with theoretical predictions, including the magnitude of the displacement by the Stokes drift and the return flow. Finally, figure 1.7 presents scaled (non-dimensional) Lagrangian displacements from the experiments, noting from (1.5-1.8) that all parameters can be scaled out except for k_0d.

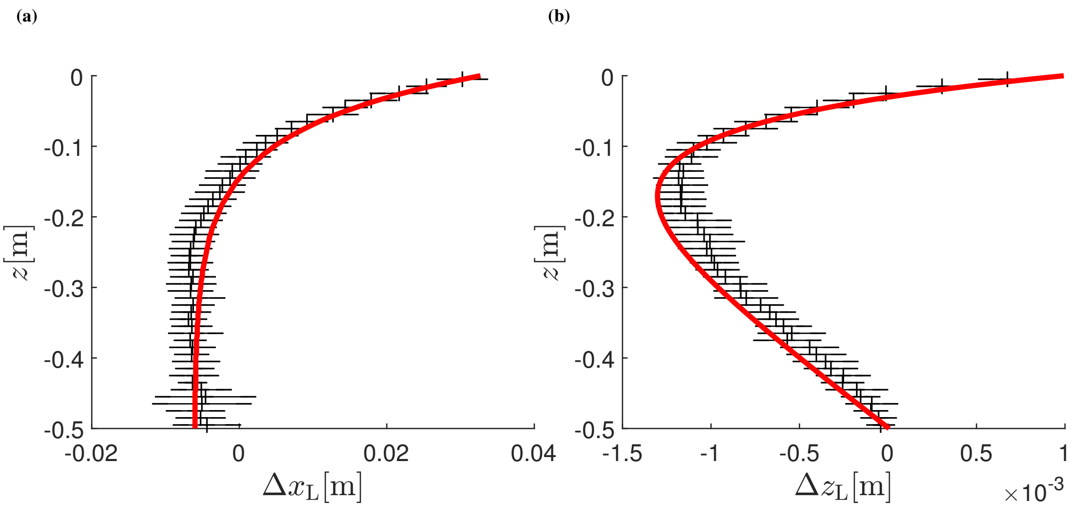

Figure 1.8: Confidence bands on the net horizontal (a) and the maximum or minimum vertical displacement (b) from 10 repeats of experiment 1 with the red lines denoting theoretical predictions. The error bars correspond to two standard deviations either side of the mean.

1.4.3 Repeatability

In order to assess repeatability of experiments and robustness of background motion removal, we conducted experiment 1 ten times. For both the horizontal and the vertical displacements, figure 1.8 demonstrates good agreement (to within two standard deviations) between experiments and theoretical predictions, notably including the positive vertical displacement by the Stokes drift in figure 1.8b. Most of the variability for single experiments observed in figures 1.5-1.7 is likely due to unpredictable small residual motions present in the flume, which cannot be perfectly removed. In fact, the reason that the agreement with the theoretical solutions appears better for the horizontal displacements (cf. figure 1.5) than for the vertical displacements (cf. figure 1.6) is simply that the horizontal displacements are larger, making removal of background motion easier. Furthermore, the displacement associated with longer groups (smaller ϵ) is simply larger and thus easier to measure.

1.5 Conclusions

This paper has reported on an experimental study of Lagrangian trajectories underneath uni-directional, deep-water surface gravity wave groups and has demonstrated visually their wave-induced Eulerian return flows as well as their Stokes drifts in experiments. Our quasi-monochromatic, small-amplitude, non-breaking experimental observations are in good agreement with leading-order solutions to the irrotational water wave equations. We have also shown that the Stokes drift for groups has both a horizontal and a vertical component, where the former results in a net displacement, whereas the latter leads to a temporary positive set-up for particles a small distance below the centre of a group, defined by a 'transition' depth. Such a non-zero vertical Stokes drift is contentious in equations of the Craik and Leibovich [1976]-type [McWilliams, 2016, Mellor, 2016], but has been predicted to affect Lagrangian buoy records [Herbers and Janssen, 2016]. For the relatively short, yet still quasi-monochromatic, groups we have examined, boundary layers do not have sufficient time to form and result in streaming of Lagrangian particles. Based on a typical velocity of $a_0\omega_0 = 0.16\,\mathrm{m/s}$ for $a_0 = 0.021\,\mathrm{m}$ and $\omega_0 = 7.9\,\mathrm{rad/s}$ and taking the amplitude a_0 as the typical length scale, we obtain a Reynolds number of 3.5×10^3 (laminar). If we take the group length scale $\sigma = 1.0\,\mathrm{m}$ as the characteristic length scale (for $f_0 = 1.25\,\mathrm{Hz}$ and $\epsilon = 0.16$), we can estimate the boundary layer thickness that can develop over this scale as $\delta = 4.91\sqrt{(\sigma\nu)/(a_0\omega_0)} = 0.012\,\mathrm{m}$ (Blasius solution for a laminar boundary layer over a plate). This is too small to play a role in our measurements. Furthermore, these short groups avoid the set up of a closed-flume return flow associated with periodic waves, which may transport vorticity, be difficult to control experimentally and could account for some of the confusion in the literature. The majority of laboratory experiments where no net drift, or an unexpected depth profile, has been observed can be explained by boundary layers, the convection and conduction of vorticity or breaking. However, the finding by Smith [2006] of Eulerian counterflows that occur under wave groups in field data that completely cancel the Stokes drift variations at the surface is left unexplained.

Although experimental studies, including the present one, have focussed exclusively on particles that behave as perfect Lagrangian tracers, modelling of transport of particles of all sizes and shapes in the upper ocean will require consideration of particle inertia [Eames, 2008, Santamaria et al., 2013] and anisotropy [DiBenedetto and Ouellette, 2018b, DiBenedetto et al., 2018], as well as 'surfing' of particles near the surface [Pizzo, 2017, Deike et al., 2017]. Future work will examine these effects experimentally.

Acknowledgments

TSvdB was supported by a Royal Academy of Engineering Research Fellowship. The authors would like to acknowledge J. Vanneste and C. Higgins for demonstrating that the net displacement (1.7) is not a function z and W. Young for pointing out that there can be a vertical Stokes drift for irrotational water wave groups.

Appendix

1.A Measured free surface elevation signals

Figure 1.9 shows the unfiltered measured free surface elevation signals for the 12 experiments in table 1.2.

1.B Experimental procedure and data processing

1.B.1 Camera settings and calibration

During the experiments, a light-emitting diode (LED) light box located above the flume illuminated a two-dimemsional plane approximately 1 m long and 10 mm thick. Ambient lighting was removed during these experiments, to maximise the contrast between the illuminated particles and the image background. A Photron SA4 high-speed camera captured the particle motions within the plane illuminated by the LED light box. Each experiment was repeated multiple times to ensure complete coverage of the depth and some overlap between different camera windows as a result. The camera captured images at 125 frames/s, with a resolution of 1024 by 1024 pixels and a shutter speed of 1/125 s (i.e. opening the shutter for the duration of image acquisition). This shutter speed achieved an acceptable compromise between the requirements of obtaining very sharp images (requiring a high shutter speed) and allowing sufficient light to enter the CCD of the camera during each image (requiring a low shutter speed). Before conducting each experiment, the camera captured a calibration image of a ruler, allowing quantification of the pixel scale and any distortion in the images (barrel-pincushion distortions were found to be

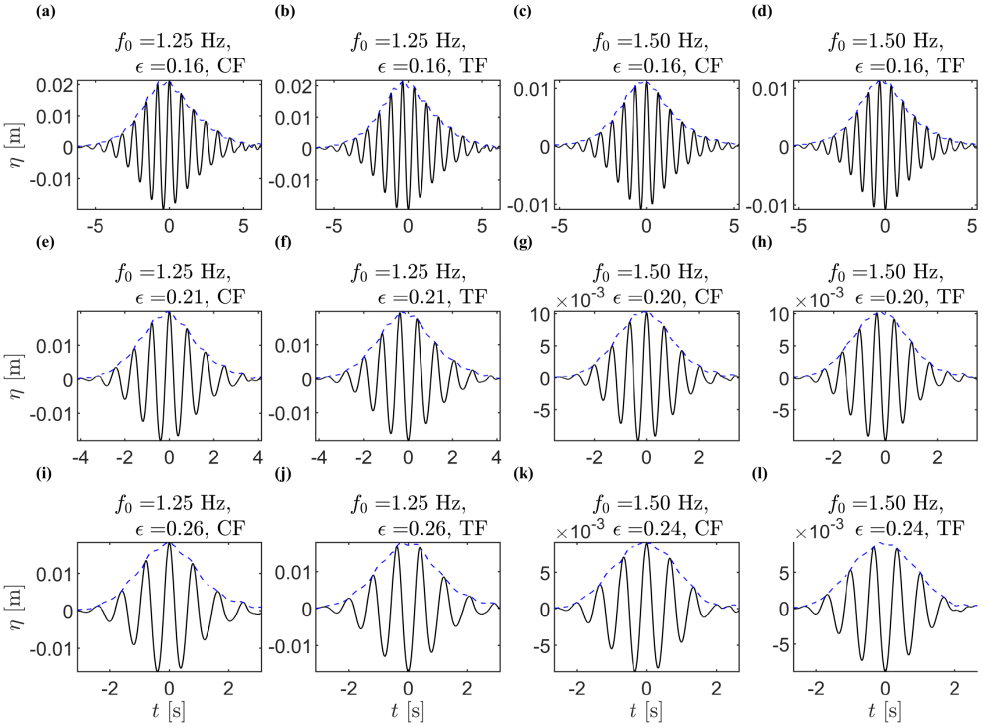

Figure 1.9: Measured free surface elevation signals for the 12 experiments in table 1.2: the blue lines dashed denote the envelopes obtained using a Hilbert transform.

negligible for these tests). The image was calibrated by placing a ruler in the light sheet.

1.B.2 Image processing and particle tracking

The particles within each image were identified using a dual threshold algorithm, which first searched the image for pixels with an intensity greater than a particular threshold, identified the maximum pixel intensity within the group of pixels and finally defined the particle boundaries based on a fraction of this maximum intensity. This algorithm has the advantage of correctly identifying stationary and moving particles within a range of lighting conditions. The identified particles were subsequently matched between frames using an ‘auction’ optimisation algorithm. This auction algorithm optimised the particle matches by minimising the total cost of all potential matches for each successive pair of frames, where the cost was first assigned based on particle distance, then based on the (matched) particle velocities in a small region. The velocities of matched particles were finally used to generate additional matches where appropriate.

1.B.3 Removal of background motion

In order to remove background motion, we first centre the signal around the time of focus, chosen as the time of the maximum horizontal velocity, so that it corresponds to $t = 0$ and then consider four ways of fitting to the background motion in the signals $(x(t), z(t))$:

1. linear fit to the x-displacement prior to wave group arrival over $(-6T_g, -3T_g)$ and quadratic fit to the z-displacement before and after wave group arrival over $(-6T_g, -3T_g)$ and $(3T_g, 6T_g)$;
2. linear fit to the x-displacement prior to wave group arrival over $(-9T_g, -3T_g)$ and quadratic fit to the z-displacement before and after wave group arrival over $(-9T_g, -3T_g)$ and $(3T_g, 9T_g)$;
3. linear fit to the x-displacement prior to wave group arrival over $(-12T_g, -3T_g)$ and quadratic fit to the z-displacement before and after wave group arrival over $(-12T_g, -3T_g)$ and $(3T_g, 12T_g)$;
4. linear fit to the x-displacement and quadratic fit to the z-displacement before and after wave group arrival over $(-9T_g, -3T_g)$ and $(3T_g, 9T_g)$;

where we estimated the group velocity $c_{g,0}$ and hence the group period T_g from the spectral peak of the measured free surface time series.

All trajectories were visually inspected to ensure the orbit was complete and the focus location correctly identified. Of the four fitting methods, we selected the method that minimised the net ‘background’ displacement of the particle within the fit windows for each trajectory. After satisfactory processing of the particle orbits, the net displacements were calculated between $-3T_g$ and $3T_g$.

Chapter 2

Eulerian mean flow under finite-depth wave packets

Abstract

The net movement of Lagrangian particles under water waves comprises a Stokes drift in the direction of wave propagation and an Eulerian return flow in the opposing direction. Accurate prediction of the Eulerian return flow in the ocean is of importance in modeling the transport of plastic pollution, oil, wreckage, and sediment. Herein, we derive a multiple-scales solution for the Eulerian mean flow under wave packets that is valid for all water depths, relative to both the length of the wave and the length of the wave packet. To validate this solution, we carry out particle tracking velocimetry experiments in a long flume to extract the mean motion from Lagrangian seeding particles under wave packets, finding good agreement. The extraction technique is able to deal with small background motion and subharmonic error waves associated with wave generation by the paddle, the latter being relatively large in finite-depth flume experiments. In finite depth, the return flow is forced by both the divergence of the Stokes transport on the wave-packet scale and the formation of a non-negligible mean set-down underneath the packet, which acts like a bounding streamtube in the form of a convergent-divergent duct. The magnitude of the horizontal return flow is thus enhanced, with particular relevance to transport in the finite-depth coastal environment.

2.1 Introduction

Although fluid particles under progressive, small-amplitude surface gravity waves predominantly move forward and backward with linear motion, they undergo a small forward net transport known as the Stokes drift [Stokes, 1847]. Realistic seas are not regular waves but are composed of wave packets, which can be represented as a linear superposition of waves of different frequencies [Longuet-Higgins, 1957]. In the limit of a narrow-banded spectrum, these packets can also be obtained by the amplitude modulation of a single frequency wave. Given that Stokes drift depends on the square of the local wave amplitude, its associated mass transport becomes divergent at packet-scale: mass transport is larger at the center of the group than at leading and trailing edges. This divergence must be balanced by a return flow in the direction opposite to wave propagation, which also causes a depression in the wave-averaged free surface under the wave packet, known as the set-down [Longuet-Higgins and Stewart, 1962a]. The depression in the wave-averaged free surface can be thought of as further enhancing the magnitude of the return flow.

Together, Stokes drift and the wave-induced Eulerian return flow make up the wave-induced Lagrangian velocity field, and both occur at second-order in a Stokes expansion. The Lagrangian velocity field is important in the prediction of species transport in the ocean, encompassing the movement of sediment, plastic, oil, and wreckage (see van den Bremer and Breivik [2017] for a recent review of Stokes drift and its applications). Because of its potentially large damage to marine wildlife, plastic, and more specifically microplastic, has recently attracted a great deal of attention [Cole et al., 2011, Cózar et al., 2014]. Although recent research has focused on documenting the concentrations of plastic in the coastal region [Isobe et al., 2014], and predicting locations of plastic accumulation [Sherman and Sebille, 2016], the effect of wave-induced plastic transport has yet to be fully explored. Wave-induced transport must also be included in the search for wreckage, such as that concerning the 2014 MH370 airplane crash in the Indian Ocean [Trinanes et al., 2016]. Stokes drift is also important in the modeling of oil spills [Christensen and Terrile, 2009, Drivdal et al., 2014, Jones et al., 2016] and in sediment transport [Deigaard et al., 1992, Nielsen, 1992].

Although it can be ignored in sufficiently deep water [McIntyre, 1981], the set-down of the wave-averaged free surface becomes important when the water depth is finite. Ignoring set-down or incorrectly reproducing it in numerical or laboratory experiments has been shown to lead to incorrect predictions of run-up on beaches [Orszaghova et al., 2014]. Generation of wave packets using linearly controlled wave paddles leads to spurious “error waves" on the scale of the group, which travel ahead of the wave packet as free waves, typically at the shallow-water phase velocity in laboratory flumes [Whittaker et al., 2017] (see also the discussion in Nielsen and Baldock [2010], Orszaghova et al. [2014]). Second-order wave generation, where the subharmonic frequencies represent the correct generation of the mean flow and the set-down of the wave-averaged free surface, has been proposed to remedy this [Schäffer, 1996, Leeuwen and Klopman, 1996]. Implementation of second-order wave generation can, however, be limited by the requirement of a large paddle stroke on the scale of the group [Whittaker et al., 2017].

Historically, several approaches have been taken to derive analytical solutions for the mean flow and the wave-averaged free surface under wave packets. These solutions can be classified on the basis of two scales: the water depth d relative to carrier wavelength, namely $k_0 d$, with k_0 denoting the carrier wave number, and the water depth relative to packet length, namely d/σ, with σ denoting the packet length scale. 2.1 shows the regimes based on these two nondimensional numbers for which solutions have been proposed in the literature. Assuming the return flow is shallow, i.e., $d/\sigma \ll 1$, such that the horizontal return flow is uniform over depth, Longuet-Higgins and Stewart [1962a], Davey and Stewartson [1975], Brinch-Nielsen and Jonsson [1986], Mei et al. [1989] presented solutions for the set-down and return flow. These solutions can describe water depths that are shallow, deep, or intermediate with respect to the carrier wavelength [$k_0 d \ll 1$, $k_0 d \gg 1$, or $k_0 d = O(1)$, respectively]. When $d/\sigma \gg 1$, the return flow does not extend to the bottom of the ocean floor, thus it is considered a deep return flow and it has been modeled by Dysthe [1979] (and van den Bremer and Taylor [2016]). None of these multiple-scales solutions are valid for an intermediate depth return flow, $d/\sigma = O(1)$. Taking a different approach, Dalzell [1999] represents the wave packet as an infinite sum over the wave number. This results in a solution for the set-down and mean flow in the form of a double summation of “frequency-difference" waves, which oscillate with a frequency of the difference between any waves used to represent the wave-packet. Dalzell [1999] makes no assumptions concerning the depth of the return flow or carrier wave. However, the solutions do not enable a simple evaluation of Lagrangian particle displacements. Expressions for these “frequency-difference" terms can also be distilled from Longuet-Higgins and Stewart [1962a], Hasselmann [1962], Okihiro et al. [1992], Sharma and Dean [1981], Forristall [2000] (see Pellet et al. [2017] for a recent rederivation that also includes pressure).

Experimentally, many authors have considered Stokes drift in laboratory wave flumes. There remains some confusion in the literature about whether a net drift should be observed (see the discussion in [Monismith et al., 2007, Grue and Kolaas, 2017, van den Bremer and Breivik, 2017, Deike et al., 2017]). In addition to the solutions to the irrotational water wave equations [Umeyama, 2012, Paprota et al., 2016], streaming in the boundary layers [Longuet-Higgins, 1953, Bagnold, 1947, Grue and Kolaas, 2017], convection of vorticity from the ends of the tank into the interior of the fluid [Longuet-Higgins, 1953, Swan, 1990] (or conduction from the free surface and bottom boundary layers [Groeneweg and Klopman, 1998]), or enhanced transport for particles on the surface in breaking waves may play a role [Melville and Rapp, 1988, Deike et al., 2017, Pizzo, 2017]. Recently, van den Bremer et al. [under review] have demonstrated experimentally that Lagrangian transport by the combination of Stokes drift and the Eulerian return flow underneath unidirectional, deep-water surface gravity wave packets is in good agreement with leading-order solutions to the irrotational water wave equations.

This paper derives solutions for the mean flow and the wave-averaged free surface using the multiple-scales method. These solutions are valid in arbitrary depths relative to the scale of the packet and the Eulerian return flow. The theory recovers all regimes for which solutions have previously been derived (see Table table 2.1), and the predicted set-down matches the multicomponent theory of Dalzell [1999] in the narrow-banded limit. In doing so, we correct incomplete predictions in the finite-depth regime by van den Bremer and Taylor [2015]. We calculate Lagrangian transport by integrating the Eulerian mean flow and Stokes drift velocity. We also carry out new particle tracking velocimetry (PTV) experiments for wave packets in a laboratory wave flume in the finite-depth regime, in which the effect of set-down on Lagrangian particle displacement becomes significant. We thus extend results for deep-water for which the set-down can be ignored (obtained by van den Bremer et al. [under review]), to finite depth for which it cannot. We measure the set-down, take into account the effect of error waves, extract the Lagrangian displacement, and compare results with our theoretical predictions, finding good agreement.

The paper is laid out as follows. First, Sec. 2.2 outlines second-order theory, leading to a solution for Eulerian return flow in arbitrary depth and displacements arising from Eulerian mean flow and Stokes drift. Section 2.3 describes the experimental method, and Sec. 2.4 presents a comparison of theoretically predicted and experimentally determined displacements. Finally, conclusions are drawn in Sec. 2.5.

Table 2.1: Classification of the literature in different regimes based on depth relative to the carrier wavelength ($k_0 d$) and depth relative to the wave-packet length or the return flow scale (d/σ).

Regime	Carrier wave depth ($k_0 d$)	Return flow depth (d/σ)	
Deep carrier wave and deep return flow	$\gg 1$	$\gg 1$	Dysthe [1979] van den Bremer and Taylor [2015] this paper
Deep carrier wave and shallow return flow	$\gg 1$	$\ll 1$	Mei et al. [1972] Longuet-Higgins and Stewart [1962a] Davey and Stewartson [1975] Brinch-Nielsen and Jonsson [1986] This paper
Intermediate-depth carrier wave and intermediate-depth return flow	$O(1)$	$O(1)$	This paper
Intermediate-depth carrier wave and shallow return flow	$O(1)$	$\ll 1$	Longuet-Higgins and Stewart [1962a] Davey and Stewartson [1975] This paper

2.2 Second-order theory

2.2.1 Governing equations

We consider unidirectional waves propagating over a horizontal bed in the (x, z) plane, with z measured vertically upward from the still water level, and the free surface located at $z = \eta$. For the irrotational flow of inviscid, incompressible fluid, the governing equation is Laplacian,

$$\nabla^2 \phi = 0 \quad \text{for} \quad -d \leq z \leq \eta, \tag{2.1}$$

where ϕ is the velocity potential and d is the depth. Equation (2.1) is solved subject to the no-flow bottom boundary condition,

$$\frac{\partial \phi}{\partial z} = 0 \quad \text{at} \quad z = -d, \tag{2.2}$$

and the kinematic and dynamic linear free surface boundary conditions,

$$w - \frac{\partial \eta}{\partial t} - u \frac{\partial \eta}{\partial x} = 0 \quad \text{and} \quad g\eta + \frac{\partial \phi}{\partial t} + \frac{1}{2}(\boldsymbol{\nabla}\phi)^2 = 0 \quad \text{at} \quad z = \eta, \tag{2.3a,b}$$

where t is time, g is gravity, and the velocity components are $u = \partial\phi/\partial x$ and $w = \partial\phi/\partial z$.

2.2.2 Solutions using perturbation methods

We begin by carrying out a Stokes expansion using the steepness $\alpha \equiv k_0 a$, where a is the maximum amplitude of the (linear) free surface A_0, and k_0 is the carrier wave number. Using a Taylor-series expansion of the free-surface boundary conditions (2.3a) and (2.3b) about $z = 0$, we obtain after some manipulation (see also [Longuet-Higgins and Stewart, 1964, McAllister et al., 2018]), utilizing the Laplace equation (2.1):

$$\left(\frac{1}{g}\frac{\partial^2}{\partial t^2} + \frac{\partial}{\partial z}\right)\phi^{(2)} =$$

$$\frac{\partial}{\partial x}\left(\frac{\partial \phi^{(1)}}{\partial x}\eta^{(1)}\right) - \frac{1}{g}\frac{\partial}{\partial t}\left(\frac{1}{2}(\boldsymbol{\nabla}\phi^{(1)})^2 + \frac{\partial^2 \phi^{(1)}}{\partial z \partial t}\eta^{(1)}\right) + O(\alpha^3) \quad \text{at} \quad z = 0, \tag{2.4}$$

$$\eta^{(2)} = \frac{-1}{g}\left(\frac{\partial \phi^{(2)}}{\partial t} + \overline{\frac{\partial^2 \phi^{(1)}}{\partial z \partial t}\eta^{(1)} + \frac{1}{2}|\boldsymbol{\nabla}\phi^{(1)}|^2}\right) + O(\alpha^3) \quad \text{at} \quad z = 0, \tag{2.5}$$

where the superscripts denote the order in α, and we only consider terms up to second order in α.

Wave packets can be created by modulating a single-frequency carrier wave with angular frequency ω_0 and wave number k_0. Assuming the length scale of the modulation σ is much larger than the wavelength of the carrier wave allows a multiple-scales expansion in the small parameter $\epsilon \equiv 1/(k_0\sigma)$. The parameter ϵ is a measure of the bandwidth of the spectrum, and the leading-order terms we consider correspond to a narrow-banded spectrum centered around the carrier wave. Accordingly, we have the fast variables x, z, and t and the slow variable $X = \epsilon(x - c_{g,0}t)$, where $c_{g,0} \equiv \partial\omega/\partial k|_{k=k_0} = \omega_0/k_0[1/2 + k_0 d/\sinh(2k_0 d)]$ is the group velocity of the wave packet. Our focus is on leading-order terms; we thus ignore dispersion of the group and its associated higher-order scales. The fast variables allow change on the length scale of the carrier wave, while the slow variables represent changes in the modulation of the wave packet. Derivatives are then expanded for fast and slow variables as

$$\frac{\partial}{\partial x} \to \partial_x + \epsilon\partial_X. \tag{2.6}$$

From here on, $\partial/\partial x$ will be used to denote combined slow and fast derivatives, whereas ∂_x and ∂_X denote fast and slow derivatives, respectively. The overlines in (2.4) and (2.5) correspond to averaging over the fast scales, and we ignore any superharmonic contributions to the second-order terms as they do not contribute to the mean flow. We will now consider the first two orders in α in turn.

First-order in steepness $O(\alpha)$

Similar to [Davey and Stewartson, 1975, Brinch-Nielsen and Jonsson, 1986], we write the $O(\alpha)$ solutions as summations over different orders in ϵ (see also [van den Bremer et al., 2019]),

$$\zeta^{(1)} = \Big\{A_0(X)\ \hat{\zeta}_0(z) + \epsilon A_1(X)\ \hat{\zeta}_1(z)\Big\}\, e^{\imath(k_0 x - \omega_0 t)} + O(\alpha\epsilon^2), \tag{2.7}$$

$$\phi^{(1)} = \Big\{B_0(X)\hat{\phi}_0(z) + \epsilon B_1(X)\hat{\phi}_1(z)\Big\}\, e^{\imath(k_0 x - \omega_0 t)} + O(\alpha\epsilon^2), \tag{2.8}$$

Table 2.2: Expressions for the different linear (in $\alpha \equiv k_0|a_0|$) fields at $O(\alpha^1\epsilon^0)$ and $O(\alpha^1\epsilon^1)$. The actual fields are the real parts of the tabulated expressions after multiplication by $\exp[\imath(k_0x-\omega_0 t)]$.

Linear field	$O(\alpha\epsilon^0)$	$O(\alpha\epsilon^1)$
surface elevation $\eta^{(1)}$	A_0	$\imath\frac{k_0 d}{k_0\tanh(k_0d)}\ \epsilon\partial_X A_0$
velocity potential $\phi^{(1)}$	$-\imath\frac{c_{p,0}}{k_0}\ A_0\ \hat{\zeta}_0'$	$\frac{c_{p,0}}{k_0^2}\ \epsilon\partial_X A_0\left[\hat{\zeta}_1'+(2-c_{g,0}/c_{p,0})\,\hat{\zeta}_0'\right]$
horizontal velocity $u^{(1)}$	$c_{p,0}\ A_0\ \hat{\zeta}_0'$	$\imath\frac{c_{p,0}}{k_0}\ \epsilon\partial_X A_0\left[\hat{\zeta}_1'+(1-c_{g,0}/c_{p,0})\,\hat{\zeta}_0'\right]$
vertical velocity $w^{(1)}$	$-\imath\omega_0\ A_0\ \hat{\zeta}_0$	$c_{p,0}\ \epsilon\partial_X A_0\left(\hat{\zeta}_1-c_{g,0}/c_{p,0}\ \hat{\zeta}_0\right)$
vertical displacement $\zeta^{(1)}$	$A_0\ \hat{\zeta}_0$	$\imath\frac{1}{k_0}\ \epsilon\partial_X A_0\ \hat{\zeta}_1$
horizontal displacement $\xi^{(1)}$	$\imath\frac{1}{k_0}\ \hat{\zeta}_0'$	$-\frac{1}{k_0^2}\ \epsilon\partial_X A_0\left(\hat{\zeta}_1'+\hat{\zeta}_0'\right)$

where the subscripts denote the order in ϵ and we only consider the first two orders. The variable $\zeta^{(1)}$ denotes the linear vertical displacement field, which corresponds to the linear free-surface elevation $\eta^{(1)}$ evaluated at $z=0$, namely $\eta^{(1)}=\zeta^{(1)}(z=0)$, and it can be found from $\partial\zeta^{(1)}/\partial t = w^{(1)}$ [cf. (2.3a)]. The vertical structure functions $\hat{\zeta}_0(z)$, $\hat{\zeta}_1(z)$, $\hat{\phi}_0(z)$, and $\hat{\phi}_1(z)$, with primes denoting derivative with respect to z, have to be chosen so that the Laplace equation (2.1) and the bottom boundary condition (2.2) are satisfied. We find that

$$\hat{\zeta}_0(z)=\frac{\sinh[k_0(d+z)]}{\sinh(k_0d)},\quad \hat{\zeta}_1(z)=a_0\sinh[k_0(d+z)]-\frac{k(d+z)\cosh[k_0(d+z)]}{\sinh(k_0d)}, \tag{2.9}$$

and

$$\begin{aligned}\hat{\phi}_0(z) &= \tfrac{\cosh[k_0(d+z)]}{\sinh(k_0d)},\\ \hat{\phi}_1(z) &= q_0\cosh[k_0(d+z)]-\tfrac{k_0(d+z)\sinh[k_0(d+z)]}{\sinh(k_0d)}+(1-c_{g,0}/c_{p,0})\tfrac{\cosh[k_0(d+z)]}{\sinh(k_0d)},\end{aligned} \tag{2.10}$$

where q_0 can be freely chosen (cf. homogeneous solution) and we set $q_0=0$. Table 2.2 reports all the $O(\alpha)$ polarization relationships expressed in terms of the amplitude envelope of the free surface up to $O(\alpha\epsilon^1)$.

From the linear solution, we can directly evaluate the Stokes drift [Longuet-

Higgins, 1953], which is generally defined by

$$\mathbf{u}_\mathrm{S} \equiv \overline{\frac{\partial \mathbf{u}^{(1)}}{\partial x}\xi^{(1)} + \frac{\partial \mathbf{u}^{(1)}}{\partial z}\zeta^{(1)}}, \tag{2.11}$$

where $\xi^{(1)}$ and $\zeta^{(1)}$ are the linear horizontal and vertical displacements (cf. $\partial\xi^{(1)}/\partial t = u^{(1)}$, $\partial\zeta^{(1)}/\partial t = w^{(1)}$). Using the linear polarization relationships from Table 2.2, we can find explicit expressions for the horizontal and vertical Stokes drift velocities:

$$\begin{aligned} u_\mathrm{S} &= \tfrac{\omega_0 k_0}{2}\tfrac{\cosh[2k_0(d+z)]}{\sinh^2(k_0 d)}|A_0|^2 \quad \text{and} \\ w_\mathrm{S} &= -\tfrac{\omega_0}{4}\left(1+\tfrac{c_{g,0}}{c_{p,0}}\right)\tfrac{\sinh[2k_0(z+d)]}{\sinh^2(k_0 d)}\epsilon\partial_X|A_0|^2. \end{aligned} \tag{2.12a,b}$$

Second order in steepness $O(\alpha^2)$

Seeking a solution for the Eulerian mean-flow potential $\phi^{(2)}$ that varies on the slow scale X and using the linear polarization relationships in Table 2.2, Eq. (2.4) becomes

$$\begin{aligned} \left(\frac{\epsilon^2 c_{g,0}^2}{g}\partial_{XX} + \partial_z\right)\phi^{(2)}(X,z) =& \epsilon\frac{\omega_0\partial_X|A_0|^2}{2\tanh(k_0 d)} + \epsilon c_{g,0}\frac{\omega_0^2\partial_X|A_0|^2}{4g\sinh^2(k_0 d)}, \\ =& \quad \epsilon[1+C_\mathrm{FD}(k_0 d)]\frac{\omega_0\partial_X|A_0|^2}{2\tanh(k_0 d)}, \end{aligned} \tag{2.13}$$

where the coefficient $C_\mathrm{FD}(k_0 d)$ represents terms that only contribute in finite depth:

$$C_\mathrm{FD}(k_0 d) = \frac{c_{g,0}\omega_0}{g\sinh(2k_0 d)} = \frac{k_0 d\,\mathrm{sech}^2(k_0 d) + \tanh(k_0 d)}{2\sinh(2k_0 d)}, \tag{2.14}$$

and in deep-water ($k_0 d \gg 1$) we have $C_\mathrm{FD}(k_0 d) \to 0$.

The forcing equation (2.13) can be solved using a Fourier transform to give

$$\phi^{(2)} = -\frac{\omega_0[1+C_\mathrm{FD}(k_0 d)]}{4\pi\tanh(k_0 d)}\int_{-\infty}^{\infty}\widehat{|A_0|^2}\frac{\cosh[\kappa(z+d)]}{\sinh(\kappa d)}\frac{\imath\exp(\imath\kappa\tilde{x})}{1-\frac{c_{g,0}^2\kappa}{g\tanh(\kappa d)}}\,d\kappa, \tag{2.15}$$

where $\widehat{|A_0|^2}$ is the Fourier transform of $|A_0|^2$ in $\tilde{x}$ and $\tilde{x} \equiv X/\epsilon = x - c_{g,0}t$. The poles of this integral do not make a contribution and they are discussed in Appendix 2.A. Using (2.15), the set-down can then be calculated from (2.5) to be

$$\begin{aligned}\eta^{(2)} = &-\frac{\omega_0^2|A_0|^2}{4g\sinh^2(k_0 d)}\\ &-\frac{c_{g,0}\omega_0[1+C_{\mathrm{FD}}(k_0 d)]}{2g\tanh(k_0 d)}\int_{-\infty}^{\infty}\kappa\widehat{|A_0|^2}\frac{\cosh[\kappa(z+d)]}{\sinh(\kappa d)}\frac{\exp(\imath\kappa\tilde{x})}{1-\frac{c_{g,0}^2\kappa}{g\tanh(\kappa d)}}\,d\kappa \text{ at } z=0. \quad (2.16)\end{aligned}$$

When examining the left-hand side of the forcing equation (2.13), care must be taken with regard to the order of $\phi^{(2)}$. Here, κ is the wave number associated with the wave packet and scales with ϵ. The order of $\phi^{(2)}$ then depends on the order of $k_0 d$. If $k_0 d$ is large (deep-water) and ϵ is small, in such a manner that $d/\sigma = \epsilon k_0 d \gg 1$, it is justified to make the “rigid-lid" approximation by neglecting the set-down. In intermediate depth and with a sufficiently narrow-banded wave packet, the return flow must be shallow, $d/\sigma = O(\epsilon) \ll 1$ [i.e., $\epsilon = 1/(k_0\sigma)$ implies $d/\sigma = k_0 d\epsilon = O(\epsilon)$ when $k_0 d = O(1)$]. Thus, the small-argument approximations of hyperbolic functions can be used [i.e., $\cosh(\kappa d)/\sinh(\kappa d) \to 1/(\kappa d)$]. As a result, $\phi^{(2)}$ becomes one order more significant in ϵ (i.e., $\phi^{(2)}|_{k_0 d=O(1)} \propto \epsilon^{-1}\phi^{(2)}|_{k_0 d\gg 1}$) (see also the discussion in [Peregrine, 1983]). If $k_0 d$ is $O(1)$, the inclusion of $\partial_{XX}\phi^{(2)}$ on the left-hand side of the forcing equation is therefore required (this term was incorrectly ignored in van den Bremer and Taylor [2015]). The subtle change in order of the potential in intermediate depth which leads to the inclusion of the full operator is vital to correctly evaluating the Eulerian return flow.

The relative depth of the return flow (d/σ) can be assumed to be shallow or deep, allowing the integrals in (2.16) and (2.15) to be calculated analytically. Our solution for general d/σ can then be manipulated to recover the results of Longuet-Higgins and Stewart [1962a] and Mei et al. [1989] for $d/\sigma \ll 1$ (shallow return flow), and Dysthe [1979] and van den Bremer and Taylor [2016] for $d/\sigma \gg 1$ (deep return flow) (see Appendix 2.B).

2.2.3 Lagrangian displacements

Arbitrary water depth: $k_0 d = O(1)$ **and** $d/\sigma = O(1)$

The Lagrangian velocity under a wave packet comprises the Stokes drift and the Eulerian return flow, so that $\Delta x_{\mathrm{L}} = \Delta x_{\mathrm{S}} + \Delta x_{\mathrm{E}}$. To allow for a comparison to experiments in which displacements have to be calculated over finite times to avoid the effect of error waves and their reflections, we calculate finite-time Lagrangian displacements. The Stokes drift (2.12) can be readily integrated between t_1 and t_2 to give

$$\Delta x_{\mathrm{S}} = \frac{\omega_0 k_0}{2} \frac{\cosh[2k_0(d+z)]}{\sinh^2(k_0 d)} \int_{t_1}^{t_2} |A_0|^2 dt, \tag{2.17}$$

$$\Delta z_{\mathrm{S}} = -\frac{1}{4}\left(1 + \frac{c_{p,0}}{c_{g,0}}\right) \frac{k_0 \sinh[2k_0(z+d)]}{\sinh^2(k_0 d)} (|A_0|^2_{t=t_2} - |A_0|^2_{t=t_1}). \tag{2.18}$$

In arbitrary water depth, making no assumptions about the scale of the group relative to the depth d/σ and thus about the depth of the return flow, the horizontal and vertical components of the Eulerian return flow are obtained by differentiating (2.15); the displacements are then obtained by integrating over time:

$$2\Delta x_{\mathrm{E}} = -\frac{\omega_0[1 + C_{\mathrm{FD}}(k_0 d)]}{4\pi \tanh(k_0 d)} \int_{t_1}^{t_2} \int_{-\infty}^{\infty} \kappa\widehat{|A_0|^2} \frac{\cosh[\kappa(z+d)]}{\sinh(\kappa d)} \frac{\exp(\imath\kappa\tilde{x})}{1 - \frac{c_{g,0}^2 \kappa}{g \tanh(\kappa d)}} d\kappa\, dt, \tag{2.19}$$

$$2\Delta z_{\mathrm{E}} = -\frac{\omega_0[1 + C_{\mathrm{FD}}(k_0 d)]}{4\pi \tanh(k_0 d)} \int_{t_1}^{t_2} \int_{-\infty}^{\infty} \kappa\widehat{|A_0|^2} \frac{\sinh[\kappa(z+d)]}{\sinh(\kappa d)} \frac{\imath \exp(\imath\kappa\tilde{x})}{1 - \frac{c_{g,0}^2 \kappa}{g \tanh(\kappa d)}} d\kappa\, dt. \tag{2.20}$$

Shallow return flow: $k_0 d = O(1)$ and $d/\sigma \ll 1$

Assuming a shallow return flow ($d/\sigma \ll 1$) enables an explicit solution of the integral over the wave number in (2.15) to be obtained (using the small-argument approximation of the hyperbolic tangent). In that case, the Eulerian flow velocity components become

$$\begin{aligned} u_{\mathrm{E}} &= -\frac{\omega_0[1+C_{\mathrm{FD}}(k_0 d)]}{2\tanh(k_0 d) d\left(1 - \frac{c_{g,0}^2}{gd}\right)} |A_0|^2 \quad \text{and} \\ w_{\mathrm{E}} &= -\frac{\omega_0[1+C_{\mathrm{FD}}(k_0 d)]}{2\tanh(k_0 d)\left(1 - \frac{c_{g,0}^2}{gd}\right)} \frac{(z+d)}{d} \partial_X |A_0|^2. \end{aligned} \tag{2.21a,b}$$

Integrating the horizontal Eulerian velocity when the return flow is shallow (2.21a) and combining with the previously derived horizontal displacement by the Stokes drift (2.17), which is unchanged, we obtain the horizontal Lagrangian displacement over the time interval t_1 to t_2,

$$\Delta x_{\mathrm{L}} = \frac{\omega_0 k_0}{2}\left[\frac{\cosh[2k_0(z+d)]}{\sinh^2(k_0 d)} - \frac{[1+C_{\mathrm{FD}}(k_0 d)]}{k_0\tanh(k_0 d) d\left(1-\frac{c_{g,0}^2}{gd}\right)}\right]\int_{t_2}^{t_1}|A_0|^2 dt, \quad (2.22)$$

where t_1 and t_2 are arbitrary time values. If the group is Gaussian and of the form $A_0 = a_0 \exp\left[-(x-c_{g,0}t)^2/2\sigma^2\right]$ and the time integral is taken over the entire group, such that $t_1 \to -\infty$ is before the arrival of the group and $t_2 \to \infty$ after the group has passed, then we obtain

$$\Delta x_{\mathrm{L}} = \frac{\sqrt{\pi}\omega_0 \alpha^2 \sigma}{2k_0 c_{g,0}}\left[\frac{\cosh[2k_0(z+d)]}{\sinh^2(k_0 d)} - \frac{[1+C_{\mathrm{FD}}(k_0 d)]}{k_0\tanh(k_0 d) d\left(1-\frac{c_{g,0}^2}{gd}\right)}\right]. \quad (2.23)$$

If the effect of the set-down is ignored in (2.23) by not fully accounting for the change in order of the operator on the potential, then $1 - c_{g,0}^2/gd$ would be unity. The vertical Lagrangian displacement component between times t_1 and t_2 is

$$\Delta z_{\mathrm{L}} = \left[\frac{1}{4}\left(1+\frac{c_{p,0}}{c_{g,0}}\right)\frac{k_0\sinh[2k_0(z+d)]}{\sinh^2(k_0 d)} - \frac{\omega_0[1+C_{\mathrm{FD}}(k_0 d)]}{2c_{g,0}\tanh(k_0 d)(1-\frac{c_{g,0}^2}{gd})}\frac{z+d}{d}\right] \times \left(|A_0|^2_{t=t_2} - |A_0|^2_{t=t_1}\right), \quad (2.24)$$

from which we can obtain for the maximum or minimum displacement underneath the center of the group

$$\Delta z_{\mathrm{L}} = \left[\frac{1}{4}\left(1+\frac{c_{p,0}}{c_{g,0}}\right)\frac{\sinh[2k_0(z+d)]}{\sinh^2(k_0 d)} - \frac{\omega_0[1+C_{\mathrm{FD}}(k_0 d)]}{2k_0 c_{g,0}\tanh(k_0 d)\left(1-\frac{c_{g,0}^2}{gd}\right)}\frac{z+d}{d}\right]\frac{\alpha^2}{k_0}. \quad (2.25)$$

Figure 2.1 now examines the effect of ignoring the set-down when computing displacements. As the relative depth $k_0 d$ becomes shallower, the role of the set-down increases, and the continuous lines, which include the effect of the set-down, diverge from the dashed lines, which ignore this effect. This paper sets out to observe this effect experimentally.

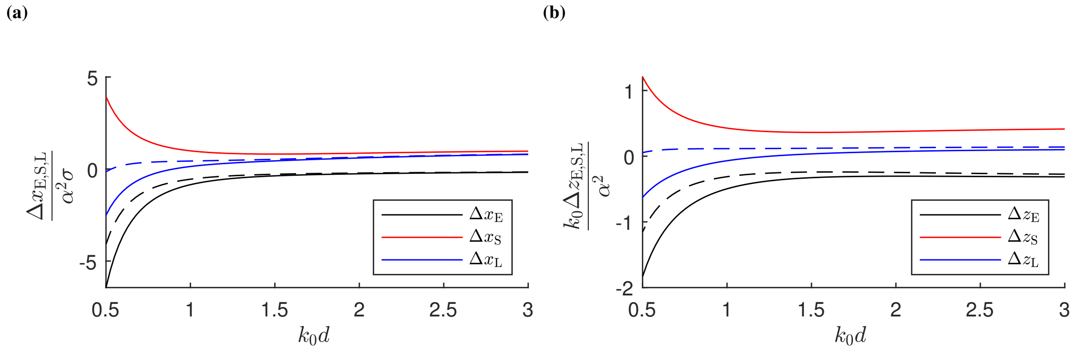

Figure 2.1: Theoretical normalized horizontal (left panel) and vertical (right panel) displacements as a function of the relative depth $k_0 d$ at $z = 0$ [from (2.23) and (2.25)]. The displacements by the Eulerian mean flow displacement are shown as black lines, the displacements by the Stokes drift are shown by red lines, and the Lagrangian displacements are shown by blue lines. The solid lines show the displacements when the set-down is fully accounted for by including the full operator on the potential because of the change in order of epsilon due the change in relative water depth, whereas the dashed lines ignore the set-down and its effect on the operator.

2.3 Experimental methodology

2.3.1 Setup and data acquisition

To validate the predicted particle trajectories under a wave packet, a series of particle tracking velocimetry (PTV) experiments were undertaken in the Sediment Wave Flume in the Coastal, Ocean and Sediment Transport (COAST) Laboratory, University of Plymouth, UK. The flume has a length of 35 m, a width of 0.60 m, and was filled with water to a depth of 0.50 m, as shown in Fig. 2.2. We used a double-element piston-type wavemaker to generate a focused wave packet with a spectral shape that linearly focuses to a Gaussian packet $A_0 = a_0 \exp\left[-(x_f - c_{g,0}t)^2/2\sigma^2\right]$ at a measurement zone located $x_f = 19.75$ m from the resting position of the wavemaker. Seven resistance-type wave gauges provided 128 Hz free-surface elevation measurements. A light-emitting diode (LED) light box illuminated the motions of small near-neutrally buoyant particles in a plane, which were captured by a camera positioned outside the flume. After propagating through the measurement zone, the dispersed wave packets were absorbed by mesh-filled wedges within an “absorption zone" located at the downstream end of the wave flume. The distance to the measurement zone was prescribed to allow as much separation as possible of the subharmonic error wave from the group, while also avoiding reflections. To ensure near-quiescent initial conditions for each experiment, the water surface was allowed to settle for 10 min between experiments. The settling time of 10 min was short enough that the slightly positively buoyant particles remained evenly distributed throughout the water column at the start of each experiment.

Fluid trajectories were measured by tracking a large number of illuminated small-diameter seeding particles within the flow. These “Plascoat" particles were approximately 150 μm in diameter, small enough to be considered dynamically unimportant. Although the particles were slightly positively buoyant, their upward settling velocities were negligible compared to their motion beneath the free-surface waves. The particles were effectively uniformly mixed throughout the measurement zone, which was achieved by adding new particles between experiments when necessary, mixing up the water column, and waiting for the flume to become quiescent before starting experiments. Due to the light sheet, only particles in a thin slice in the (x-z) plane were tracked. The camera field of view was not able to capture the full depth of the flume. Thus, to obtain a complete coverage of the water column, the same experiment was repeated three times. Ambient lighting was removed while a Photron SA4 high-speed camera captured the particle motions at 125 frames/s, at a resolution of 1024 by 1024 pixels and a shutter speed of 1/125 s. This shutter speed achieved an acceptable compromise between the requirements of obtaining very sharp images and allowing sufficient light to enter the camera during each image exposure. An image of a ruler was used to quantify the pixel scale, and distortion was found to be negligible for these tests.

2.3.2 Wave generation

If operated using a first-order signal, a wavemaker will generate spurious error waves (see, e.g., [Nielsen and Baldock, 2010, Orszaghova et al., 2014] for a discussion on the effects of these error waves). To partially eliminate the generation of these error waves, the second-order corrections of Schäffer [1996] were applied to the wavemaker signal. The Edinburgh Designs Ltd. (EDL) wavemaker differs from an idealized piston-type wavemaker in two ways. First, the EDL wavemaker is a double-element paddle, which does not extend to the base of the flume. Second, the paddle does not have the range of movement required to eliminate subharmonic error waves in finite water depth. As a result,

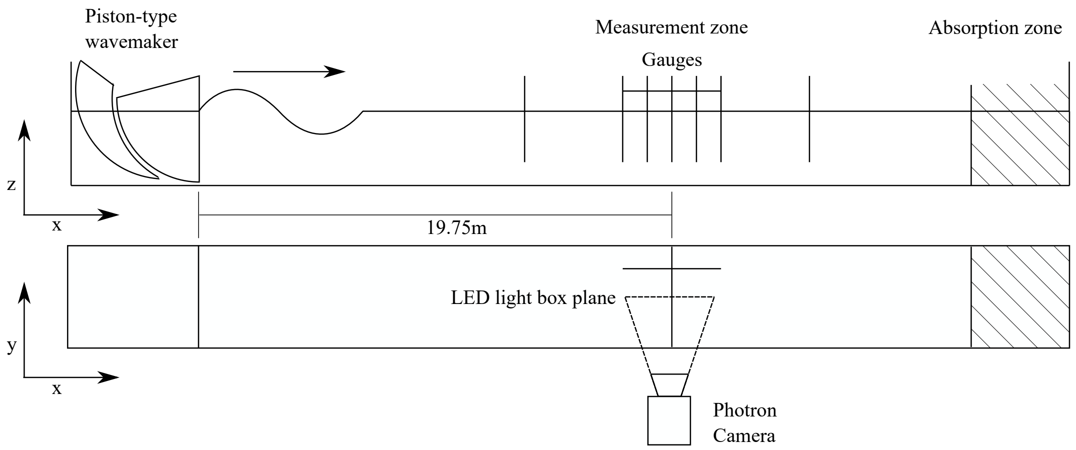

Figure 2.2: Experimental setup used to obtain PTV measurements of fluid trajectories beneath focused wave packets generated by a double-element piston-type wavemaker at the COAST laboratory, University of Plymouth, UK.

error waves were not completely removed by the correction method (see also [Sriram et al., 2015]). Whittaker et al. [2017] concluded that the subharmonic error wave amplitude was reduced by approximately 60% in similar conditions. In our case, subharmonic error waves had relatively large amplitude due to the finite-depth nature of experiments (finite k_0d), and they caused significant difficulty when calculating the displacements discussed in Sec. 2.4.1.

2.3.3 Matrix of experiments

Table 2.3 lists the parameters for the nine experiments we conducted, varying the relative water depth k_0d and the bandwidth ϵ. Frequencies were chosen such that the water depth is “intermediate" ($k_0d \approx$ 1–3); amplitudes such that second-order motions are large enough to measure, but not so large so that effects beyond second-order play a role; and the bandwidth parameter $\epsilon = 1/(k_0\sigma)$ such that the wave packet is still quasimonochromatic, but not so long that reflections play a role.

2.3.4 Data processing and removal of background motion

The free surface was measured using seven resistance wave gauges, five spread around the focus location and two significant distances before and after the focus location. The wave packets were deliberately chosen to have a narrow-

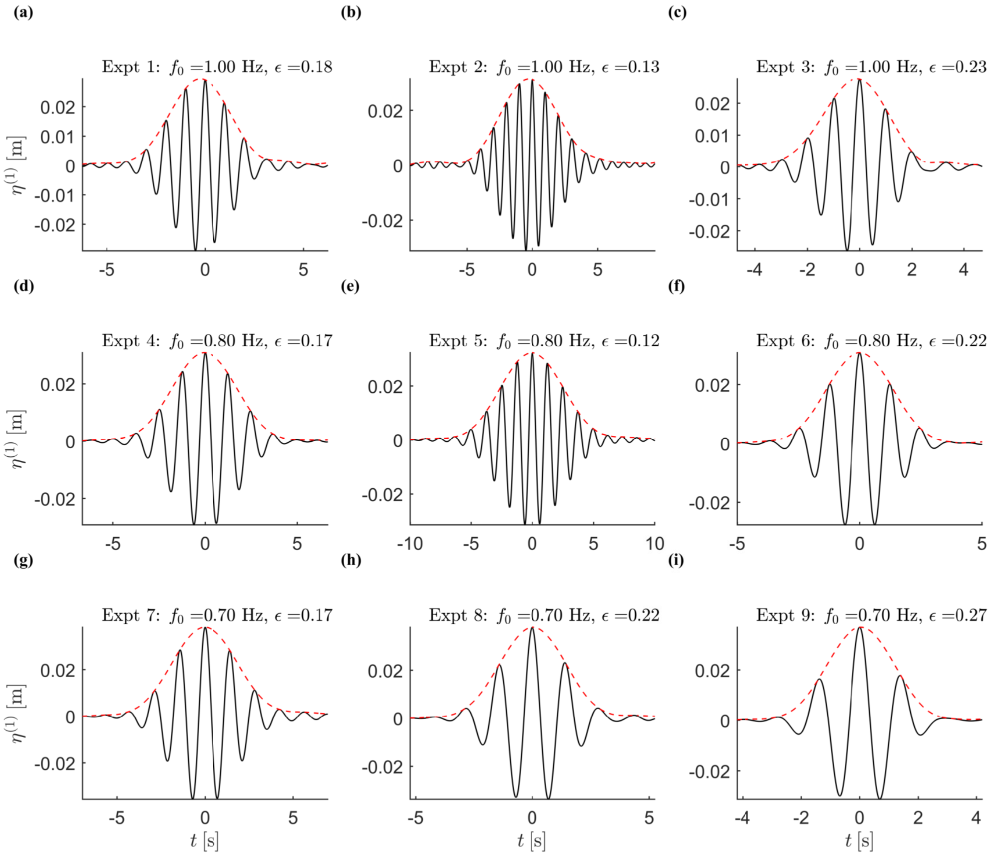

Figure 2.3: The experimental linear free surface elevation measured at the focus location (black lines). The linear part has been extracted with a band-pass filter between $0.7f_0$ and $1.3f_0$. The envelope (red dashes lines) has been calculated using a Hilbert transform of the linear free surface.

banded spectrum to allow frequency filtering to separate the linear and second-order subharmonic parts from the wave gauge signal. This was achieved using a low-pass filter of $0.5f_0$ to separate the subharmonic set-down and a band-pass filter between $0.7f_0$ and $1.3f_0$ to extract the linear free-surface elevation. The linear free-surface elevation is shown in Fig. 2.3, along with the measured envelope $|A_0|$. The measured envelope is calculated using the Hilbert transform of the linear free-surface elevation, which in turn is used to predict the mean flow using (2.22). The use of the measured envelope at the location where the trajectories are measured accounts for any dissipation or nonlinear dispersion, which may occur between the wavemaker and the measurement zone.

The recorded images were processed using STREAMS software, a specialist package for flow visualization applications [Nokes, 2014]. Particles within each image were identified using a dual threshold algorithm, which first searched for pixels of intensity greater than a threshold value, identified the maximum pixel intensity within the group of pixels, and finally defined particle boundaries based on a fraction of this maximum intensity. The identified particles were subsequently matched between frames using an "auction" optimization algorithm, which minimized the total cost of all potential matches for each successive pair of frames, where the cost was first assigned based on particle distance, then based on matched particle velocities in a small region. Recent velocities of matched particles were finally used to generate additional matches where appropriate. Lagrangian paths were then calculated and stored for post-processing.

Background motion and the motion due to the subharmonic error wave had to be eliminated in order to calculate the displacement due to Stokes drift and Eulerian return flow. The background motion is much slower than the desired measured Lagrangian motion, and it consists of a combination of a rise velocity of the particles, long waves that decay slowly in the flume, circulation induced by small air flows over the water surface, which cannot be eliminated in the laboratory, and mixing-induced motion. The Stokes rise velocity of the spherical particles can be estimated as $w = (2/9)[(\rho_w - \rho_p)/\rho_w](gR^2/\nu) = 0.49$ mm/s, where we have used $\rho_p = 0.96$ g/cm^3 (density of Plascoat particle), $\rho_w = 1.00$ g/cm^3 (density of water), $\nu = 1.0 \times 10^{-6}$ m^2/s (viscosity of water), and $R = 75 \times 10^{-6}$ m (radius of Plascoat particle). This is much slower than the motion induced by the waves. The smallest amplitudes of wave-induced motion at focus are $u_S = 17.7$ mm/s and $U_E = 6.7$ mm/s, which are significantly larger than the rise velocity of 0.49 mm/s. This permitted a suitable curve fit to the trajectories before and/or after the focused wave packet to be subtracted from the original $x(t)$ and $z(t)$ trajectories. The most successful fitting method was then selected by studying the frequency spectrum of the trajectories after the curve fit had been subtracted. The exact procedure is described in Appendix 2.C.

Table 2.3: Matrix of experiments.

Experiment	Peak frequency f_0 (Hz)	Steepness $\alpha = k_0 a_0$	Bandwidth $\epsilon = (k_0\sigma)^{-1}$	Relative depth $k_0 d$
1	1.00	0.12	0.18	2.08
2	1.00	0.13	0.13	2.08
3	1.00	0.12	0.23	2.08
4	0.80	0.09	0.17	1.44
5	0.80	0.09	0.12	1.44
6	0.80	0.09	0.22	1.44
7	0.70	0.09	0.17	1.18
8	0.70	0.09	0.22	1.18
9	0.70	0.09	0.27	1.18

2.4 Results

2.4.1 The subharmonic free-surface elevation: Set-down and error waves

Figure 2.4 shows the experimental second-order subharmonic free-surface elevation time series, calculated by filtering the free-surface elevation at $0.5 f_0$. Each experiment clearly exhibits a set-down at the center of the group ($t = 0$). Close to focus, the set-down matches the theoretical curve well, and the maximum of the experimental set-down is very close to the theoretical. However, “shoulders" can be seen on either side of the experimental set-down. These shoulders are not to be confused with the predicted set-down shape in nonshallow return flow. The left shoulder corresponds to the subharmonic error wave propagating in the positive x-direction ahead of the group (and its bound set-down), and the right shoulder corresponds to its reflection traveling in the opposite direction. Because of its length relative to the water depth, the subharmonic error wave travels at the shallow water speed ($\sqrt{gd}$).

Figure 2.5 shows the time series of the subharmonic wave components at seven wave gauges plotted with an offset proportional to their respective distance from the focus location. Straight lines denote the propagation speeds of the different features: the positive group speed $c_{g,0}$ for the set-down, the positive shallow-water speed $\sqrt{gd}$ for the subharmonic error wave (left shoulder), and the negative shallow-water speed $-\sqrt{gd}$ for its reflection (right shoulder). The error wave is larger and less separated in the shallower experiments (experiment 4–9 in Figs. 2.4 and 2.5), which is as expected because the second-order signal given to the paddle is produced less well and the error wave is consequently larger, and the difference between the group and the shallow-water speeds is smaller in these cases.

Based on the three repetitions we carried out for each experiment, we can quantify the repeatability and quantify the measurement error associated with the (small) set-down. The left panel of Fig. 2.6 shows an example of this for experiment 5 (where $f_0 = 0.80$ Hz and $\epsilon = 0.12$), with the three repeats plotted as a function of time along with the mean and confidence region of ± 2 standard deviations. The set-down of the three experiments shows remarkable repeatability, even though the maximum value of the set-down is only 1.2 mm. The gray confidence band of ± 2 standard deviations captures the theoretically predicted magnitude of the set-down (dashed red line), though there is an error in the time structure and alignment. The right panel of Fig. 2.6 shows the measured magnitude of the set-down as a function of the theoretically predicted value for all experiments, with the 45° line corresponding to perfect agreement. The error bars in this panel are not estimated from repeats but from the (absolute) calibration error of the gauges, giving generally larger confidence bands than the error estimated from repeats. A good agreement between theory and experiments is generally evident for the magnitude of the set-down underneath the center of the group, where the error waves have not been reached for all experiments.

In the same way that the return flow underneath the set-down leads to a negative displacement of particles, the subharmonic error wave (a setup traveling to the right) gives rise to positive displacement of particles, and its reflection (a setup traveling to the left) to negative displacement. In experiments 4–9, the error wave did not separate out from the group before the group arrived at the focus location. Instead of calculating the true net displacement, in all experiments a small window ($t_1 = -0.1\sigma/c_{g,0}$, $t_2 = 0.1\sigma/c_{g,0}$) has been used to calculate the horizontal displacement to avoid including any error wave in the displacement. See Appendix 2.C for more details.

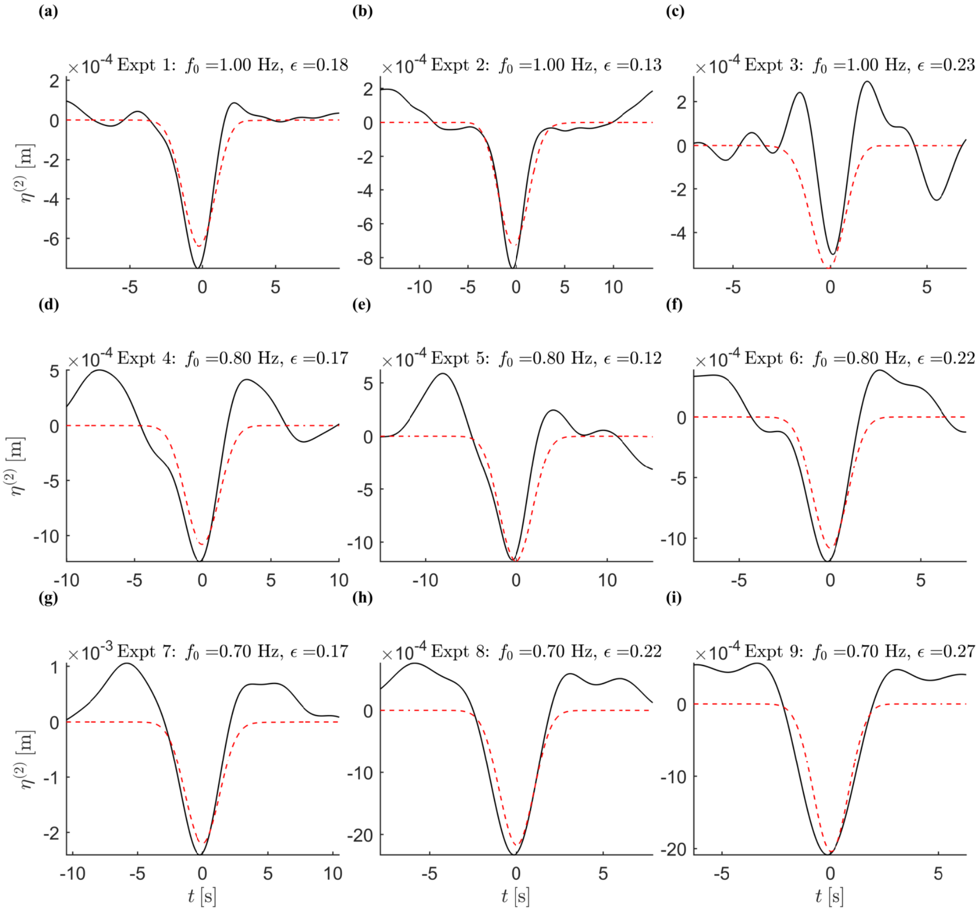

Figure 2.4: Time series of the subharmonic components of the free surface elevation representing a “set-down," from experiments (solid black lines), extracted from the free surface elevation by a low-pass filter at $0.5f_0$, and theory (dashed red lines) for the different experiments.

2.4.2 Particle trajectories

Figure 2.7 shows typical trajectories of particles under wave packets before removal of the background motion. The trajectories are all for experiment 1 ($f_0 = 1.0$ Hz and $\epsilon = 0.18$). As denoted by the vertical axis, the left panel is closest to the free surface, the middle panel is lower, and the right panel is the deepest down in the water column. Near the free surface, there is a positive displacement because Stokes drift is dominant (shown in the left panel). Further down in the water column, the displacement reduces and changes sign; this is when the Stokes drift and the Eulerian return flow are balanced (the middle panel). Toward the bottom of the tank (right panel), there is still strong

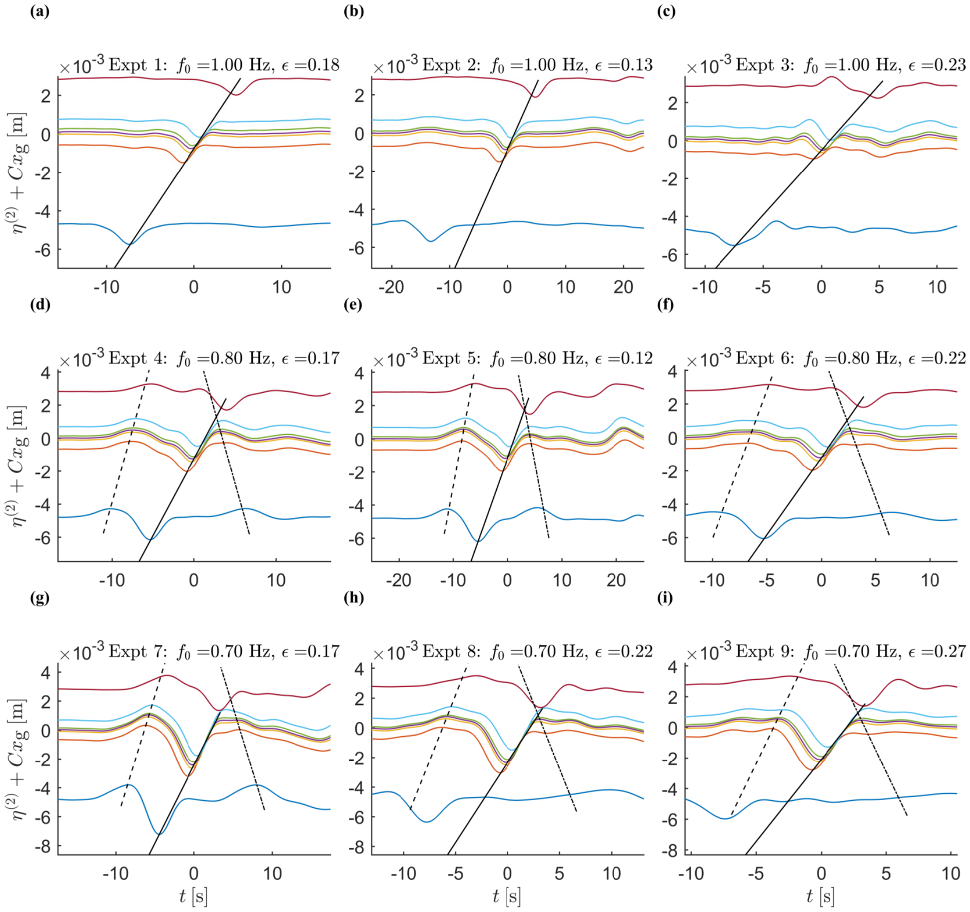

Figure 2.5: Time series of the subharmonic components of the free surface at each wave gauge (extracted from the free surface elevation using a low-pass filter at $0.5f_0$). The y-axis is offset by the product of the distance of each gauge from the focus location x_g and $C = 8.0 \times 10^{-4}$. Also shown are the group speed of the wave packet $c_{g,0}$ with which the set-down moves (continuous black lines which have been set to go through the negative peak of the set-down at the focus time and location), the speed of the error wave $\sqrt{gd}$ (dashed black lines which have been set to go through the peak of the 'hump' just before (in time) the wavepacket at the focus location using the maximum of fitted Gaussian), and the speed of its reflection $-\sqrt{gd}$ (dash-dotted black lines set in the same way as forward travelling error wave).

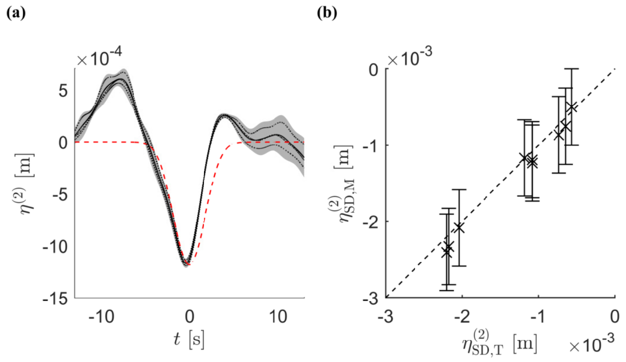

Figure 2.6: Quantification of the measurement error of the set-down. Panel (a) shows the subharmonic set-down for experiment 5 ($f_0 = 0.88$ Hz, $\epsilon = 0.12$) as a function of time: three repeats are plotted using black dotted lines, and the mean is overlaid in solid black. The gray region shows a confidence band of ±2 standard deviations around the mean. The theoretical set-down is plotted using a dashed red line. Panel (b) is a comparison of the magnitude of the set-down between the theoretical (labeled $\eta^{(2)}_{\mathrm{SD,T}}$ on the horizontal axis) and experimentally measured (labeled $\eta^{(2)}_{\mathrm{SD,M}}$ on the vertical axis) magnitude of the set-down for each experiment. The error bars show ±2 standard deviations of the absolute calibration error.

evidence of the waves in the trajectories (shown by the oscillatory motion) because these waves are finite-depth. However, the Eulerian mean flow dominates the drift, and the particles move in the opposite direction (right to left) to that of wave propagation (left to right). Note that there is a small net vertical displacement in Fig. 2.7, as the background motion has not yet been removed. The predicted and experimentally measured depth profiles after removal of the background motion are examined in the next section.

2.4.3 Horizontal Lagrangian displacements

Figure 2.8 compares the measured horizontal particle displacements with theoretical predictions based on the measured (linearized) free-surface elevation. As discussed in Sec. 2.4.1, the displacements are calculated over the interval $t_1 = -0.1\sigma/c_{g,0}$ to $t_2 = 0.1\sigma/c_{g,0}$, where $t = 0$ is the focus time. The short time integral window ($t_2 - t_2 = 0.2\sigma c_{g,0}$) was used to avoid including displacements induced by the subharmonic error wave. The packet length scale σ and the group velocity of the carrier $c_{g,0}$ were estimated from fitting a Gaussian to the measured free-surface signal. As expected, for an irrotational flow, Stokes drift

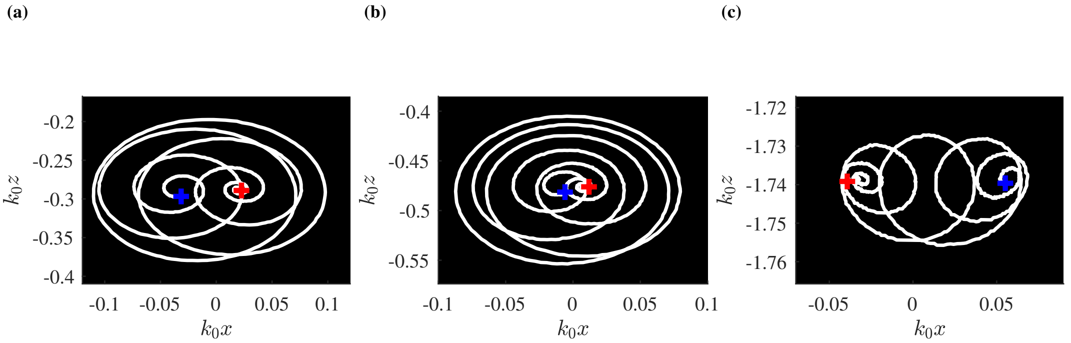

Figure 2.7: Experimental particle trajectories under wave packets with $f_0 = 1.00$ Hz and $\epsilon = 0.18$ at three different depths and before removal of the background motion. The left panel is closest to the surface, the central panel is close to the vertical position where there is no mean drift, and the right panel is the deepest trajectory, showing the large negative mean flow. The blue and red crosses denote the position before the wave packet has arrived and after it has passed, respectively.

dominates at the top of the water column resulting in positive displacements, while the Eulerian return flow causes opposite displacements, which dominate at depth.

Figure 2.8 includes two theoretical predictions: including the effect of the set-down (2.22) (continuous red lines) and excluding the set-down (dotted black lines). To predict the displacement using (2.22), we use the envelope A_0 obtained from a Hilbert transform of the linearized free-surface elevation. To exclude the set-down, we replace the term $[1 - c_{g,0}^2/(gd)]$ in the denominator of the second term in the square brackets in (2.22) by 1. It is immediately evident from Fig. 2.8 that agreement between measurements and theoretical predictions indeed requires inclusion of the set-down. Including the effect of the set-down can be likened to a convergent-divergent duct, thus accelerating the Eulerian mean flow and resulting in a larger velocity underneath the center of the group. The set-down grows in magnitude as the carrier wave gets shallower (f_0 decreases) and thus forces the mean flow more significantly. As the carrier waves get shallower, $c_{g,0}^2/(gd)$ approaches 1, and thus the change in denominator creates a very large difference in the predicted return flow. This can be observed in Fig. 2.8 by the increase in difference between the two theoretical lines as f_0 decreases (lower rows). For the experiments with the greatest depth (experiments 1–3, $k_0 d = 2.1$), the importance of the set-down is minimal, as is evident by the small difference between the two theoretical lines. However, for the shallower cases (experiments 4–6, $k_0d = 1.4$; experiments 7–9, $k_0d = 1.2$), it is evident that the prediction including the set-down is far better than without. For completeness, we note that the agreement for the shallower experiments is less good, likely as a result of the more dominant role of imperfectly eliminated error waves in these cases.

In Fig. 2.8, the bandwidth ϵ [$\epsilon \equiv 1/(k_0\sigma)$, with σ the group length] is varied for each frequency (each panel in a particular row has a different ϵ). One can observe an increase in the magnitudes of the transport with a reduction in ϵ: the narrower the bandwidth ϵ, the longer the wave packet. Figure 2.9 shows scaled and nondimensional measured horizontal displacement profiles, allowing experiments at the same relative depth k_0d but a different group length $\sigma = 1/(k_0\epsilon)$ to be overlaid. The nondimensional horizontal displacements collapse onto a single curve for the three values of k_0d considered.

It is evident from the results that there is a mean transport observed under two-dimensional wave packets, which can be decomposed into Stokes drift and an Eulerian return flow. Stokes drift is dominant near the surface, as is evident from the positive transport near the surface, and its decay with depth matches the theory well. It is worth noting that although the displacement by Stokes drift decays with depth, the displacement by the Eulerian return flow is constant with depth. This can be seen in Eq. (2.22) and is consistent with the observed measured displacements.

Although the net vertical displacement by a group is zero, the measured vertical displacement underneath the center of the group can also be compared to theory. Although the data are subject to more noise, experiments and theory also agree well here (see Appendix 2.D).

2.5 Conclusions

In this paper, we have derived from the water wave equations an expression for wave-induced Eulerian mean flow for a quasi-monochromatic or narrow-banded surface gravity wave packet that is valid for arbitrary water depth relative to both the carrier wave and the wave packet (or return flow) scale. In doing so, we have generalized previous results in the literature that are valid for packets and their return flows that are either very short ($d/\sigma \gg 1$) or very long relative

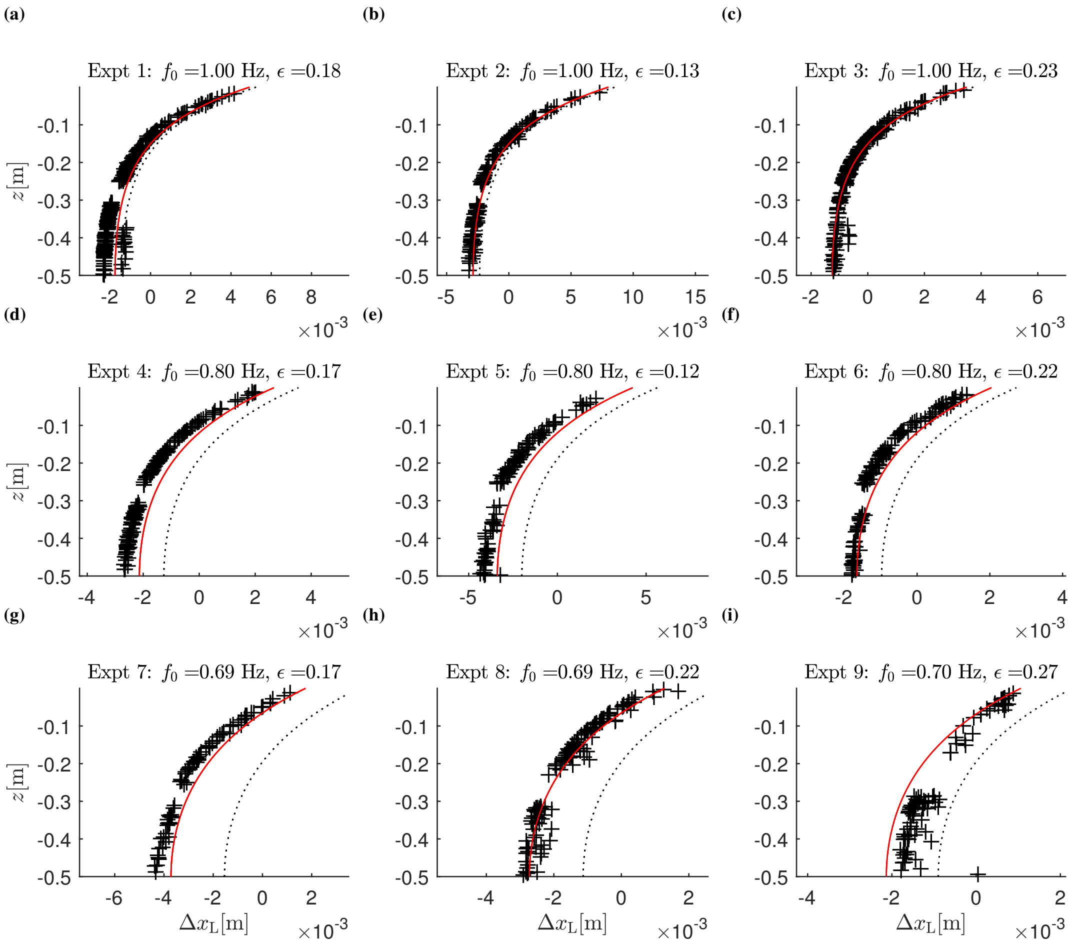

Figure 2.8: Profiles of horizontal Lagrangian displacement between $t_1 = -0.1\sigma/c_{g,0}$ and $t_2 = 0.1\sigma/c_{g,0}$ (with $t = 0$ the center of the packet) as a function of depth: postprocessed experimental data (black crosses), theoretical prediction from (2.22) (continuous red lines), and theoretical prediction ignoring the set-down from (2.22) (dotted black lines). The theoretical prediction ignoring the set-down is obtained by replacing the term $[1-c_{g,0}^2/(gd)]$ in the denominator of the second term in the square brackets in (2.22) by 1.

to the water depth ($d/\sigma \ll 1$), referred to by us as shallow and deep return-flow, respectively. Furthermore, we have corrected van den Bremer and Taylor [2015], who did take into account the effect of finite depth, but incompletely so, by ignoring the set-down. Physically, we explain the mechanism by which set-down enhances the mean flow in finite depth, namely by acting as a convergent-divergent duct.

There has been some disagreement in the literature about whether a net drift should be observed in a laboratory wave flume (see the discussion in [Monismith et al., 2007, Grue and Kolaas, 2017, van den Bremer and Breivik, 2017,

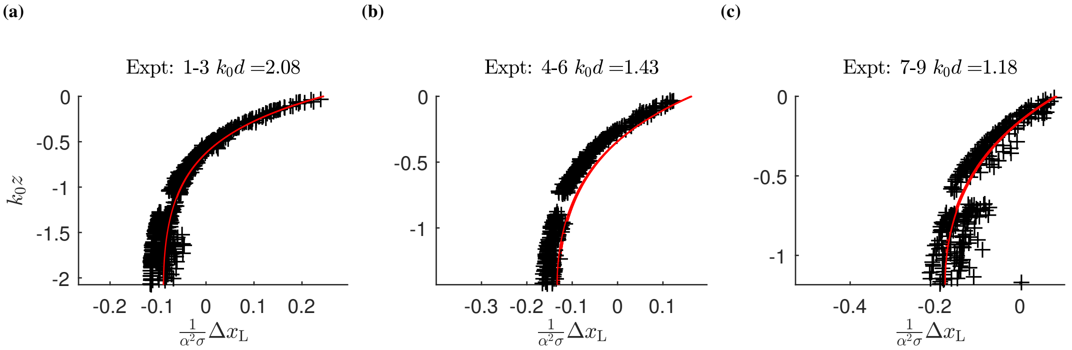

Figure 2.9: Scaled, nondimensional profiles of horizontal Lagrangian displacement between $t_1 = -0.1\sigma/c_{g,0}$ and $t_2 = 0.1\sigma/c_{g,0}$ (with $t = 0$ the center of the packet) as a function of depth: postprocessed experimental data (black crosses) and theoretical predictions from (2.22) (continuous red lines).

Deike et al., 2017]). We have clearly shown in this paper that for the relatively short groups considered, observations are in good agreement with leading-order equations of the irrotational water wave equations in two dimensions. These equations predict a net drift under wave packets in irrotational flows. The resulting displacement is the result of both the Stokes drift and the Eulerian return flow. The Stokes drift displacement is positive (in the direction of the waves) and decays with depth on the scale of the carrier wavelength. The displacement induced by the return flow is negative and does not vary as a function of the vertical coordinate, as predicted both in the shallow return flow and in the deep return flow regimes.

Experiments were designed to extract Lagrangian particle displacements for wave packets in finite depth ($k_0 d = 1.2$–2.2) in a flume without full second-order wave-generation, where the error wave is of significant amplitude and travels at a similar speed to the wave packet. The processing technique accounted for motion from the error wave and eliminated other background motion of the Lagrangian seeding particles. The effect of set-down in these experiments was clear, and the theoretical solution was found to match the experimental measurements far better than if the contribution from the set-down forcing was excluded. The experimental methodology presented herein enables mean flows to be measured in finite water depth despite the presence of an error wave. Although full second-order wave generation is preferable, such generation will be physically constrained in many wavemakers by the maximum length of the paddle sweep and its inability to generate all the slow bound subharmonic components of the signal. Careful consideration of the error wave through fitting methods on the mean flow will then be necessary, as demonstrated herein.

In shallow coastal waters, where the set-down under wave packets is significant, the increase in mean flow found herein would significantly effect transport of pollutants (such as plastic, oil, wreckage, and sediment). Transport by the return flow is opposite to the direction of wave propagation, and, unlike the transport by the Stokes drift, it does not decay with depth.

Acknowledgments

T.S.v.d.B. was supported by a Royal Academy of Engineering Research Fellowship. The authors wish to thank Christopher Higgins and Yan Li for helpful discussions.

Appendix

2.A Analysis of poles in wave-number integral

In the solution to $\phi^{(2)}$ (2.15) there are three poles in the integral over wave number. The first is at $\kappa = 0$ and can be considered inconsequential because it only exists in the potential and disappears once spatially differentiated to velocity; $\kappa = 0$ corresponds to a mean increase in potential (infinite wavelength), which has no physical interpretation. The second and third poles are symmetrical and stem from $\left[1 - c_{g,0}^2\kappa/(g\tanh\kappa d)\right]^{-1}$, which we shall define as $1/f(\kappa)$. The poles are at $\pm\kappa_p$ only if the gradient $c_{g,0}^2/gd < 1$, which is true for all cases other than at the limit of shallow water where $c_{g,0}^2/(gd) = 1$. If $f(\kappa)$ is expanded around κ_p in a Taylor series, it can be shown that $f'(\kappa)$ is an odd function. Thus, when combined with the other terms in the equation for velocity, the two symmetric poles will cancel each other out upon integration.

2.B Comparison with existing literature

The theory presented in Sec. 2.2 describes a single solution for mean flow in water of arbitrary depth. Table 2.1 shows the regimes characterized by relative depths k_0d and d/σ. In this appendix, the solution is shown to recover the results of these established regimes, and a return flow is modeled in an arbitrary depth, either of the carrier wave (k_0d) or the return flow (d/σ).

2.B.1 Shallow return flow: $k_0d = O(1)$ and $d/\sigma \ll 1$

The solution for $\phi^{(2)}$ in (2.15) does not make an assumption regarding the depth of the return flow. If the return flow is assumed to be shallow ($d/\sigma \ll 1$), after differentiation to obtain horizontal velocity, (2.15) simplifies to

$$u^{(2)} = -\frac{\omega_0[1 + C_{\mathrm{FD}}(k_0 d)]}{4\pi \tanh(k_0 d)\left(1 - \frac{c_{g,0}^2}{gd}\right)} \int_{-\infty}^{\infty} \kappa \widehat{|A_0|^2} \frac{\exp(\imath \kappa \tilde{x})}{\kappa d} d\kappa, \tag{2.26}$$

and we can explicitly evaluate (2.16):

$$\eta^{(2)} = -\frac{c_{g,0}}{g} \frac{[1 + C_{\mathrm{FD}}(k_0 d)]}{2 \tanh(k_0 d)(gd - c_{g,0}^2)} g|A_0|^2 - \frac{\omega_0^2 |A_0|^2}{4g \sinh^2(k_0 d)}, \tag{2.27}$$

which can be rewritten as

$$\eta^{(2)} = -\frac{K(c_{g,0}^2/g)|A_0|^2}{gd - c_{g,0}^2} - \frac{\omega_0^2 |A_0|^2}{4g \sinh^2(k_0 d)}, \tag{2.28}$$

where

$$K = \frac{\omega_0^2}{4 \sinh^2(k_0 d)} \left[\frac{\sinh(4k_0 d) + 3\sinh(2k_0 d) + 2k_0 d}{2k_0 d + \sinh(2k_0 d)} \right]. \tag{2.29}$$

Equation (2.28) is identical to (3.17b) obtained by Longuet-Higgins and Stewart [1962a] under the assumption of a shallow return flow when solving for the potential [ϕ in Eq. (3.17a) of Longuet-Higgins and Stewart [1962a]]. Note that Longuet-Higgins and Stewart initially represent the wave packet A_0 as a sum of difference waves, which are waves with phase equal to the difference between that of the linear components, and they do not take a multiple-scales approach.

The two terms on right-hand side of (2.28) can be combined using a rearranged relation for group velocity, $k_0 d/\sinh(2k_0 d) = c_{g,0}/c_{p,0} - 1/2$, to give

$$\eta^{(2)} = -\frac{g|A_0|^2}{2(gd - c_{g,0}^2)} \left[\frac{2c_{g,0}}{c_{p,0}} - \frac{1}{2} \right], \tag{2.30}$$

which is the same as Eq. (11.4.4) obtained by Mei et al. [1989] through a multiple-scales approach similar to ours.

2.B.2 Deep return flow: $k_0 d \gg 1$ and $d/\sigma \gg 1$

Using their nondimensional notation, our forcing Eqs. (2.5) and (2.13) can be rewritten as (2.20) and (2.21) in Dysthe [1979]. As noted by Dysthe [1979], the $\epsilon^2 \partial_{XX} \phi^{(2)}$ term in (2.13) can be ignored in deep water, and an explicit solution for the return flow velocity can be found [van den Bremer and Taylor, 2016],

$$2u^{(2)} = -\frac{\omega_0}{4\pi} \int_{-\infty}^{\infty} \kappa \widehat{|A_0|^2} \exp(\kappa z) \exp(\imath \kappa \tilde{x}) d\kappa. \tag{2.31}$$

2.C Trajectory processing

The raw motion of the seeding particles also included background motion and motion due to the error wave, which was significantly larger in the shallower experiments. This motion had to be eliminated, and a suitable interval to calculate displacements used to achieve good agreement of the experimentally measured displacements with the theory. The background motion of particles is much slower than the Stokes drift and the Eulerian return flow beneath the group. We eliminated background motion using a suitable curve fit (selected from four possible fits) to the motion of the particles over specified time interval(s) before and/or after the arrival of the focused wave packet, and then we subtracted the fit from the original $x(t)$ and $z(t)$ trajectories. The postprocessing algorithm first identified the focus time t_f within the record as the time of the maximum horizontal velocity, and calculated the group velocity $c_{g,0}$, and hence the group period T_g, by solving the linear dispersion equation based on the modulation of the linear surface signal, A_0. The group period formed the basis of the “fit windows" used by the different curve fit options:

(a) Linear fit to x-displacement prior to the wave-packet arrival ($t_f - 6T_g$ to $t_f - 3T_g$), quadratic fit to z-displacement before and after the wave-packet arrival ($t_f \pm 6T_g$ to $t_f \pm 3T_g$).

(b) Linear fit to x-displacement prior to the wave-packet arrival ($t_f - 12T_g$ to $t_f - 9T_g$), quadratic fit to z-displacement before and after the wave-packet arrival ($t_f \pm 9T_g$ to $t_f \pm 3T_g$).

(c) Linear fit to x-displacement prior to the wave-packet arrival ($t_f - 12T_g$ to $t_f - 3T_g$), quadratic fit to z-displacement before and after the wave-packet arrival ($t_f \pm 12T_g$ to $t_f \pm 3T_g$).

(d) Linear fit to x-displacement prior to the wave-packet arrival ($t_f - 9T_g$ to $t_f - 3T_g$), quadratic fit to z-displacement before and after the wave-packet arrival ($t_f \pm 9T_g$ to $t_f \pm 3T_g$).

Once the fits to the raw motions had been carried out, the frequency spectrum of the motion was examined (the motion was first mirrored to create a periodic signal). Using the knowledge that for narrow-banded wave packets the subharmonic and periodic motion should be well-separated (this is not the case for background motion if this is not periodic), the fitting method that led to the frequency spectrum that was most separated was chosen for each trajectory.

The remaining signal was then filtered with a low-pass filter to eliminate the periodic motion; this allowed an accumulated displacement over any time to be compared with theory. For the horizontal motion, an interval of $\pm 0.1\sigma/c_{g,0}$ was used to avoid displacement by the error wave. The vertical displacements were measured over half of the wave packet before the time of focus ($t_1 = -3T_g$ and $t_2 = 0$). If only a small window before focus was used for the vertical displacement, the measurements became very small and dominated by noise.

2.D Vertical Lagrangian displacements

Figure 2.10 compares the measured vertical Lagrangian displacement profiles with theoretical predictions based on the measured (linearized) free-surface elevation from (2.24). The time integral in (2.24) has been taken from before the group arrives ($t_1 = -3\sigma/c_{g,0}$) to the focus time ($t_2 = 0$). The agreement between measured and predicted vertical displacements appears less satisfactory than for horizontal displacements because the values are an order of magnitude smaller, leading to larger relative errors. Even so, measurements capture predictions in terms of their shape and magnitude, including zero vertical displacements at the bottom, negative displacements at mid-depth due to the return flow, and positive displacements near the free surface due to Stokes drift. Measurements and theory agree better in deeper water (experiments 1–3 compared to experiments 4–9). This is most likely because the effect of the error wave is larger in the shallower cases. Figure 2.11 shows scaled and nondimensional measured vertical displacement profiles, allowing experiments at the same relative depth k_0d but a different group length $\sigma = 1/(k_0\epsilon)$ to be overlaid. The measured vertical displacements again show far more scatter than their horizontal counterparts. The increased magnitude of the error wave at low k_0d is evident in the additional scatter in the experiments at shallower relative depth.

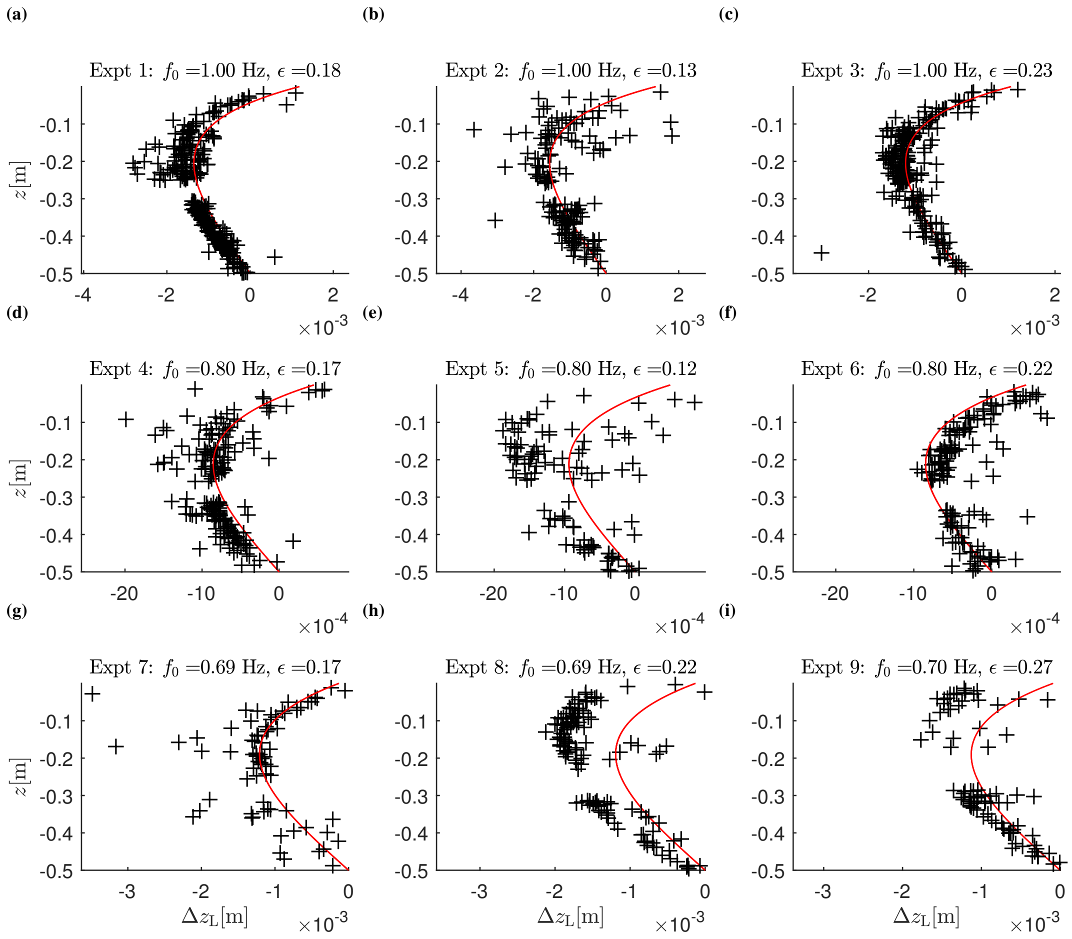

Figure 2.10: Profiles of vertical Lagrangian displacement between $t_1 = -3\sigma/c_{g,0}$ and $t_2 = 0$ (corresponding to the center of the packet $t = 0$) as a function of depth: postprocessed experimental data (black crosses) and theoretical predictions from (2.24) (continuous red lines).

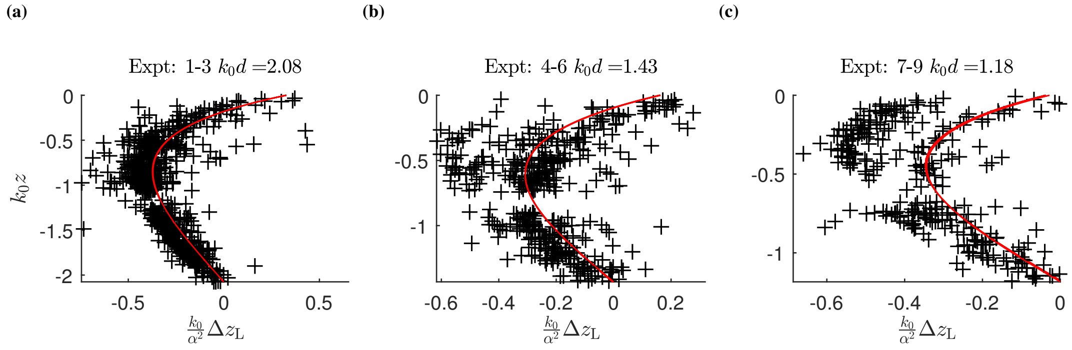

Figure 2.11: Scaled, nondimensional profiles of vertical Lagrangian displacement between $t_1 = -3\sigma/c_{g,0}$ and $t_2 = 0$ (corresponding to the center of the packet $t = 0$) as a function of depth: postprocessed experimental data (black crosses) and theoretical predictions from (2.24) (continuous red lines).

Chapter 3

Mechanism for the increased transport of large floating marine debris

Abstract

Periodic water waves generate Stokes drift as manifest from the orbits of Lagrangian particles not fully closing. Stokes drift can contribute to the transport of floating marine litter, including plastic. Previously, marine litter objects have been considered to be perfect Lagrangian tracers, thus travelling with the Stokes drift of the waves. However, floating marine litter objects have large ranges of sizes and densities, which potentially result in different rates of transport by the waves due to the non-Lagrangian behaviour of the objects. Through a combination of theory and experiments for idealised spherical objects in deep-water waves, we show that different objects are transported at different rates depending on their size and density and that larger buoyant objects can have increased drift compared with Lagrangian tracers. We show that the mechanism for the increased drift observed in our experiments comprises the variable submergence and the corresponding dynamic buoyancy force components in the direction perpendicular to the local water surface. This leads to an amplification of the drift of these objects compared to the Stokes drift when averaged over the wave cycle. Using an expansion in wave steepness, we derive a closed-form approximation for this increased drift, which can be included in ocean-scale models of marine litter transport.

3.1 Introduction

In the last half century large concentrations of plastic have polluted the oceans, with harmful effects on marine wildlife and potentially on human health [Ostle et al., 2019, Cózar et al., 2014, Cole et al., 2011]. Plastic pollution will have lasting impact because it is expected to take hundreds or thousands of years for plastic to decay in the ocean [Cole et al., 2011]. Floating plastic debris is transported and dispersed by three key mechanisms: currents, wind, and waves [van Sebille et al., 2020]. This paper will investigate wave-induced transport.

To leading order and in deep water, the Lagrangian motion induced by waves takes the form of circular orbits with Lagrangian particles following these orbits in a periodic fashion. The imbalance between the forward orbital velocity when under the crest and backward orbital velocity when under the trough, caused by the decay in velocity with depth, and the fact that particles spend more time under the forward-moving crest than under the backward-moving trough results in orbits that do not close, i.e. a Lagrangian-mean drift, known as Stokes drift [Stokes, 1847]. Stokes drift is proportional to the square of wave steepness and decays with depth at twice the rate of the oscillatory water particle velocity (see e.g. the review by van den Bremer and Breivik [2017]). Ocean surface gravity waves are driven by wind, and thus Stokes drift has often been assumed to be locally proportional to the wind forcing [Weber, 1983]. However, waves are slow to build and, once established as swell, waves can travel long distances with little dispersion [Ardhuin et al., 2019, Hanley et al., 2010] and so their magnitude is not always proportional to the local wind forcing. Wave models, such as WaveWatch III [The WAVEWATCH III ® Development Group, 2016], can be used to predict Stokes drift [Webb and Fox-Kemper, 2011, 2015].

Several authors have considered the effect of Stokes drift on the transport of floating marine litter. In an early study, Kubota [1994] found that Stokes drift derived from local wind fields did not make a significant contribution towards debris transport. However, more recent studies that included the entire wave field showed that Stokes drift could play an important role. For example, Iwasaki et al. [2017] found that Stokes drift transported plastic towards the coast in the Sea of Japan during winter, and Delandmeter and Van Sebille [2019] reported similar behaviour in the Norwegian Sea. Stokes drift could enable debris to leak out of the Indian Ocean [Dobler et al., 2019], cause drifting debris to cross the strong circumpolar winds and currents to reach the Antarctic coast [Fraser et al., 2018], and thus promote increased transport to polar regions [Onink et al., 2019]. Isobe et al. [2014] modelled the plastic beaching process by including Stokes drift and sinking velocity and observed that larger plastic debris was selectively moved onshore. All the foregoing studies have simply assumed that floating marine litter objects are transported with the Stokes drift; in other words, that they are perfect Lagrangian tracers.

If a particle is infinitesimally small and has the same density as water, it will behave purely as a Lagrangian tracer and will be transported with the Stokes drift. This is not necessarily true for an object of finite size or of a density different to that of water. As the inertia of such an object becomes important, the fluid will exert a drag on the object owing to the relative velocity between the object and fluid. Furthermore, the object may rise, sink, or float depending on the density difference. The literature distinguishes between fully submerged and floating objects, discussed separately below.

The motion of a fully submerged sphere in unsteady flow with viscous drag can be described by the Maxey–Riley equations [Maxey and Riley, 1983]. Based on this pioneering work, Eames [2008] and Santamaria et al. [2013] examined how far slightly positively or negatively buoyant objects would be transported by regular waves. They defined the distance transported as either the horizontal distance transported whilst a negatively buoyant object sinks from the free surface to the sea floor or the horizontal distance transported whilst a positively buoyant object rises from the sea floor to the free surface. Eames [2008] and Santamaria et al. [2013] both used expansions in Stokes number to arrive at analytical solutions for small objects. To leading order and for negatively buoyant objects, Eames [2008] showed such small objects are transported with a mean horizontal Stokes drift velocity and sediment with their terminal fall velocity. Santamaria et al. [2013] predicted that positively buoyant objects would experience an increase in drift owing to their inertia. Although Eames [2008] and Santamaria et al. [2013] considered the object's inertia when examining transport by waves, both considered completely submerged objects.

Also considering fully submerged objects, DiBenedetto and Ouellette [2018b] first showed non-spherical objects have a preferential orientation under waves, confirming this result numerically [DiBenedetto and Ouellette, 2018b] and experimentally [DiBenedetto et al., 2019] but not examining the effect of the object's inertia. The orientation changes the drag on the slightly negatively buoyant objects, which results in objects of different shapes being transported different distances before 'raining out' [DiBenedetto et al., 2018].

Analysis of the motion of floating objects commences with the extension of Maxey–Riley equation [Maxey and Riley, 1983] to include a free surface as undertaken by Rumer et al. [1979]. These authors considered the free surface to be an oscillating slope with a vertical force balance between gravity and buoyancy, whilst the horizontal part of the buoyancy force induces object motion in what Rumer et al. [1979] termed the slope-sliding effect. Shen and Zhong [2001] further extended the slope-sliding model, proceeding to find analytical solutions of the object motion in limit of no added mass or no resistance. Huang et al. [2016] found that the drift of relatively large floating discs, used to model floating ice sheets, increased beyond the Stokes drift in physical experiments. This could be explained by numerical solutions to an equation of motion based on a rotating coordinate system which aligned with the free surface, leaving the physical mechanism at work unclear.

This theoretical and experimental paper examines the transport of inertial, finite-size floating marine litter under the influence of non-breaking waves. Our derivation starts from Newton's second law, with buoyancy, gravity and drag force components. Using a transformed coordinate system, similar but not equivalent to Huang et al. [2016], that vertically translates and is oriented orthogonally to the time-varying free surface, we ensure that the dynamic buoyancy term is directed normal to the free surface. In this model, the drag force changes with submergence of the object, and we formulate a drag coefficient that is valid across a range of Reynolds numbers. We use perturbation methods to derive a closed-form solution for the transport of inertial, finite-size floating spherical objects, which is then used to interpret the physical mechanism for their enhanced transport compared to the Stokes drift. Numerical and analytical solutions are compared for viscous drag. To validate the model, we perform experiments in a laboratory wave flume.

This paper is laid out as follows. Section 3.2 presents the theoretical model. Section 3.3 describes solutions obtained using perturbation methods for visous drag. Section 3.4 compares the analytical solutions thus obtained against numerical solutions of the model. The numerical solutions are also used to compare the model's predictions for viscous and non-viscous drag. Section 3.5 describes the laboratory flume experiments, and section 3.6 compares the experimental results with theoretical predictions. Conclusions are drawn in section 3.7.

3.2 Mathematical model

3.2.1 Equation of motion of a floating object

The motion of a floating inertial object is described by Newton's second law:

$$m\dot{\mathbf{v}} = \mathbf{F} \equiv \mathbf{B} + \mathbf{M} + \mathbf{G} + \mathbf{R}, \tag{3.1}$$

where m is the mass of the object and $\mathbf{v}$ its velocity with the dot denoting a derivative with respect to time. The total force on the object $\mathbf{F}$ can be decomposed into a buoyancy force $\mathbf{B}$, an added-mass force $\mathbf{M}$, a gravity force $\mathbf{G}$ and a resistance force $\mathbf{R}$, which are formulated below. The buoyancy and added-mass forces arise from the integral of pressure around the object. For simplicity, we will assume the object is spherical with diameter D. Throughout, it is assumed that the object is small relative to the wavelength, such that $D/\lambda_0 \ll 1$, with D the diameter of the object and λ_0 the wavelength. This has four important consequences. First, the wave field is unaffected by the presence of the object; in other words, there is no diffraction. Second, the free surface can be approximated as an (inclined) straight line on the scale of the object. Third, we can approximate the (relative) velocity field between the liquid and object, which determines the drag on the object, as the velocity at a point. Fourth, the buoyancy force can be computed from the submergence measured relative to the free surface.

We first adopt a stationary two-dimensional laboratory coordinate system $(x,\ z)$ with the vertical coordinate z measured upwards from the undisturbed free surface. To define the forces on the object, a second, moving coordinate system $(\tau,\ n)$ is established that moves vertically with the free surface $z = \eta(x,t)$ and aligns locally with the τ-axis tangential to the free surface at the position of the object x_p and the n-axis normal to it, as shown in figure 3.1. The coordinate transformation takes the form of a vertical translation followed

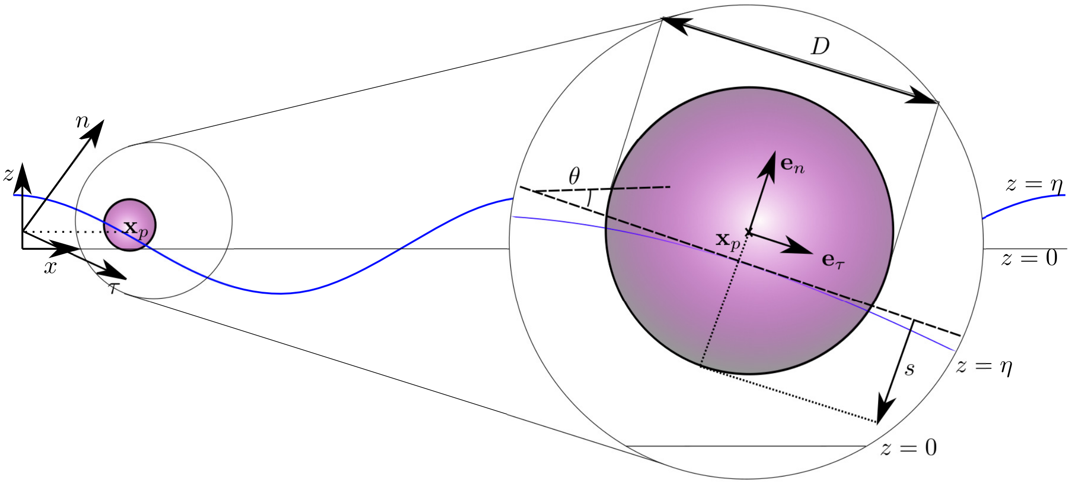

Figure 3.1: Diagram of the two coordinate systems used to describe a floating object of diameter D: a stationary laboratory coordinate system (x, z) and a vertically translating and rotating coordinate system (τ, n) with its origin at the vertical position of the free surface $z = \eta_p$ and the τ-axis aligned tangential to the free surface. The vector $\mathbf{x}_p$ locates the centre of the object relative to the origin of the stationary coordinate system, $\tan\theta = \partial\eta/\partial x$ is the slope of the free surface, and s is the (variable) submergence.

by a clockwise rotation through the angle $\theta = \arctan(\partial\eta/\partial x)$, both at the horizontal position of the object x_p:

$$\begin{bmatrix} \tau \\ n \end{bmatrix} = \begin{bmatrix} 1 & \partial_x\eta(x,t)|_{x_p} \\ -\partial_x\eta(x,t)|_{x_p} & 1 \end{bmatrix} \begin{bmatrix} x \\ z - \eta(x_p,t) \end{bmatrix} \Xi(x_p,t)$$
$$\text{with} \quad \Xi(x_p,t) \equiv \Big(1 + \big(\partial_x\eta(x,t)|_{x_p}\big)^2\Big)^{-1/2}. \quad (3.2)$$

The quantities $\partial_x\eta(x,t)$, $\eta(x,t)$ and $\Xi(x,t)$ are evaluated at the object position $x_p(t)$ and are thus solely functions of time t. The coordinate system (τ, n) does not translate in the horizontal direction, enabling direct estimation of the object's horizontal drift $\overline{v}_x = \overline{\dot{x}}_p$, where the overbar denotes an average over the wave cycle. The time-dependent unit normal vectors are

$$\mathbf{e}_\tau = \big[1, \partial_x\eta(x,t)|_{x_p}\big]\,\Xi(x_p,t) \quad \text{and} \quad \mathbf{e}_n = \big[-\partial_x\eta(x,t)|_{x_p}, 1\big]\,\Xi(x_p,t). \quad (3.3\text{a,b})$$

It should be emphasized that (τ, n) is an accelerating coordinate system, both in terms of rotation and vertical translation. Inverting (3.3):

$$\begin{aligned}\mathbf{e}_x &= \big(\mathbf{e}_\tau(t) - \partial_x\eta(x,t)|_{x_p}\mathbf{e}_n(t)\big)\,\Xi(x_p,t) \quad \text{and}\\ \mathbf{e}_z &= \big(\partial_x\eta(x,t)|_{x_p}\mathbf{e}_\tau(t) + \mathbf{e}_n(t)\big)\,\Xi(x_p,t).\end{aligned} \tag{3.4a,b}$$

For the time-dependent unit normal vectors $\mathbf{e}_\tau(t)$ and $\mathbf{e}_n(t)$:

$$\frac{\mathrm{d}\mathbf{e}_\tau(t)}{\mathrm{d}t} = \dot\theta_p\mathbf{e}_n(t) \text{ and } \frac{\mathrm{d}\mathbf{e}_n(t)}{\mathrm{d}t} = -\dot\theta_p\mathbf{e}_\tau(t) \text{ with } \dot\theta_p = \mathrm{d}_t(\partial_x\eta(x,t)|_{x_p})\Xi_p^2, \tag{3.5a,b}$$

in which $\theta_p(t) \equiv \theta(x_p(t),t)$, $\Xi_p(t) = \Xi(x_p(t),t)$, and $\mathrm{d}_t \equiv \mathrm{d}/\mathrm{d}t$.

Denoting the position of the object as $\mathbf{x}_p = x_p\mathbf{e}_x + z_p\mathbf{e}_z = \eta_p\mathbf{e}_z + \tau_p\mathbf{e}_\tau + n_p\mathbf{e}_n$ with $\eta_p(t) \equiv \eta(x_p(t),t)$, its velocity may be written as:

$$\mathbf{v} = v_x\mathbf{e}_x + v_z\mathbf{e}_z = \left(\dot\tau_p - \dot\theta_p n_p + \dot\eta_p\partial_x\eta|_{x_p}\Xi_p\right)\mathbf{e}_\tau + \left(\dot n_p + \dot\theta_p\tau_p + \dot\eta_p\Xi_p\right)\mathbf{e}_n, \tag{3.6}$$

where we have used (3.5) for the time derivatives of the unit vectors $\mathbf{e}_\tau$, and $\mathbf{e}_n$, and $\mathbf{e}_z$ was substituted for from (3.4b). The velocity in the translating reference frame $\mathbf{v}^*$ is related to the velocity in the stationary reference frame $\mathbf{v}$ by $\mathbf{v}^* = \mathbf{v} - \dot\eta_p\mathbf{e}_z$, where both vectors can be expressed in any arbitrary set of orthogonal components, such as $\mathbf{e}_x$ and $\mathbf{e}_z$ or $\mathbf{e}_\tau$ and $\mathbf{e}_n$. Accordingly, the acceleration of the object can be written as:

$$\begin{aligned}\dot{\mathbf{v}} = \dot v_x\mathbf{e}_x + \dot v_z\mathbf{e}_z &= \left(\ddot\tau_p - \ddot\theta_p n_p - 2\dot\theta_p\dot n_p - (\dot\theta_p)^2\tau_p + \ddot\eta_p\partial_x\eta|_{x_p}\Xi_p\right)\mathbf{e}_\tau\\ &+ \left(\ddot n_p + \ddot\theta_p\tau_p + 2\dot\theta_p\dot\tau_p - (\dot\theta_p)^2 n_p + \ddot\eta_p\Xi_p\right)\mathbf{e}_n.\end{aligned} \tag{3.7}$$

To evaluate (3.7), the double time derivatives $\ddot\theta_p$ and $\ddot\eta_p$ must be evaluated explicitly. The double time derivative $\ddot\theta_p$ can be obtained by differentiating with respect to time twice using the relationship $\theta_p = \arctan\left(\partial\eta/\partial x|_{x_p}\right)$, noting that x_p is a function of time requiring the chain rule, to obtain:

$$\begin{aligned}\ddot\theta_p = &\left(\partial_{ttx}\eta|_{x_p} + 2\dot x_p\partial_{txx}\eta|_{x_p} + (\dot x_p)^2\,\partial_{xxx}\eta|_{x_p} + \ddot x_p\partial_{xx}\eta|_{x_p}\right)\Xi_p^2\\ &+ \left(\partial_{tx}\eta|_{x_p} + \dot x_p\partial_{xx}\eta|_{x_p}\right)2\Xi_p\dot\Xi_p.\end{aligned} \tag{3.8}$$

Similarly, the double time derivative $\ddot\eta_p$ takes into account the dependence of the free surface $\eta_p(x_p(t),t)$ on time t and the time-dependent horizontal position

$x_p(t)$, which gives through the chain rule after differentiating twice:

$$\ddot{\eta}_p = \partial_{tt}\eta|_{x_p} + 2\dot{x}_p\partial_{tx}\eta|_{x_p} + (\dot{x}_p)^2\,\partial_{xx}\eta|_{x_p} + \ddot{x}_p\partial_x\eta|_{x_p}. \tag{3.9}$$

Substituting (3.8) and (3.9) into (3.7) and thence into (3.1) results in two second-order differential equations in the (n,τ) coordinate system, which are explicitly given by (3.45) and (3.46) in section 3.A. These two equations contain three second-order time derivatives, and so a third (kinematic) equation relating the second-order derivatives is required to solve the system. Such an equation can for example be found by taking the dot product of (3.7) and $\mathbf{e}_x$ (see (3.47) in section 3.A).

For convenience, we express the normal coordinate of the centre of the object n_p in terms of the submergence depth s (see figure 3.1). To do so, we assume that $D/\lambda_0 \ll 1$ so that the free surface is a locally straight line with n-coordinate $n_s = -\partial_x\eta|_{x_p}x_p\Xi_p$ (using (3.2), setting $x = x_p$ and $z = \eta_p$). The submergence depth is then given by $s = D/2-(n_p-n_s) = D/2-n_p-x_p\partial_x\eta|_{x_p}\Xi_p$, where D is the diameter of the object. From (3.6), the following expression is obtained for the horizontal velocity of the object:

$$\dot{x}_p = \left(\dot{\tau}_p - \dot{\theta}_p\left(n_p + \tau_p\partial_x\eta|_{x_p}\right) - \dot{n}_p\partial_x\eta|_{x_p}\right)\Xi_p. \tag{3.10}$$

It should be noted that $\dot{s} = -\dot{n}_p - \mathrm{d}_t(x_p\partial_x\eta|_{x_p}\Xi_p)$.

Buoyancy and added mass

We decompose total pressure p into an undisturbed component $p_{\text{undisturbed}}$ and a disturbed component $p_{\text{disturbed}}$ owing to the presence of the object. Assuming an object that is small relative to the wavelength ($D/\lambda_0 \ll 1$), the undisturbed pressure varies as $p_{\text{undisturbed}} = \rho_f g(\eta(x,t)-z)$ on the scale of the object with ρ_f the density of the fluid, so that the dynamic free surface boundary condition $p_{\text{undisturbed}}(z=\eta) = 0$ is satisfied, the variation with depth is hydrostatic, and any depth-dependent variation owing the waves (cf. $\exp(k_0 z)$ with k_0 the wavenumber) is ignored.

The undisturbed pressure integrated around the wetted surface results in a buoyancy force acting in the normal direction to the free surface,

$$B_n(t) = \frac{gm}{\beta}\frac{V_\mathrm{s}}{V}\Xi_p^{-1} = \frac{gm}{\beta}\left(3\left(\frac{s(t)}{D}\right)^2 - 2\left(\frac{s(t)}{D}\right)^3\right)\Xi_p^{-1}, \tag{3.11}$$

where g is the gravitational constant, V_s is the submerged and V the total volume of the sphere, and $\beta \equiv \rho_o/\rho_f$ is the ratio of object to fluid density. By including $\rho_f g\eta(x,t)$ in the undisturbed pressure, we have included the Froude–Krylov force resulting from the waves.

The disturbed component of pressure leads to an added mass term, as derived by Maxey and Riley [1983]:

$$\mathbf{M}_\tau = \frac{C_m(\beta)m}{\beta}(\dot{u}_\tau(\tilde{\mathbf{x}}_p, t) - \dot{v}_\tau) \text{ and } \mathbf{M}_n = \frac{C_m(\beta)m}{\beta}(\dot{u}_n(\tilde{\mathbf{x}}_p, t) - \dot{v}_n), \tag{3.12a,b}$$

where the added mass coefficient C_m is a function of the object's submergence and thus its density ratio. In a potential flow a fully submerged sphere has an added mass coefficient of 1/2. Instead of deriving the complicated dependence of C_m on the object's density, we interpolate linearly between a sphere that is fully submerged ($\beta = 1$, $C_m = 1/2$) and a sphere that is entirely out of the water ($\beta = 0$, $C_m = 0$) and set $C_m = \beta/2$. The small-diameter assumption leaves the vertical location, where we should evaluate the velocity of the surrounding fluid in (3.12), unspecified. We set this location to be at the free surface, $\tilde{\mathbf{x}}_p = (x_p, \eta_p)$.

Gravity forces

The gravity force acts in the vertical direction, and has the following components in the moving coordinate system,

$$G_\tau(t) = -mg\partial_x\eta|_{x_p}\Xi_p(t) \text{ and } G_n(t) = -mg\Xi_p(t). \tag{3.13a,b}$$

Resistance forces

The resistance terms are caused by drag on the object when it has a velocity relative to that of the surrounding liquid. The drag depends on the submer-

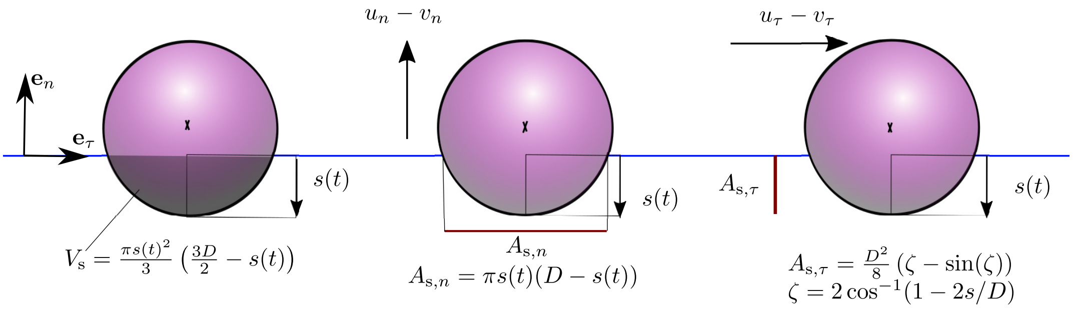

Figure 3.2: Diagrams of (left) the submerged volume V_{s} as a function of the variable submergence $s(t)$; (centre) the projected area of a submerged sphere moving in the normal direction ($\mathbf{e}_n$); and (right) the projected area of a submerged sphere moving in the tangential direction ($\mathbf{e}_\tau$). All diagrams are shown in the (τ, n) coordinate system.

gence of the object and is taken into account by using the submerged projected area of a sphere in the tangential and normal directions (see figure 3.2). The resistance force in the tangential direction is,

$$R_\tau(t) = \frac{1}{2} C_{d,\tau}\left(\mathrm{Re}_\tau\right) \rho_f A_{\mathrm{s},\tau} \left|u_\tau^*(\tilde{\mathbf{x}}_p, t) - v_\tau^*(t)\right| \left(u_\tau^*(\tilde{\mathbf{x}}_p, t) - v_\tau^*(t)\right), \quad (3.14)$$

where $C_{d,\tau}$ is the drag coefficient for the τ-direction dependent on the Reynolds number Re_τ, and u_τ^* is the Eulerian velocity component of the surrounding fluid in the τ-direction in the moving reference frame, then As for the added mass, we evaluate the velocity at the free surface, $\tilde{\mathbf{x}}_p = (x_p, \eta_p)$. The drag force is a function of the difference in object velocity and the Eulerian fluid velocity following the object, if the Lagrangian fluid velocity is used instead, then the drift in the limit of small object size does not recover Stokes drift. The submerged projected area of a sphere in the tangential direction is given by (see fig. 3.2):

$$A_{\mathrm{s},\tau} = \frac{D^2}{8}\left(\zeta - \sin(\zeta)\right) \quad \text{with} \quad \zeta \equiv 2\cos^{-1}\left(1 - 2s/D\right). \quad (3.15)$$

Similarly, we have for the n-direction,

$$R_n(t) = \frac{1}{2} C_{d,n}\left(\mathrm{Re}_n\right) \rho_f A_{\mathrm{s},n} \left|u_n^*(\tilde{\mathbf{x}}_p, t) - v_n^*(t)\right| \left(u_n^*(\tilde{\mathbf{x}}_p, t) - v_n^*(t)\right), \quad (3.16)$$

where we have evaluated the velocity of the surrounding fluid at the same location $\tilde{\mathbf{x}}_p$ as for the tangential resistance force. The submerged projected

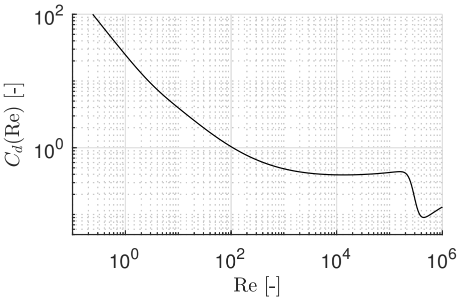

Figure 3.3: The drag coefficient of a sphere (3.18) at the range of Reynolds numbers for which it is valid [Morrison, 2013]. The drag coefficient has been established by fitting to experimental data and recovers the limit of 24/Re for small Reynolds numbers.

area of a sphere in the normal direction is given by (see figure 3.2):

$$A_{\mathrm{s},n} = \pi s(t)\left(D - s(t)\right). \tag{3.17}$$

We choose a formulation of the drag coefficient $C_d(\mathrm{Re})$ that captures both viscous drag for small Reynolds number, which is linear in the velocity difference, and quadratic drag at high Reynolds number. Specifically, we use the fit to experimental data for drag on a sphere by Morrison [2013, page 625], which is accurate for $\mathrm{Re} < 1 \times 10^6$:

$$\begin{aligned} C_d(\mathrm{Re}) = \frac{24}{\mathrm{Re}} + 2.6\frac{\mathrm{Re}/5}{(1+\mathrm{Re}/5)^{1.52}} + 0.411\frac{(\mathrm{Re}/(2.63 \times 10^5))^{-7.94}}{(1+\mathrm{Re}/(2.63\times 10^5))^{-8}} \\ + 0.25\frac{\mathrm{Re}/(1\times 10^6)}{1+\mathrm{Re}/(1\times 10^6)}, \end{aligned} \tag{3.18}$$

Which is explicitly shown in fig. 3.3. We independently evaluate (3.18) for the two orthogonal directions, i.e. $\mathrm{Re}_\tau \equiv |u_\tau - v_\tau|D/\nu$ and $\mathrm{Re}_n \equiv |u_n - v_n|D/\nu$ with ν the kinematic viscosity of the fluid.

Taking the small-object and thus the small-Reynolds-number limit of the tangential drag force in (3.14) and the normal drag in (3.16), we can recover the Stokes drag on a partially submerged sphere as:

$$R_\tau = 3\pi\rho_f \nu D \hat{A}_{\mathrm{s},\tau}\left(u_\tau - v_\tau\right) \quad \text{and} \quad R_n = 3\pi\rho_f \nu D \hat{A}_{\mathrm{s},n}\left(u_n - v_n\right), \tag{3.19a,b}$$

where $\hat{A}_{\mathrm{s},\tau} \equiv A_{\mathrm{s},\tau}/(\pi D^2/4)$ and $\hat{A}_{\mathrm{s},n} \equiv A_{\mathrm{s},n}/(\pi D^2/4)$ are the submerged projected areas of a partially submerged sphere normalised by the projected area of a fully submerged sphere in tangential and normal directions, respectively.

3.2.2 Fluid velocity for surface gravity waves

We consider unidirectional deep-water surface gravity waves propagating over a horizontal bed in the (x, z)-coordinate system, with z measured vertically upwards from the still water level, and the free surface located at $z = \eta$. For irrotational flow of inviscid, incompressible fluid, the governing (Laplace) equation is,

$$\nabla^2\phi = 0 \quad \text{for} \quad -d \leq z \leq \eta, \tag{3.20}$$

where ϕ is the velocity potential and d depth. Equation (3.20) is solved subject to the no-flow bottom boundary condition,

$$\partial_z\phi = 0 \quad \text{for} \quad z = -d, \tag{3.21}$$

and the kinematic and dynamic linear free surface boundary conditions,

$$u_z - \partial_t\eta - u\partial_x\eta = 0 \quad \text{and} \quad g\eta + \partial_t\phi + \frac{1}{2}(\nabla\phi)^2 = 0 \quad \text{at} \quad z = \eta, \tag{3.22a,b}$$

where the velocity components are $u_x = \partial_x\phi$ and $u_z = \partial_z\phi$.

3.3 Perturbation theory for viscous drag

To interpret the physical mechanism behind the drift predicted by the model derived in §3.2, we use perturbation theory to establish an analytical solution. We do so here for the case of viscous drag, as this allows inclusion of drag at first order in our expansion. The case of viscous drag corresponds to the small-object limit of the drag force with general drag coefficient (3.18). We will discuss limitations of viscous drag in §3.3.4 and consider numerical solutions of our model in §3.4 in which the assumption of viscous drag is relaxed. We consider only periodic, weakly nonlinear, deep-water surface gravity waves, so that $k_0 d \gg 1$ with k_0 the wavenumber. We perturb the object position $\mathbf{x}_p$ in a Stokes-type expansion in wave steepness ($\alpha = k_0 a_0$, where a_0 the wave amplitude), giving

$$\mathbf{x}_p(t) = \mathbf{x}_p^{(0)} + \mathbf{x}_p^{(1)}(t)\Big|_{\mathbf{x}_p^{(0)}} + \mathbf{x}_p^{(2)}(t)\Big|_{\mathbf{x}_p^{(0)}} + \mathcal{O}(\alpha^3). \tag{3.23}$$

where the superscript corresponds to the order in α, and $\mathbf{x}_p^{(0)}$ is the object label and thus not a function of time. As we are interested in the wave-induced drift, which arises at second order, we only pursue those terms necessary to obtain this drift.

Applying a perturbation expansion in the same small parameter α to the governing equation of the fluid (3.20) and its boundary conditions (3.21) and (3.22) allows the free surface η and the velocity potential ϕ to be determined, and we do so up to second order.

Although the perturbation theory solutions in this section are for regular waves, the experiments introduced in section 3.5 make use of long (or narrow-bandwidth) wavepackets for practical reasons. We assume that inertial effects do not arise on the scale of the packets, as justified in section 3.B, so that we can correct for the presence of a wavepacket simply by accounting for its Eulerian mean flow. Table 3.1 lists the resulting solutions, whose derivation and laboratory validation is given in more detail by Van Den Bremer et al. [2019] for deep water and Calvert et al. [2019] for intermediate depth. We consider only deep-water waves here ($k_0 d \gg 1$). The solutions for the Eulerian return flow and the second-order surface elevation are based on wavepackets with envelope $|A_0|$. The solution assumes the wavepackets are narrow banded and that the Eulerian return flow is shallow, which corresponds to a depth that is small relative to the packet length (Calvert et al. [2019] establish the Eulerian return flow without the shallow return flow assumption). In practise, including the effect of the return flow only leads to a small correction of less than 2% for our laboratory experiments.

3.3.1 Zeroth-order in wave steepness: $\mathcal{O}(\alpha^0)$

At zeroth-order in wave steepness, wave forcing evidently does not play a role. Only the normal direction of (3.1) has any forcing at zeroth order, where the following leading-order static balance is achieved between buoyancy force and

Field	Symbol	Solution
First-order horizontal velocity	$u_x^{(1)}$	$A_0\omega_0\exp(i\varphi + k_0 z)$
First-order vertical velocity	$u_z^{(1)}$	$-A_0\omega_0 i\exp(i\varphi + k_0 z)$
First-order free surface elevation	$\eta^{(1)}$	$A_0\exp(i\varphi)$
Second-order horizontal Eulerian velocity	$u_x^{(2)}$	$-\frac{\omega_0}{2d}\lvert A_0\rvert^2$
corresponding time-integrated displacement	$\Delta x_E^{(2)}$	$-\frac{\omega_0}{2d}\int_{t_1}^{t_2}\lvert A_0\rvert^2 \mathrm{d}t$
Second-order horizontal Stokes drift velocity	$u_S^{(2)}$	$k_0\omega_0\lvert A_0\rvert^2\exp(2k_0 z)$
corresponding time-integrated displacement	$\Delta x_S^{(2)}$	$k_0\omega_0\int_{t_1}^{t_2}\lvert A_0\rvert^2 \mathrm{d}t$

Table 3.1: First and second-order solutions for the kinematic properties of deep-water surface gravity waves, with $A_0 = a_0\hat{A}_0$ the wave amplitude envelope, a_0 its amplitude, $\hat{A}_0$ a non-dimensional envelope, ω_0 the carrier wave frequency, and k_0 the carrier wavenumber. Where complex fields are given, the real part is understood, and $\varphi = k_0 x - \omega_0 t$. The first three rows are first-order solutions, valid for regular waves or wavepackets. The remaining rows comprise second-order solutions for the wave-averaged Eulerian and Stokes velocities and the set-down. The second-order wave-averaged Eulerian velocity only arises for wavepackets, which are considered in the experiments only.

gravity,

$$F_n^{(0)} = \frac{gm}{\beta}\left[3\left(\frac{s^{(0)}}{D}\right)^2 - 2\left(\frac{s^{(0)}}{D}\right)^3\right] - gm = 0. \tag{3.24}$$

We have used the fact that $\Xi_p = 1$ at zeroth order and note that (3.24) is only valid for a floating sphere, i.e. $|D/2 - s^{(0)}| \leq D/2$. Equation (3.24) is a (cubic) implicit equation, which can be readily solved numerically for the depth of submergence of a floating sphere in the absence of waves $s^{(0)}$.

3.3.2 First-order in wave steepness: $\mathcal{O}(\alpha^1)$

We begin by expressing the projected areas of the sphere required to calculate the tangential and normal resistance forces as series expansions around $s^{(0)}$. The submerged projected area of a sphere in the tangential direction (3.15) can be approximated by

$$A_{\mathrm{s},\tau}(s) = A_{\mathrm{s},\tau}(s^{(0)}) + 2D\sqrt{\frac{s^{(0)}}{D} - \left(\frac{s^{(0)}}{D}\right)^2}\, s^{(1)} + \mathcal{O}(\alpha^2), \tag{3.25}$$

where we have obtained $\partial_s(A_{\mathrm{s},\tau})$ from (3.15) by implicit differentiation. For the submerged projected area of a sphere in the normal direction, it is sufficient for our purposes to evaluate $A_{\mathrm{s},n}(s)$ at zeroth order, i.e. $A_{\mathrm{s},n}(s) = A_{\mathrm{s},n}(s^{(0)}) + \mathcal{O}(\alpha^1)$.

The tangential direction

To first-order of approximation, the velocity and acceleration in the horizontal coordinate x and the tangential coordinate τ are equal, i.e. $\dot{x}_p^{(1)} = v_x^{(1)} = v_\tau^{(1)}$ and $\ddot{x}_p^{(1)} = \dot{v}_x^{(1)} = \dot{v}_\tau^{(1)}$. The only forces that play a role are the tangential components of the added mass, gravity and the resistance force. The first-order added-mass terms in the tangential direction are

$$M_\tau^{(1)} = \frac{C_m m}{\beta}(\dot{u}_x^{(1)} - \ddot{x}_p^{(1)}). \tag{3.26}$$

The resistance force (3.19a) can be approximated as:

$$R_\tau^{(1)} = \Gamma_R m\omega_0 \hat{A}_{\mathrm{s},\tau}^{(0)}(u_x^{(1)}|_{\tilde{\mathbf{x}}_p^{(0)}} - \dot{x}_p^{(1)}) \quad \text{with} \quad \Gamma_R \equiv \frac{3\pi\nu D}{\beta V\omega_0}, \tag{3.27}$$

where the non-dimensional coefficient Γ_R measures the importance of the resistance force.

From the object's equation of motion (3.1) we thus obtain:

$$\left(1 + \frac{C_m}{\beta}\right)\ddot{x}_p^{(1)} = \frac{C_m}{\beta}\dot{u}_x^{(1)}|_{\tilde{x}_p^{(0)}} - g\partial_x\eta^{(1)}|_{x_p^{(0)}} + \Gamma_R\hat{A}_{\mathrm{s},\tau}^{(0)}\omega_0\left(u_x^{(1)}|_{\tilde{\mathbf{x}}_p^{(0)}} - \dot{x}_p^{(1)}\right). \tag{3.28}$$

We seek a solution to the forced second-order ordinary differential equation (3.28) of the form $x_p^{(1)} = \mathcal{R}(iX^{(1)}a_0\exp(i\varphi_p^{(0)}))$ with $\varphi_p^{(0)} = k_0x_p^{(0)} - \omega_0t + \varphi_0$ and $\varphi_0 = \arg(A_0)$, ignoring initial transients. The complex coefficient $X^{(1)}$ represents the amplitude and phase change of the horizontal motion of the object relative to that of an idealized Lagrangian object under the influence of waves at the same order, $x_L^{(1)} = \mathcal{R}(ia_0\exp(i\varphi_p^{(0)}))$. We obtain $X^{(1)} = 1$, i.e. there is no horizontal motion amplification compared to that of a Lagrangian particle.

The normal direction

Expressing the submergence depth s in terms of the vertical coordinate z_p, we have without approximation that $s = D/2 - (z_p - \eta_p)\Xi_p$. Therefore, the velocity and acceleration in the vertical coordinate z and the normal coordinate n are related to first order by:

$$\dot{z}_p^{(1)} = v_z^{(1)} = -\dot{s}^{(1)} + \dot{\eta}_p^{(1)} \quad \text{and} \quad \ddot{z}_p^{(1)} = \dot{v}_z^{(1)} = -\ddot{s}^{(1)} + \ddot{\eta}_p^{(1)}. \tag{3.29a,b}$$

We first approximate the buoyancy force (3.11) by:

$$B_n^{(1)} = \Gamma_B m \omega_0^2 s^{(1)} \quad \text{with} \quad \Gamma_B \equiv \frac{6}{\beta k_0 D} \left(\frac{s^{(0)}}{D} - \left(\frac{s^{(0)}}{D} \right)^2 \right), \tag{3.30}$$

the added-mass terms by,

$$M_n^{(1)} = \frac{C_m m}{\beta} \ddot{s}^{(1)}, \tag{3.31}$$

and the resistance force (3.19b) by:

$$R_n^{(1)} = \Gamma_R m \omega_0 \hat{A}_{\mathrm{s},n}^{(0)} \dot{s}^{(1)}, \tag{3.32}$$

where we have used $u_z^{(1)}(z=0) = \dot{\eta}_p^{(1)}$ from the linearised kinematic free surface boundary condition and $v_n^{(1)} = \dot{z}_p^{(1)}$. The new non-dimensional coefficient Γ_B measures the strength of dynamic buoyancy, and Γ_R measures the strength of the resistance force, as for the tangential resistance force in (3.27). From the object's equation of motion (3.1) we thus obtain:

$$\left(1 + \frac{C_m}{\beta}\right) \left(\ddot{\eta}_p^{(1)} - \ddot{s}^{(1)}\right) = \frac{C_m}{\beta} \dot{u}_z^{(1)}|_{\tilde{x}_p^{(0)}} + \Gamma_B \omega_0^2 s^{(1)} + \Gamma_R \hat{A}_{\mathrm{s},n}^{(0)} \omega_0 \dot{s}^{(1)}, \tag{3.33}$$

where we note gravity only enters at zeroth order. As for the tangential direction, we seek a solution to the forced second-order ordinary differential equation (3.33) of the form $s^{(1)} = \mathcal{R}(\mathcal{S}^{(1)} a_0 \exp(i\varphi_p^{(0)}))$ with $\varphi_p^{(0)} = k_0 x_p^{(0)} - \omega_0 t + \varphi_0$ and $\varphi_0 = \arg(A_0)$, ignoring initial transients. We find for the non-dimensional submergence at first order $\mathcal{S}^{(1)}$:

$$\mathcal{S}^{(1)} = \frac{1 + \dfrac{C_m}{\beta} - \Gamma_B - i\Gamma_R \hat{A}_{\mathrm{s},n}^{(0)}}{\left(1 + \dfrac{C_m}{\beta} - \Gamma_B\right)^2 + \left(\Gamma_R \hat{A}_{\mathrm{s},n}^{(0)}\right)^2}. \tag{3.34}$$

Figures 3.4 and 3.5 respectively show the magnitudes and arguments of the first-order solutions for the horizontal motion amplification $X^{(1)}$ and the variable submergence $\mathcal{S}^{(1)}$. In these figures, the purely Lagrangian limit, in

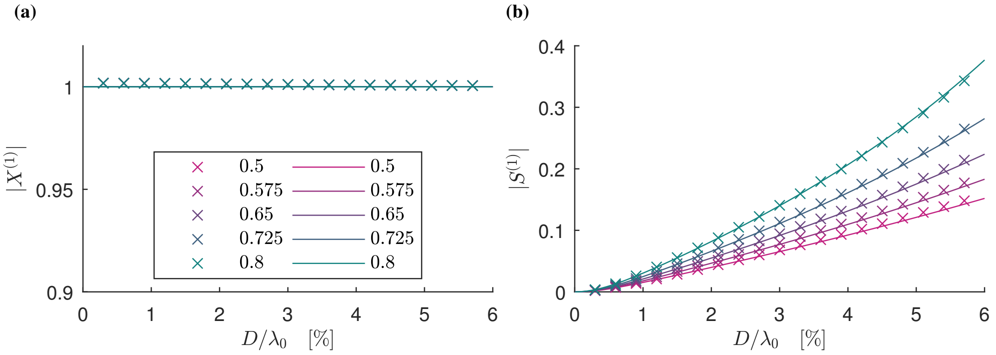

Figure 3.4: For viscous drag, magnitudes of the first-order horizontal motion amplification $X^{(1)}$ (a) and the variable submergence $\mathcal{S}^{(1)}$ (b) as functions of dimensionless object size D/λ_0 for different density ratios $\beta = \rho_o/\rho_f$, where the density ratio for each colour is shown in the legend. We have set $C_m = \beta/2$. Numerical and analytical solutions from perturbation theory are denoted by crosses and solid lines, respectively.

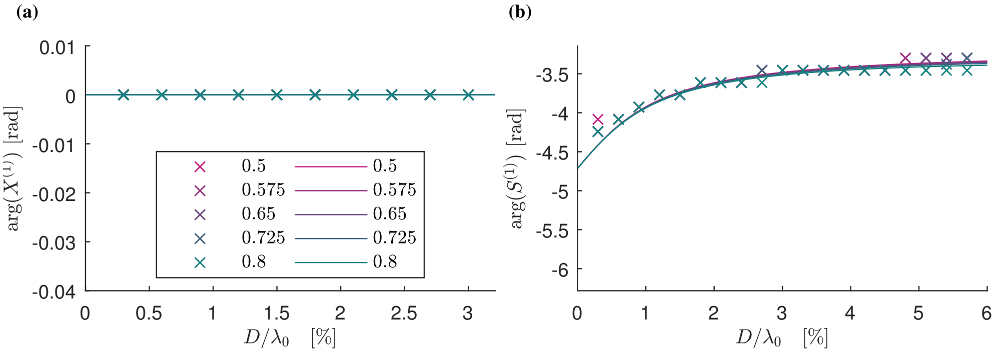

Figure 3.5: For viscous drag, arguments of the first-order horizontal motion amplification $X^{(1)}$ (a) and the variable submergence $\mathcal{S}^{(1)}$ (b) as functions of dimensionless object size D/λ_0 for viscous drag and for different density ratios $\beta = \rho_o/\rho_f$, as shown in the legend. We have set $C_m = \beta/2$. Numerical and analytical solutions from perturbation theory are denoted by crosses and solid lines, respectively.

which the object is simply transported with the Stokes drift and floats on the moving surface, corresponds to $X^{(1)} = 1$, $\mathcal{S}^{(1)} = 0$. This limit is obtained as object size tends to zero. Note that the phase of variable submergence in this limit is non-zero, $\arg(\mathcal{S}^{(1)} \to -3\pi/2)$. This is because both imaginary and real parts of the variable submergence tend to zero, with the imaginary part approaching zero at a faster rate. Note that the phase is in the third quadrant because both the real and imaginary parts of $S^{(1)}$ are negative, evident in (3.34) for the imaginary part whilst the relative size of Γ_b and $1+C_m/\beta$ causes the real part to be negative also. As our model is only valid for objects that are small relative to the wave length, we truncate the x-axis at $D/\lambda_0 = 6\%$. Diffraction of the wave field typically only becomes important for $D/\lambda_0 > 20\%$.

As confirmed in figure 3.4a, the magnitude of the horizontal motion $|X^1|$ is equivalent to that of a purely Lagrangian tracer. Turning to figure 3.5a, the argument of the horizontal motion $\arg(X^{(1)})$ is evidently also zero. As shown in figure 3.4b, the magnitude of the variable submergence $|\mathcal{S}^{(1)}|$ increases monotonically with object size and does so at a larger rate for density ratios closer to unity. Variable submergence is driven by the free surface elevation and governed by drag, dynamic buoyancy, and (added) mass, which are respectively the resistance, spring, and inertia terms of a forced spring-mass-damper system (cf. (3.33)). The larger the object, the more dominant is the acceleration of the free surface, which acts as an apparent force in the moving reference frame in which the variable submergence is defined, thus increasing the 'bobbing' of the object. The lower the density ratio, the stronger the buoyancy force and the stiffer the 'spring'. The response in variable submergence for a stiffer 'spring' is smaller. The argument of variable submergence $\arg(\mathcal{S}^{(1)})$ decreases monotonically with object size and growing importance of inertia but is dependent on the density ratio, as shown in figure 3.5b.

3.3.3 Second-order in wave steepness: $\mathcal{O}(\alpha^2)$

The equation of motion (3.1) resolved in the horizontal direction and at second order of approximation gives:

$$\ddot{x}_p^{(2)} = \frac{1}{m}\left(F_\tau^{(2)} - \partial_x \eta^{(1)}\Big|_{x_p^{(0)}} F_n^{(1)} \right). \tag{3.35}$$

In order to examine the wave-induced drift of a floating object in periodic waves, we consider the steady wave-averaged transport and set $\overline{\ddot{x}}_p^{(2)} = 0$, so that the resultant force must be zero. We will now consider the tangential and normal force contributions to (3.35) in turn.

The tangential and normal directions

In the tangential direction, the added-mass terms at second order can be obtained from the combination of an expansion in the horizontal and vertical displacements of the object, a coordinate transformation and evaluation of the advective derivative, respectively:

$$\begin{aligned} &M_\tau^{(2)} \\ &= \frac{C_m m}{\beta} \Big(\dot{u}_x^{(2)} + x_p^{(1)} \partial_x \dot{u}_x^{(1)}|_{\tilde{x}_p^{(0)}} \\ &\quad + \eta_p^{(1)} \partial_z \dot{u}_x^{(1)}|_{\tilde{x}_p^{(0)}} + \dot{u}_z^{(1)}|_{\tilde{x}_p^{(0)}} \partial_x \eta^{(1)}|_{x_p^{(0)}} + \dot{x}_p^{(1)} \partial_x u_x^{(1)}|_{\tilde{x}_p^{(0)}} + \dot{\eta}_p^{(1)} \partial_z u_x^{(1)}|_{\tilde{x}_p^{(0)}} - \dot{v}_\tau^{(2)} \Big) . \end{aligned} \tag{3.36}$$

In addition to the added-mass terms, the tangential force consists of a correction to the tangential component of gravity due to the object's horizontal displacement,

$$G_\tau^{(2)} = -mg \partial_{xx} \eta^{(1)} \Big|_{x_p^{(0)}} x_p^{(1)}, \tag{3.37}$$

and a tangential resistance force,

$$R_\tau^{(2)} = 3\pi \rho_f \nu D \left(\hat{A}_{\mathrm{s},\tau}^{(1)} \left(u_{\tau,p}^{(1)} - v_\tau^{(1)} \right) + \hat{A}_{\mathrm{s},\tau}^{(0)} \left(u_{\tau,p}^{(2)} - v_\tau^{(2)} \right) \right) . \tag{3.38}$$

For the first-order velocities, we have $u_{\tau,p}^{(1)} = u_x^{(1)}|_{\tilde{\mathbf{x}}_p^{(0)}}$ and $v_\tau^{(1)} = \dot{x}_p^{(1)}$. Noting from the coordinate transformation that $u_\tau = u_x + \partial_x \eta|_{x_p} u_z + \mathcal{O}(\alpha^3)$, we obtain for the second-order accurate horizontal fluid velocity at the object position:

$$u_{\tau,p}^{(2)} = u_x^{(2)}|_{\tilde{\mathbf{x}}_p^{(0)}} + \partial_x u_x^{(1)}|_{\tilde{\mathbf{x}}_p^{(0)}} x_p^{(1)} + \partial_z u_x^{(1)}|_{\tilde{\mathbf{x}}_p^{(0)}} \tilde{z}_p^{(1)} + \partial_x \eta^{(1)}|_{x_p^{(0)}} u_z^{(1)}|_{\tilde{\mathbf{x}}_p^{(0)}} . \tag{3.39}$$

We set the second-order Eulerian wave-induced velocity $u_x^{(2)}$ to zero for the regular waves we consider here. For the object's horizontal velocity we have at second order:

$$v_\tau^{(2)} = \dot{x}_p^{(2)} + \partial_x \eta^{(1)}|_{x_p^{(0)}} \dot{z}_p^{(1)}, \tag{3.40}$$

where $\dot{x}_p^{(2)}$ is the quantity that is ultimately of interest. Combining (3.39) and (3.40) and substituting into (3.38) gives:

$$\begin{aligned} R_\tau^{(2)} = 3\pi\rho_f \nu D \Bigg(& \hat{A}_{\mathrm{s},\tau}^{(1)} \left(u_x^{(1)}|_{\tilde{\mathbf{x}}_p^{(0)}} - \dot{x}_p^{(1)} \right) \\ & + \hat{A}_{\mathrm{s},\tau}^{(0)} \left(\partial_x u_x^{(1)}|_{\tilde{\mathbf{x}}_p^{(0)}} x_p^{(1)} + \partial_z u_x^{(1)}|_{\tilde{\mathbf{x}}_p^{(0)}} \eta_p^{(1)} - \dot{x}_p^{(2)} + \partial_x \eta^{(1)}|_{x_p^{(0)}} \dot{s}^{(1)} \right) \Bigg), \end{aligned} \tag{3.41}$$

where we have substituted $u_x^{(2)} = 0$, $\dot{z}_p^{(1)} = \dot{\eta}_p^{(1)} - \dot{s}^{(1)}$ and $u_z^{(1)}|_{\tilde{\mathbf{x}}_p^{(0)}} = \dot{\eta}_p^{(1)}$ from the linearised kinematic free surface boundary condition. We use the notation $\hat{A}_{\mathrm{s},\tau}^{(1)} = \hat{A}_{\mathrm{s},\tau}^{\prime(0)}(s^{(1)}/D)$ with $\hat{A}_{\mathrm{s},\tau}^{\prime(0)} \equiv \partial_{\hat{s}} \hat{A}_{\mathrm{s},\tau}(\hat{s})|_{\hat{s}^{(0)}}$ and $\hat{s} \equiv s/D$ according to (3.25).

In the normal direction, the total force at first order consists of a buoyancy force, an added mass and a resistance force already evaluated in (3.30), (3.31) and (3.32), respectively.

The wave-induced drift

Substituting the first-order solutions for $x_p^{(1)}$ (i.e. $X^{(1)} = 1$) for $s^{(1)}$ from (3.34) and for the wave quantities from table 3.1 and averaging over the waves, we obtain from (3.35), for the wave-induced drift of the object $\overline{v}_x = \overline{\dot{x}_p^{(2)}}$:

$$\begin{aligned} \overline{v}_x = \frac{u_S}{2} \Bigg[& \overbrace{2 - \underbrace{\mathcal{R}(\mathcal{S}^{(1)})}_{\substack{\text{Increases}\\ \text{drift}}}}^{\text{Adjusted Stokes drift}} + \frac{1}{\hat{A}_{\mathrm{s},\tau}^{(0)} \Gamma_R} \left(\underbrace{\overbrace{-\Gamma_B \mathcal{I}(\mathcal{S}^{(1)})}^{\substack{\text{Buoyancy}\\ \text{resolved into}\\ \text{the } x\text{-direction}}}}_{\text{Increases drift}} + \underbrace{\overbrace{\frac{C_m \mathcal{I}(\mathcal{S}^{(1)})}{\beta}}^{\text{Added mass}}}_{\text{Negligible effect}} \right) \\ & + \underbrace{\overbrace{\frac{\hat{A}_{\mathrm{s},n}^{(0)}}{\hat{A}_{\mathrm{s},\tau}^{(0)}} \mathcal{R}(\mathcal{S}^{(1)})}^{\text{Normal drag}}}_{\text{Reduces drift}} \Bigg], \end{aligned} \tag{3.42}$$

where $u_S = k_0 \omega_0 a_0^2$ is the Stokes drift. We define the drift amplification factor $X^{(2)} \equiv \overline{v_x}/u_S$, so that $X^{(2)}$ corresponds to what is inside the square brackets in (3.42) divided by 2. Equation (3.42) is the main result of this paper, and we will interpret it below. The text above the terms explains their physical

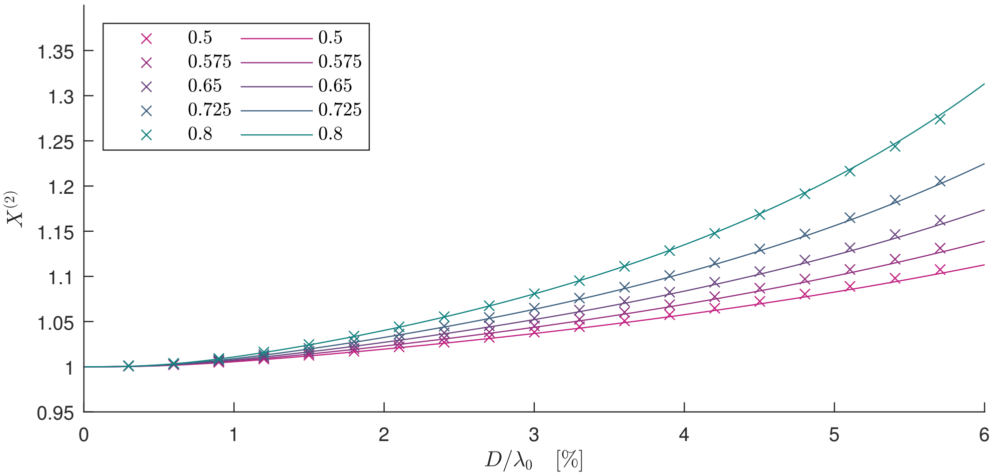

Figure 3.6: For viscous drag, wave-induced drift amplification $X^{(2)}$ as a function of dimensionless object size D/λ_0 for different density ratios $\beta = \rho_o/\rho_f$ (see legend). We have set $C_m = \beta/2$. Numerical and analytical solutions from perturbation theory are denoted by crosses and solid lines, respectively.

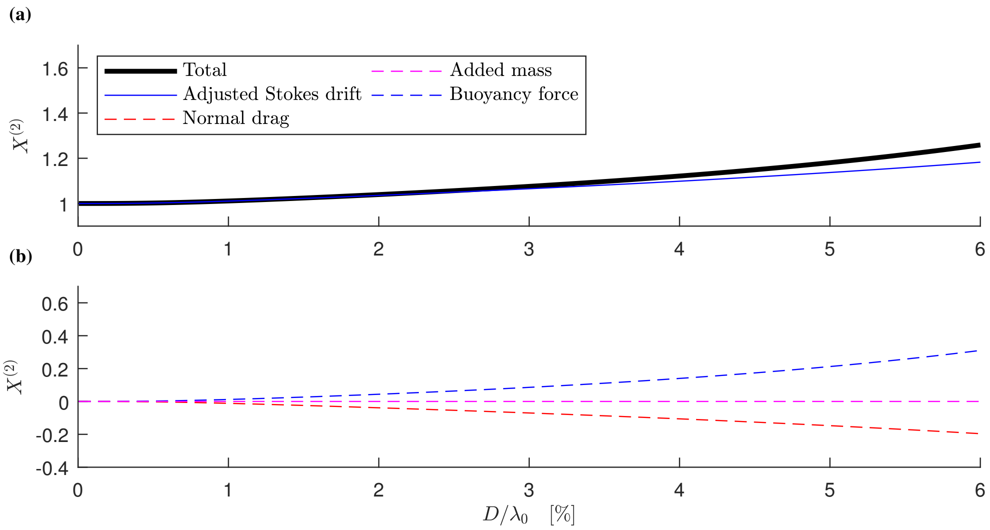

Figure 3.7: For viscous drag, contributions to the wave-induced drift amplification $X^{(2)}$ from the five components in (3.42) as a function of non-dimensional object size D/λ_0 for density ratio $\beta = 0.8$ and $C_m = \beta/2$.

origins and the text below their effect on the wave-induced drift of the object compared to the Stokes drift.

We begin by examining the wave-induced drift amplification factor $X^{(2)}$ as a function of object size and for different density ratios in figure 3.6. It is evident that the drift is enhanced and increasingly so for larger and heavier objects. Figure 3.7 examines the contributions to $X^{(2)}$ of the four components in (3.42): the adjusted Stokes drift, buoyancy resolved in the x-direction, normal drag, and added mass, which we will discuss in turn.

Adjusted Stokes drift

The adjusted Stokes drift terms in (3.42) reflect the change in the linear object trajectory. For unmodified horizontal motion ($X^{(1)} = 1$) and zero variable submergence ($\mathcal{S}^{(1)} = 0$), we obtain $X^{(2)} = 1$ from the adjusted Stokes drift terms alone. For larger objects, the increase in the vertical motion due to 'bobbing' of the object effectively increases the Stokes drift, as shown in figure 3.7.

Buoyancy resolved in the x-direction

The mechanism through which buoyancy when resolved in the x-direction and averaged over the wave cycle can increase the drift of an object is illustrated in figure 3.8. Without variable submergence (left column), the dynamic buoyancy force is simply zero. With variable submergence but without drag in the normal direction (middle column), the first-order buoyancy force resolved in the x-direction does not result in a net force on the object, as the first-order buoyancy force and the first-order slope required to resolve this force into the x-direction are out of phase. It is only in the presence of a drag in the normal direction (right column), that a phase lag in the submergence depth arises and a net force results. As shown in figure 3.7, the buoyancy force thus makes a relatively large contribution to the object's drift.

Normal drag

Although normal drag is required to create the phase difference that gives gives to the net buoyancy force resolved in the x-direction, normal drag also acts

<table>
<tr><th>No variable submergence</th><th>Variable submergence
No normal drag</th><th>Variable submergence
With normal drag</th></tr>
<tr><td colspan="3">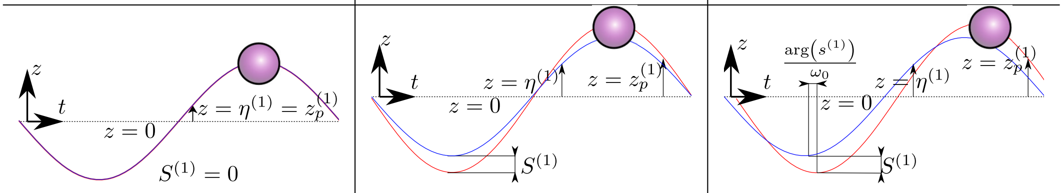
</td></tr>
<tr><td>$\mathcal{S}^{(1)} = 0$</td><td>$\mathcal{S}^{(1)}$ is real</td><td>$\mathcal{S}^{(1)}$ is complex</td></tr>
<tr><td>$\overline{s^{(1)}\partial_x\eta^{(1)}} = 0$</td><td>$\overline{s^{(1)}\partial_x\eta^{(1)}} = 0$</td><td>$\overline{s^{(1)}\partial_x\eta^{(1)}} = A_0^2 k_0 \frac{\mathcal{I}(\mathcal{S}^{(1)})}{2}$</td></tr>
<tr><td>$s^{(1)}$ is out of phase with $\partial_x\eta^{(1)}$.</td><td>The in-phase component of $s^{(1)}$ with $\partial_x\eta^{(1)}$ has a mean component in the x-direction.</td><td></td></tr>
<tr><td>No enhanced drift.</td><td>No mean component and no enhanced drift.</td><td>This mean component causes an enhanced drift.</td></tr>
</table>

Figure 3.8: Schematics of the object trajectory (red) and free surface (blue) for three cases: no variable submergence, variable submergence with no normal drag, and variable submergence with normal drag. The schematics illustrate the physical mechanism for increased drift arising from variable submergence $s^{(1)}$, where variable submergence and drag are in the n-direction, and a mean motion in the x-direction is created due to the slope of the free surface $\partial_x\eta^{(1)}$. For this illustration, we have chosen a density ratio $\beta = 1/2$.

to reduce the magnitude of the 'bobbing' and thus reduces the drift motion, as shown in fig. 3.4. The normal drag resolved into the horizontal direction opposes the buoyancy force resolved into the horizontal direction, with the balance resulting in a drift that is greater than the adjusted Stokes drift discussed above. Tangential drag, through the inverse dependence of $X^{(2)}$ on the projected area $\hat{A}_{s,\tau}^{(0)}$ and the effective drag coefficient Γ_R in (3.42), acts the reduce increase in object drift, by effectively 'anchoring' the object to the fluid and its Stokes drift.

Added mass

As at first order the object is accelerating in the normal direction, in addition to the buoyancy force and the normal drag discussed above, an added mass term has to be take into account. As shown in fig. 3.4, its contribution is a relatively small reduction in drift.

3.3.4 Limitation on validity of viscous drag

Although the analysis above has demonstrated how enhanced drift of non-infinitesimal objects may arise, the underlying assumption of viscous drag places an upper limit on object size. We estimate the maximum Reynolds number that arises from the linear motion in the normal direction:

$$\mathrm{Re}_{\max} = \frac{a_0\omega_0\ |\mathcal{S}^{(1)}|D}{\nu} \leq 2, \tag{3.43}$$

where we take 2 to be the maximum Reynolds number for drag to be considered viscous. Noting that $\mathcal{S}^{(1)}(D/\lambda_0, \beta)$ and for $\beta = 0.8$, we obtain from (3.43) for the maximum diameter:

$$\mathcal{S}^{(1)}\left(D_{\max}/\lambda_0, \beta = 0.8\right)\left(D/\lambda_0\right) = \frac{k_0^2\nu}{\alpha\omega_0\pi}. \tag{3.44}$$

For a typical laboratory water wave of steepness $\alpha = 0.1$ and frequency $f_0 = 1.25$ Hz, the right-hand side of (3.44) becomes equal to 1.6×10^{-5}. Fitting a linear curve $S^{(1)} = 5.8D/\lambda_0$ to figure 3.4b, we can solve the quadratic (3.44) in D/λ_0 and obtain a maximum diameter to wavelength ratio of 0.2% corresponding to $\mathrm{Re}_{\max} = 2$. Examining figure 3.6, we can conclude that for such small objects drift enhancement is negligible. We therefore have to consider the non-viscous drag formulation (3.18) in our model, which requires numerical solutions, as examined in the next section.

3.4 Numerical solutions

To validate the perturbation theory for viscous drag in §3.3 and to explore the predictions of our model for non-viscous drag, we set out to obtain numerical solutions of our model. Specifically, we solve the set of differential equations

(3.45-3.47) with the forces described in detail in §3.2 using a numerical ordinary differential equation solver. The fluid velocity and free surface elevation from table 3.1 are used as input.

We start our numerical solutions from an initial condition without waves with the object depth set at the static submergence given by numerical solution of (3.24). Avoiding initial transients, we then ramp up the wave forcing using half of a Gaussian envelope to a steady state. A convergence study showed that a Gaussian half width set to 20 wavelengths was sufficient to avoid initial transients. Once the object motion reaches steady state, its motion components in the x and z directions are effectively linearised using a band-pass filter between $0.8f_0$ and $1.2f_0$. The linear phase was found using the cross-correlation of the linearised object motion and the linearised Eulerian velocity evaluated at the object position in both directions. The object drift velocity is calculated as the gradient of a straight line fitted to the sub-harmonic $x(t)$ motion obtained by low-pass filtering at $0.5f_0$. We will now consider viscous and non-viscous drag in turn. Section 3.C discusses the small-object limit of the numerical solutions.

3.4.1 Viscous drag

For the viscous drag formulation, the crosses in figures 3.4, 3.5 and 3.6 display the numerical solutions of the model for a (small) steepness $\alpha = 0.02$. The agreement with the perturbation theory solutions shown as continuous lines for both the first-order amplitudes (figure 3.4) and phases (figures 3.5) and the second-order drift (figure 3.6) is near perfect. Any discrepancy between perturbation theory and numerical simulations that could arise in these figures would be caused by higher-order terms (beyond second-order) in steepness that are effectively included in the numerical simulations. The comparison thus acts solely to confirm the accuracy of our perturbation theory solutions.

3.4.2 Non-viscous drag

In this section we use the non-viscous drag expression with the drag coefficient given by (3.18). Discrepancies in predicted drag by different formulations become significant as the object becomes large and the Reynolds number increases. For the non-viscous drag formulation, we examine simulations at both

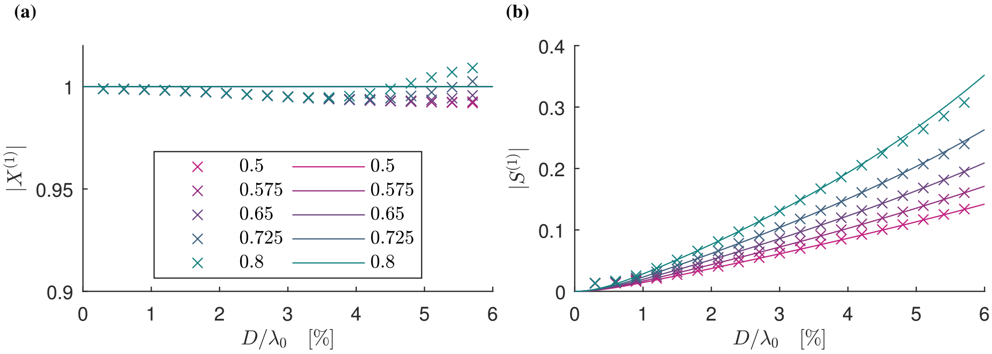

Figure 3.9: Laboratory scale numerical simulation results using non-viscous drag for magnitudes of the first-order horizontal motion amplification $X^{(1)}$ (a) and the variable submergence $\mathcal{S}^{(1)}$ (b) as functions of dimensionless object size D/λ_0 for different density ratios $\beta = \rho_o/\rho_f$, where the density ratio for each colour is shown in the legend. We have set $C_m = \beta/2$. Numerical and analytical solutions from perturbation theory are denoted by crosses and solid lines, respectively.

laboratory (see §3.5 for further details) and at field scale, as considered separately below.

Laboratory scale

At laboratory scale, we set $f_0 = 1.25$ Hz, corresponding to $\lambda_0 = 1.0$ m and $\alpha = 0.1$. With object diameters up to $D = 60$ mm, we obtain $D/\lambda_0 = 6\%$, where we concluded in §3.3.4 the limit of validity for viscous drag is $D/\lambda_0 = 0.2\%$. At laboratory scale, figure 3.9 compares the analytically predicted linear motion using viscous drag with the corresponding numerical results using non-viscous drag. The response in the normal direction is unchanged because the forcing is inertial with little effect from the drag. As the object size increases, inertia increasingly dominates over drag. A small decrease in the horizontal linear motion is evident growing to a few percent for larger objects. The results for small objects are the same because the non-viscous drag recovers viscous drag in the small object limit.

The drift amplification increases slightly when using non-viscous drag for larger objects, as seen in figure 3.10. This is because the (tangential) drag force for larger objects is lower for non-viscous drag than for viscous drag, resulting in a reduced resistance to increases in drag above the Stokes drift.

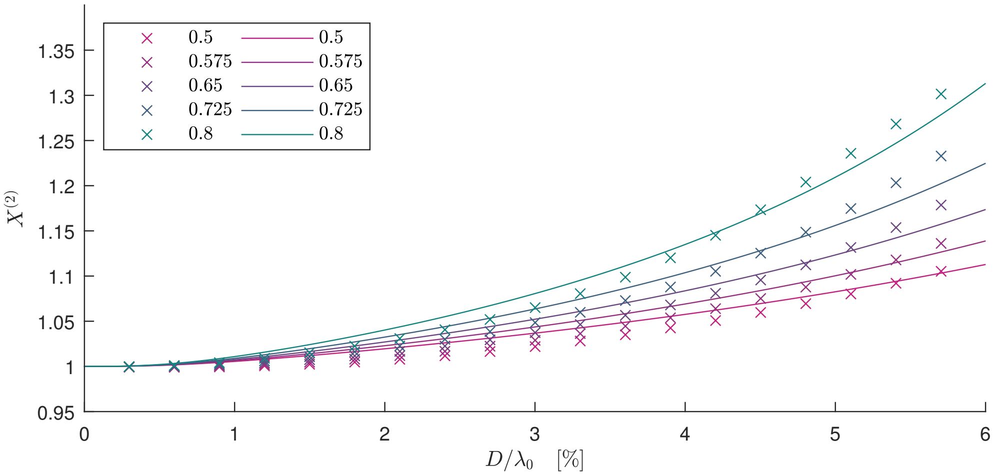

Figure 3.10: Laboratory scale numerical simulation results using non-viscous drag for wave-induced drift amplification $X^{(2)}$ as a function of dimensionless object size D/λ_0 and for different density ratios $\beta = \rho_o/\rho_f$ (see legend). We have set $C_m = \beta/2$. Analytical solutions using viscous drag from perturbation theory are denoted by solid lines.

Field scale

We set a wave frequency of $f_0 = 0.2$ Hz and a steepness of $\alpha = 0.05$ to represent a typical wind wave at field scale. The frequency of 0.2 Hz corresponds to the peak in the spectrum with $\alpha = 0.05$ at the upper end of the steepness range for wind waves in the ocean [Toffoli and Bitner-Gregersen, 2017]. This steepness corresponds to a dimensional wave amplitude of $a_0 = 0.3$ m. The difference between viscous and non-viscous drag will be larger at field scale owing to the higher Reynolds numbers.

Figure 3.11a shows the linear horizontal motion, which is mostly unchanged from the perturbation theory result. The magnitude of variable submergence is inertially driven and thus very similar to the viscous analytical result shown in fig. 3.11b, although its phase will be different (not shown).

The drift amplification for field scale simulations using non-viscous drag shown in fig. 3.12 is greater than the perturbation theory result based on viscous drag, even more so than at laboratory scale. This is because the non-viscous drag force is now considerably smaller than its viscous equivalent taken outside the range of Reynolds numbers for which it is valid. As for at laboratory scale,

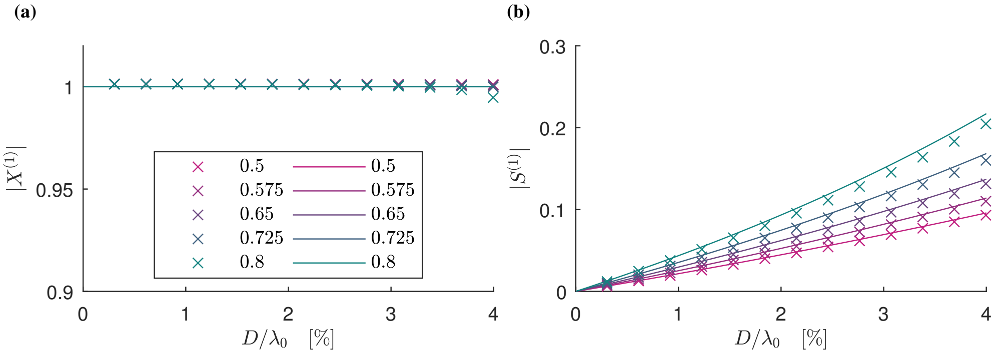

Figure 3.11: Field scale numerical simulation results using non-viscous drag for magnitudes of the first-order horizontal motion amplification $X^{(1)}$ (a) and the variable submergence $\mathcal{S}^{(1)}$ (b) as functions of dimensionless object size D/λ_0 for different density ratios $\beta = \rho_o/\rho_f$, where the density ratio for each colour is shown in the legend. Field scale here denotes a 0.2 Hz wave with a steepness of $\alpha = 0.05$. We have set $C_m = \beta/2$. Numerical and analytical solutions from perturbation theory are denoted by crosses and solid lines, respectively.

the (tangential) drag force for larger objects is lower for non-viscous drag than for viscous drag, resulting in a reduced resistance to increases in drag above the Stokes drift.

Using the results from field scale numerical simulations for non-viscous drag, a 1 m diameter object of density $\rho_p = 0.9 \ \text{g/cm}^3$ results in a 50% increase in drift ($X^{(2)} = 1.5$). This is a significant increase compared to the Stokes drift infinitesimal objects would experience. For comparison, a 0.1 m diameter object in the same wave field does not experience any drift amplification ($X^{(2)} = 1$) and behaves as a perfectly Lagrangian tracer.

3.5 Wave flume experiments

3.5.1 Set-up and data acquisition

To validate our model, we have conducted a series of object tracking experiments in the Sediment Wave Flume in the Coastal, Ocean and Sediment Transport (COAST) Laboratory at the University of Plymouth, UK. The flume has length 35 m, width 0.60 m, and was filled with water to 0.50 m depth, as shown in figure 3.13. A double-element piston-type wavemaker supplied by Edinburgh

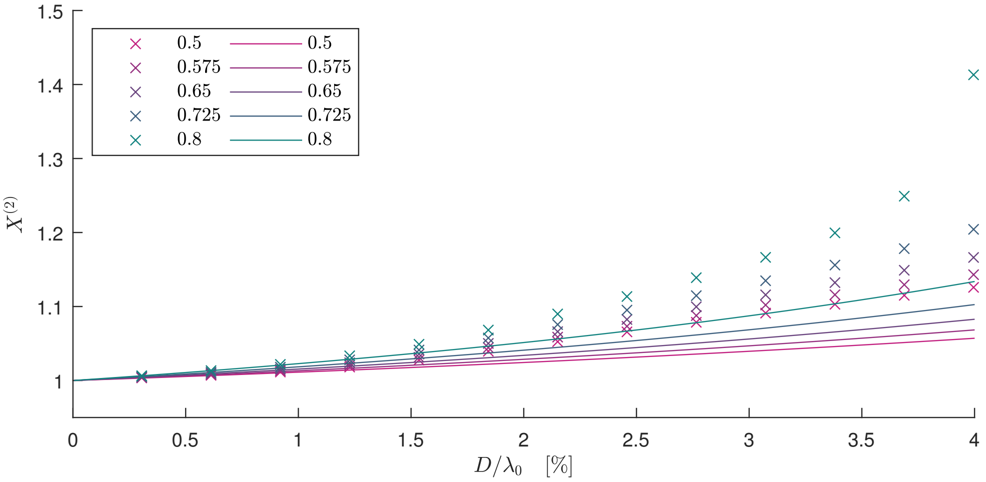

Figure 3.12: Field scale numerical simulation results using non-viscous drag for the wave-induced drift amplification $X^{(2)}$ as a function of dimensionless object size D/λ_0 for different density ratios $\beta = \rho_o/\rho_f$ (see legend). Field scale here denotes a 0.2 Hz wave with a steepness of $\alpha = 0.05$. We have set $C_m = \beta/2$. Analytical solutions using viscous drag from perturbation theory are denoted by solid lines.

Designs Ltd (EDL) was used to generate a wavepacket with a spectral shape that linearly focuses to a Gaussian packet, $A_0 = a_0 \exp\left(-(x_f - c_{g,0}t)^2/2\sigma^2\right)$, at a measurement zone centred $x_f = 9.75$ m from the rest position of the wavemaker. The wavepacket was made as long as possible to make it quasi-monochromatic whilst avoiding reflection ($\epsilon = 1/(k_0\sigma) = 0.04$) with a steepness $\alpha = a_0 k_0 = 0.1$ and peak frequency $f_0 = 1.25$ Hz.

Despite our perturbation theory solutions being for periodic waves, we use quasi-monochromatic wavepackets in our laboratory experiments because wave-induced transport is much easier to measure experimentally for wavepackets (see van den Bremer et al. [2019] and Calvert et al. [2019] and the discussion in Monismith [2020]). In appendix 3.B, we confirm that the slow modulation associated with the wavepacket does not result in any additional non-inertial behaviour of the object. As a result, our model predictions for periodic waves and the wavepackets considered in our experiments are equivalent.

We control the wavemaker using linear wave theory. Although sub-harmonic error waves at second order generated for wavepackets (e.g. Nielsen and Baldock [2010], Orszaghova et al. [2014]) can lead to spurious wave-induced dis-

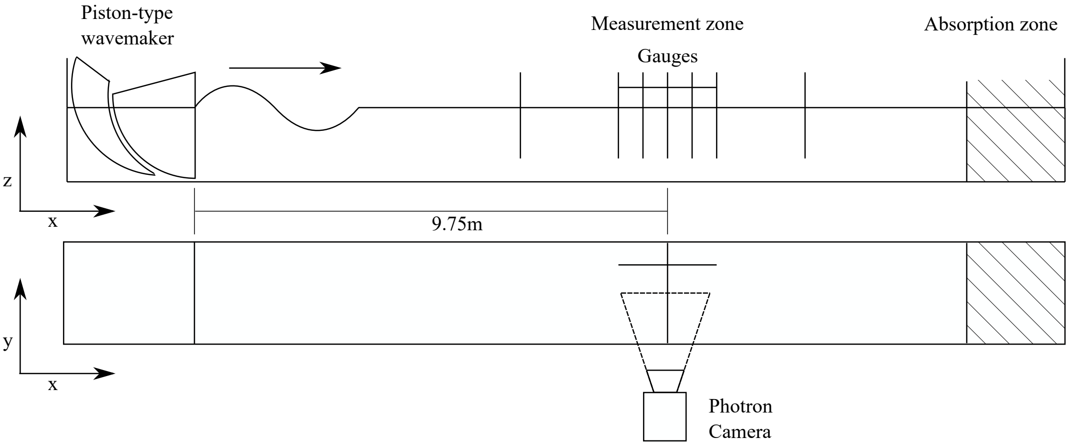

Figure 3.13: Experimental set-up used to track the motion of floating objects under wave motion generated by a double-element piston-type wave maker at the COAST Laboratory, University of Plymouth, UK.

placements [Calvert et al., 2019], these displacements are negligibly small for the deep-water waves we consider [van den Bremer et al., 2019].

Seven resistance-type wave gauges provided 128 Hz free surface elevation measurements. Five gauges were located close to the focus location at 15 cm intervals, as shown in figure 3.13 . Two gauges were located significant distances before and after the focus location. After propagating through the measurement zone, the dispersed wavepackets were absorbed by mesh-filled wedges within an absorption zone located at the downstream end of the wave flume. To ensure near-quiescent initial conditions for each experiment, the water surface was allowed to settle for 10 minutes between experiments. A Photron SA4 high-speed camera captured the object motions at 125 frames/s, resolution of 1024 by 1024 pixels, and shutter speed of 1/125 s. Optical distortion was removed using 35 mm chequerboard images and MATLAB's inbuilt image processing package.

3.5.2 Matrix of experiments

In our experiments, we have chosen a peak frequency of $f_0 = 1.25$ Hz, corresponding to a wavelength of $\lambda_0 = 1.0$ m and non-dimensional water depth $k_0 d = 3.1$. We then vary systematically the diameter D and the density ρ_o of the spherical floating object, with values for our 16 experiments listed in table 3.2. The object size was limited by camera resolution and the MATLAB track-

Experiment	D [m]	ρ_o [kgm^{-3}]	D/λ_0 [%]	β [-]
1	0.051	508	5.1	0.51
2	0.051	551	5.1	0.55
3	0.051	620	5.1	0.62
4	0.051	703	5.1	070
5	0.038	597	3.8	0.60
6	0.038	637	3.8	0.63
7	0.038	678	3.8	0.68
8	0.038	750	3.8	0.75
9	0.025	649	2.5	0.65
10	0.025	678	2.5	0.68
11	0.025	700	2.5	0.70
12	0.025	809	2.5	0.81
13	0.019	647	1.9	0.65
14	0.019	679	1.9	0.68
15	0.019	654	1.9	0.65
16	0.019	807	1.9	0.81

Table 3.2: Matrix of experiments listing dimensional object diameter D, object density ρ_o, non-dimensional object diameter D/λ_0, and density ratio $\beta = \rho_o/\rho_f$.

ing algorithm. The density was varied by filling hollow spheres with different ratios of epoxy to glass micro-ball filler. Each experiment was repeated five times.

3.5.3 Data processing

Free surface elevation

The wavepackets were created from narrow-banded spectra to allow frequency filtering to separate the linear and second-order sub-harmonic components in the wave gauge signal. A band-pass filter between $0.8f_0$ and $1.2f_0$ was used to extract the linear free surface elevation. The measured envelope A_0 was calculated using the Hilbert transform of the linear free surface elevation. Use of the measured envelope at the location where the trajectories were measured, to calculate purely Lagrangian displacement, accounts for any dissipation or non-linear dispersion between the wavemaker and the zone of interest.

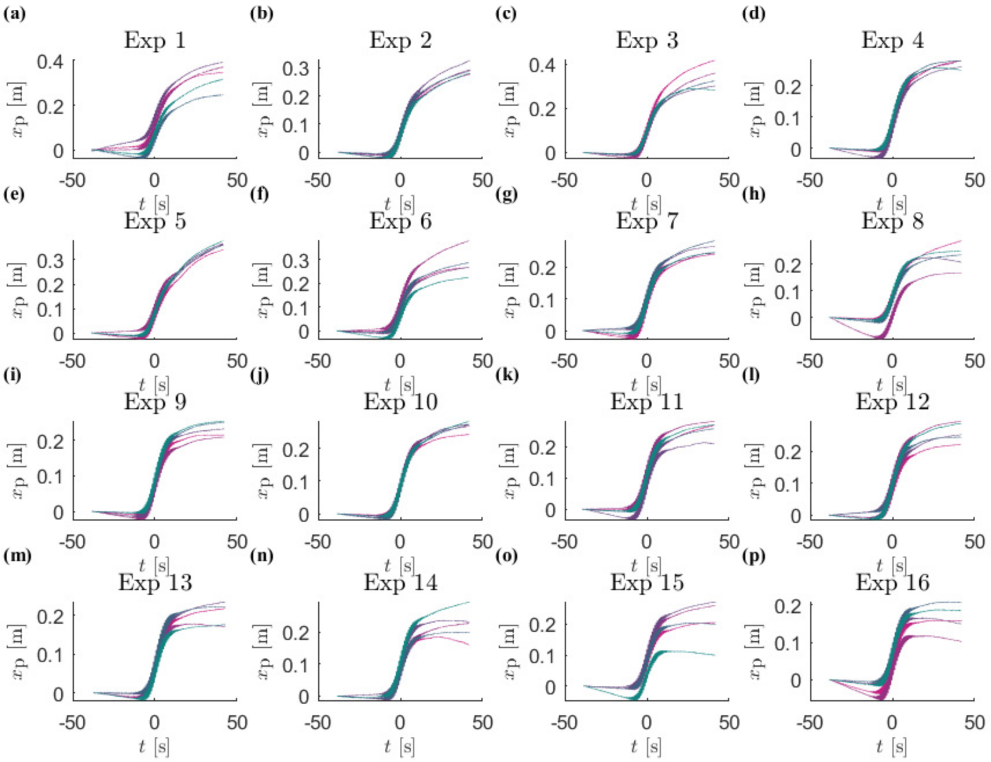

Figure 3.14: Time histories of object horizontal position for each experiment. Each panel shows the five repeated experiments in different colours.

Object tracking

Profile images of the floating white spheres were illuminated from various angles and captured by the Photron camera. The trajectories of the floating objects were tracked by identifying their position in each frame using a circle finding algorithm. The apparent size of the circle in the image was used to calibrate the pixel scale against the known size of the sphere. This also reduced any errors from out-of-plane motion not captured by the single camera. The horizontal components of the raw trajectories, repeated five times, are shown in figure 3.14.

Every effort was made to settle the sphere at the start of each experiment in order to give it a zero initial velocity. This was not completely possible due to air flows over the water surface and slight disturbance from human touch. A linear fit in the time domain, assuming a constant pre-existing drift velocity, was used to remove motion before the arrival wavepacket from the raw orbits in figure 3.14. The focus location was determined as coinciding with the position of the maximum of the linearised vertical motion envelope of the object. The difference in object location and exact focus location in the flume had negligible effect because of the very long wavepackets used.

The magnitudes of the linear response were determined by filtering the horizontal and vertical motion components with a band-pass filter of 0.8-$1.2f_0$, followed by a Hilbert transform to obtain the envelope A_0. Note that frequency filtering was only applied to velocities, and numerical integration was used to calculate displacements. The maximum magnitude of the envelope were then normalised by wave amplitude a_0 to obtain $X^{(1)}$ and unity subtracted from the normalised vertical motion to give $\mathcal{S}^{(1)}$ (the normal and vertical directions equivalent up to first-order accuracy). We were not able to extract the linear phase from the experiments because exact spatial and temporal matching of Eulerian wave-gauge data and Lagrangian object positions could not be achieved. A low-pass filter at $0.5f_0$ was used to extract the sub-harmonic horizontal velocity component. The drift value $X^{(2)}$ was then determined by subtracting the Eulerian return flow from the maximum value of the sub-harmonic horizontal velocity component flow and dividing by the Stokes drift.

3.6 Comparison between theory and experiments

3.6.1 First-order in wave steepness: $\mathcal{O}(\alpha)$

Figure 3.15 presents the first-order magnitudes $|X^{(1)}|$ and $|\mathcal{S}^{(1)}|$ as functions of dimensionless diameter (D/λ_0) for each experiment, with the colour corresponding to the density ratio. Comparison is made with numerical solutions of our model for non-viscous drag and analytical solutions using viscous drag. Overall, the horizontal motion in figure 3.15a is of similar magnitude to what is theoretically predicted $(X^{(1)})$ with some variability, as quantified by the error bars. We note that a decrease of a few percent in the numerical simulation solutions to $|X^{(1)}|$ is equivalent to a (small) dimensional decrease in the horizontal motion less than 1 mm. The first-order variable submergence $|\mathcal{S}^{(1)}|$ in figure 3.15b increases monotonically with dimensionless diameter (D/λ_0), as predicted by theory.

The experiments do not show a consistent trend with density for either linear motion component. We note that the densities are not equally spaced

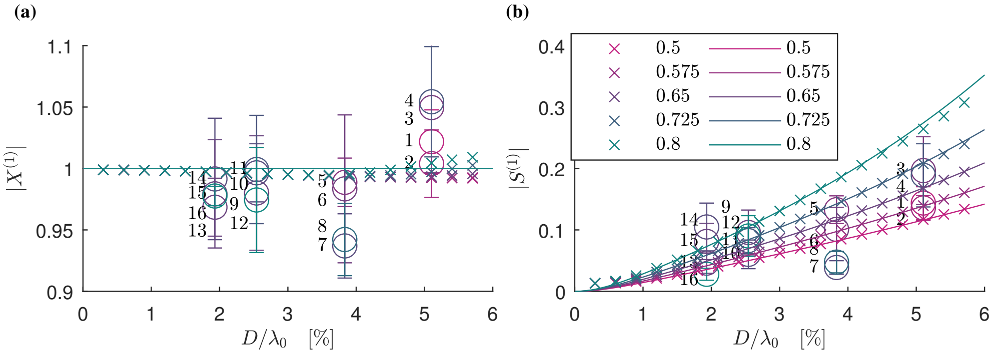

Figure 3.15: Magnitude of the first-order motion as a function of non-dimensional object size D/λ_0 for different density ratios (see legend): analytical solution with viscous drag (solid lines), numerical solution with quadratic drag (crosses) and experiments (circles). The density ratios for the numerical solutions are listed in the legend; density ratios for the experiments are labelled using the same colour scale. The error bars are obtained from repeated experiments and correspond to two standard deviations.

or the same for each size sphere owing to practical constraints on filling the spheres with different ratios of epoxy to glass micro-ball filler (see table 3.2 for the experimental matrix). The error bars shown for each experiment, which are twice the standard deviation of the five repeats, are large enough to mask any trend in density. Although we could measure the overall density of the spheres accurately, we emphasize that we were not able to measure its uniformity within the sphere.

Errors could have arisen from various physical sources that can account for the relatively large standard deviations. The initial motion of the object was hard to eliminate. Air conditioning was switched off, but there were sometimes air flows over the flume. The method of taking the value of sub-harmonic velocity at the peak of the wavepacket has been shown to numerically match regular waves in section 3.B. However, inertia on the packet scale can be seen in figure 3.16 as the velocity does not go to zero after the packet passes. Ten minutes was left between experiments for the flume to settle, but there may have been residual currents still present.

3.6.2 Second-order in wave steepness: $\mathcal{O}(\alpha)$

Figure 3.16 presents time histories of the normalised sub-harmonic horizontal object velocity component for all 16 experiments, having first removed motion ahead of the wavepacket and the Eulerian mean flow associated with the wavepacket. In all cases, the non-dimensional sub-harmonic horizontal object velocity exceeds or is very close to unity near focus, has a Gaussian-like profile, reducing close to zero within about 25 s either side of focus. The distributions are slightly skewed, with a faster rising limb than falling. There is more variability after focus than before. Using the peak values from figure 3.16, figure 3.17 shows the dimensionless drift factor $X^{(2)}$ for each experiment as a function of dimensionless diameter, with colour indicating density ratio. Drift increases with non-dimensional diameter and, as for the first-order results, the trend with density is unclear from the experiments and masked by substantial variability. We note that the density of floating plastic in the ocean typically has a small range between 800-1000 kg/m^3 and may thus be a less important variable than object size. The trend with object size is consistent between experiments and theory, both presenting a similar increase with size.

3.7 Conclusions

In this paper, we have developed a model for the transport of spherical, finite-size, floating marine debris by deep-water waves. Using a Stokes-like expansion in wave steepness, we have derived closed-form solutions for the linear response and the wave-induced drift of an object forced by regular waves and experiencing viscous drag. These closed-form solutions match numerical solutions of our model in the case of viscous drag. Our model recovers the Lagrangian limit as object size tends to zero, meaning that small objects are simply transported with the Stokes drift of the surface gravity waves.

Through our perturbation solutions, we have identified two mechanisms for increased drift. The first arises from the change in magnitude of the linear orbits, especially its vertical component. The second arises when an out-of-phase variable submergence is resolved in the horizontal direction by the slope of the free surface. The second mechanism requires buoyancy and drag to be acting normal to the free surface, where the drag is required to create the phase

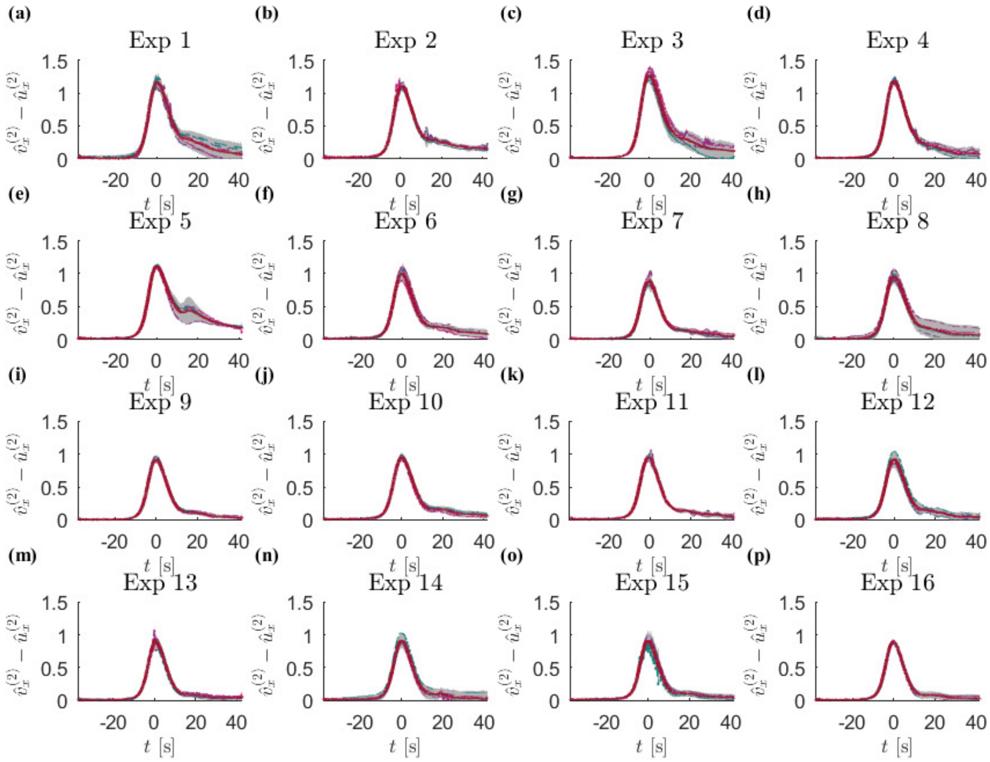

Figure 3.16: Sub-harmonic horizontal object velocity $v_x^{(2)}$, or object drift, relative to the Eulerian mean flow $u_x^{(2)}$ as a function of time for each experiment, which has been normalized by the Stokes drift at the centre of the packet, $u_{\mathrm{S}}(t=0, x=x_f) = \omega_0 k_0 a_0^2$. Values at the peak greater than unity denote that the object is drifting at a greater rate than a purely Lagrangian tracer because the object drift of a purely Lagrangian tracer would equal the Stokes drift plus Eulerian return flow [Calvert et al., 2019, van den Bremer et al., under review]. The mean of the five repeated experiments is shown as a continuous red line, and the confidence band corresponding to two standard deviations is shaded in grey, with five lines overlaid for each individual experiment.

difference that gives rise to the drift when averaged over the wave cycle. In any realistic oceanographic scenario, a non-viscous drag is required in order for the drift amplification to be significant. To validate our model, we have carried out laboratory wave flume experiments for a range of object sizes and densities. The experiments present a similar trend with object size to our model predictions for non-viscous drag, but no discernible trend with density ratio, probably due to relatively large experimental error.

Our experiments are at laboratory scale where a significant increase in drift is observed. The main driver for an increased drift has been shown to be an

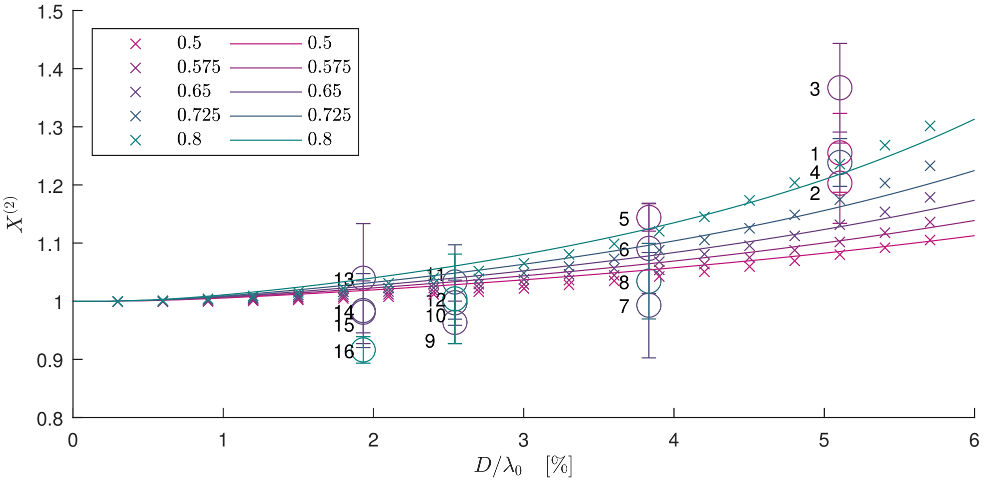

Figure 3.17: Second order drift amplification factor $X^{(2)}$ as a function of non-dimensional object size for different density ratios (see legend): analytical solution with viscous drag (solid lines), numerical solution with quadratic drag (crosses) and experiments (circles). The density ratios for the numerical solutions are listed in the legend; density ratios for the experiments are labelled using the same colour scale. The error bars are obtained from repeated experiments and correspond to two standard deviations.

object's size relative to the wavelength. Thus, in the real ocean, where wavelengths range from 10-10^3 m, increased drift will likely only be observed where shorter wavelengths are present, such as in gulfs or smaller seas. Modelling an object with a diameter of 1 m and density of 0.9 g/cm^3 floating on a wave with a 5 s period and a steepness of $\alpha \equiv k_0 a_0 = 0.05$, typical of a moderately steep wind wave, results in a 50% increase in wave-induced drift compared to the Stokes drift for such a wave. In the same wave field, an object with a diameter of 0.1 m would not experience an increase in drift at all. Further experiments are recommended at larger scale, covering a wider range of object sizes and considering the effect of object shape. Insights from the present work should be useful in the development of more sophisticated models for tracking floating marine litter.

Acknowledgement

TSvdB acknowledges a Royal Academy of Engineering Research Fellowship.

Declaration of interests

The authors report no conflict of interest.

Appendix

3.A Equations of motion

Substituting (3.8) and (3.9) into (3.7), and thence into (3.1) results in two second-order differential equations in the (n, τ) coordinate system:

$$\begin{aligned}
&\ddot{\tau}_p - \left(-(\partial_x \eta|_{x_p})^2 \Xi_p + \partial_{xx}\eta|_{x_p} \Xi_p^2 n_p\right) \ddot{x}_p = \frac{1}{m(1+\frac{C_m}{\beta})} F_\tau + \Big\{ 2\dot{\theta}_p \dot{n}_p + (\dot{\theta}_p)^2 \tau_p \\
&- \partial_x \eta|_{x_p} \Xi_p \left(\partial_{tt}\eta|_{x_p} + 2\dot{x}_p \partial_{tx}\eta|_{x_p} + (\dot{x}_p)^2 \partial_{xx}\eta|_{x_p}\right) + n_p \Big[\left(\partial_{tx}\eta|_{x_p} + \dot{x}_p \partial_{xx}\eta|_{x_p}\right) 2\Xi_p \dot{\Xi}_p \\
&+ \left(\partial_{ttx}\eta|_{x_p} + 2\dot{x}_p \partial_{txx}\eta|_{x_p} + (\dot{x}_p)^2 \partial_{xxx}\eta|_{x_p}\right) \Xi_p^2 \Big] \Big\} ,
\end{aligned} \tag{3.45}$$

$$\begin{aligned}
&\ddot{n}_p + \left(\partial_x \eta|_{x_p} \Xi_p + \partial_{xx}\eta|_{x_p} \Xi_p^2 \tau_p\right) \ddot{x}_p = \frac{1}{m(1+\frac{C_m}{\beta})} F_n - \Big\{ 2\dot{\theta}_p \dot{\tau}_p - (\dot{\theta}_p)^2 n_p \\
&+ \Xi_p \left(\partial_{tt}\eta|_{x_p} + 2\dot{x}_p \partial_{tx}\eta|_{x_p} + (\dot{x}_p)^2 \partial_{xx}\eta|_{x_p}\right) + \tau_p \Big[\left(\partial_{tx}\eta|_{x_p} + \dot{x}_p \partial_{xx}\eta|_{x_p}\right) 2\Xi_p \dot{\Xi}_p \\
&- \left(\partial_{ttx}\eta|_{x_p} + 2\dot{x}_p \partial_{txx}\eta|_{x_p} + (\dot{x}_p)^2 \partial_{xxx}\eta|_{x_p}\right) \Xi_p^2 \Big] \Big\} ,
\end{aligned} \tag{3.46}$$

where we have kept all the second-order time derivatives on the left-hand side. We now have two equations in terms of three second-order time derivatives, namely $\ddot{\tau}_p$, $\ddot{n}_p$ and $\ddot{x}_p$, and require a third equation to solve the system. We obtain this third (kinematic) equation by taking the dot product of (3.7), in which we have substituted for $\ddot{\theta}_p$ and $\ddot{\eta}_p$ from (3.8) and (3.9), and $\mathbf{e}_x$, giving:

$$\begin{aligned}
&\ddot{x}_p \left[1 + \partial_{xx}\eta|_{x_p}\Xi_p^3 \left(n_p + \partial_x\eta|_{x_p}\tau_p\right)\right] - \ddot{\tau}_p\Xi_p + \ddot{n}_p\partial_x\eta|_{x_p}\Xi_p = \\
&\Xi_p \Big\{-n_p \Big[\left(\partial_{tx}\eta|_{x_p} + \dot{x}_p\partial_{xx}\eta|_{x_p}\right) 2\Xi_p\dot{\Xi}_p + \big(\partial_{ttx}\eta|_{x_p} + 2\dot{x}_p\partial_{txx}\eta|_{x_p} \\
&+ (\dot{x}_p)^2\partial_{xxx}\eta|_{x_p}\big)\, \Xi_p^2\Big] - 2\dot{\theta}_p\dot{n}_p - (\dot{\theta}_p)^2\tau_p - \partial_x\eta|_{x_p} \Big[\tau_p \Big[\left(\partial_{tx}\eta|_{x_p} + \dot{x}_p\partial_{xx}\eta|_{x_p}\right) 2\Xi_p\dot{\Xi}_p \\
&+ \left(\partial_{ttx}\eta|_{x_p} + 2\dot{x}_p\partial_{txx}\eta|_{x_p} + (\dot{x}_p)^2\partial_{xxx}\eta|_{x_p}\right) \Xi_p^2\Big] + 2\dot{\theta}_p\dot{\tau}_p - (\dot{\theta}_p)^2 n_p\Big]\Big\} .
\end{aligned} \tag{3.47}$$

3.B Wavepackets vs. periodic waves

We use numerical solutions (see §3.4) to the model developed in §3.2 to examine the difference in predictions for objects subject to the quasi-monochromatic wavepackets we use in our experiments and periodic waves. The processing of the trajectory data from the numerical simulations using wavepackets was the same as for the experiments described in §3.5. Figure 3.18 shows the almost identical first-order response as a function of non-dimensional object diameter at different density ratios for periodic waves (crosses) versus wavepackets of the same bandwidth as in experiments (circles). Figure 3.19 shows the corresponding second-order drift amplification factors. Very slight differences are only predicted for larger object sizes for which the role of inertia is more dominant. For wavepackets, a slightly smaller drift motion is predicted, because the time required for inertial objects to reach steady state is longer for larger objects.

3.C Limiting behaviour of the numerical solutions

To confirm the model developed in §3.2 is correct, including its cumbersome coordinate transforms, we examine the perfectly Lagrangian limit (§3.C.1) and the small-object limit (§3.C.2) of its numerical solutions obtained using MATLAB's ODE15s solver.

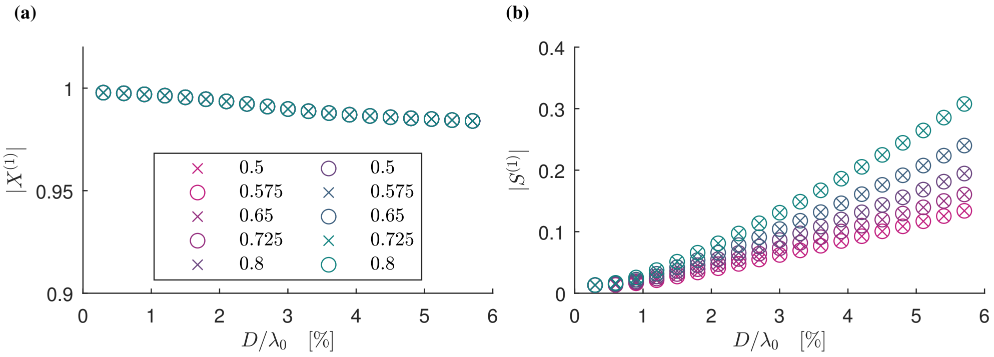

Figure 3.18: Numerical solutions for magnitude of the first-order horizontal motion amplification $X^{(1)}$ (a) and the variable submergence $\mathcal{S}^{(1)}$ (b) as functions of dimensionless object size D/λ_0 for non-viscous drag and for different density ratios $\beta = \rho_o/\rho_f$ (see legend). In the figure, periodic waves are denoted by crosses and wavepackets of the same bandwidth as in the experiments by circles.

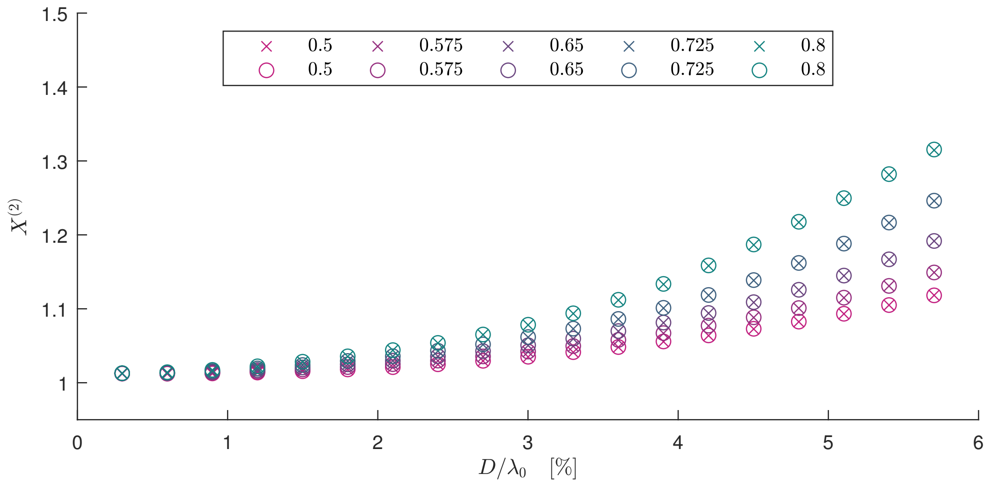

Figure 3.19: Numerical solutions for magnitude of the second-order horizontal motion amplification $X^{(2)}$ as functions of dimensionless object size D/λ_0 for non-viscous drag and for different density ratios $\beta = \rho_o/\rho_f$ (see legend). In the figure, periodic waves are denoted by crosses and wavepackets of the same bandwidth as in the experiments by circles.

3.C.1 The Lagrangian limit

To obtain the Lagrangian limit, we replace the forces on the object by the accelerations a Lagrangian particle would experience under linear periodic waves:

$$\ddot{x}_p = a_0\omega_0^2 \sin(\varphi) \exp\left(k_0 z_p\right), \quad \ddot{z}_p = -a_0\omega_0^2 \cos(\varphi) \exp\left(k_0 z_p\right), \tag{3.48a,b}$$

where $\varphi = k_0 x_p - \omega_0 t + \varphi_0$. The accelerations are then mapped to the translating coordinate system and expressed in the (n, τ)-directions. The system is then solved numerically in (n, τ)-coordinates and the results mapped back onto (x, z)-coordinates, providing confirmation our transformations are correct. As shown in figure 3.20, we obtain the correct amplitude of the vertical and horizontal linear motion and the correct Stokes drift.

3.C.2 Small-object limit

As object size tends to zero, $D \to 0$, the solution should recover the behaviour of a perfectly Lagrangian tracer. This has been explicitly checked by numerically solving for an object of non-dimensional diameter $D/\lambda_0 = 1 \times 10^{-6}$, which results in $X^{(1)} = 1.00$, $\mathcal{S}^{(1)} = 0.00$ and $X^{(2)} = 1.00$. These correct limits are shown in figures 3.15 and 3.17.

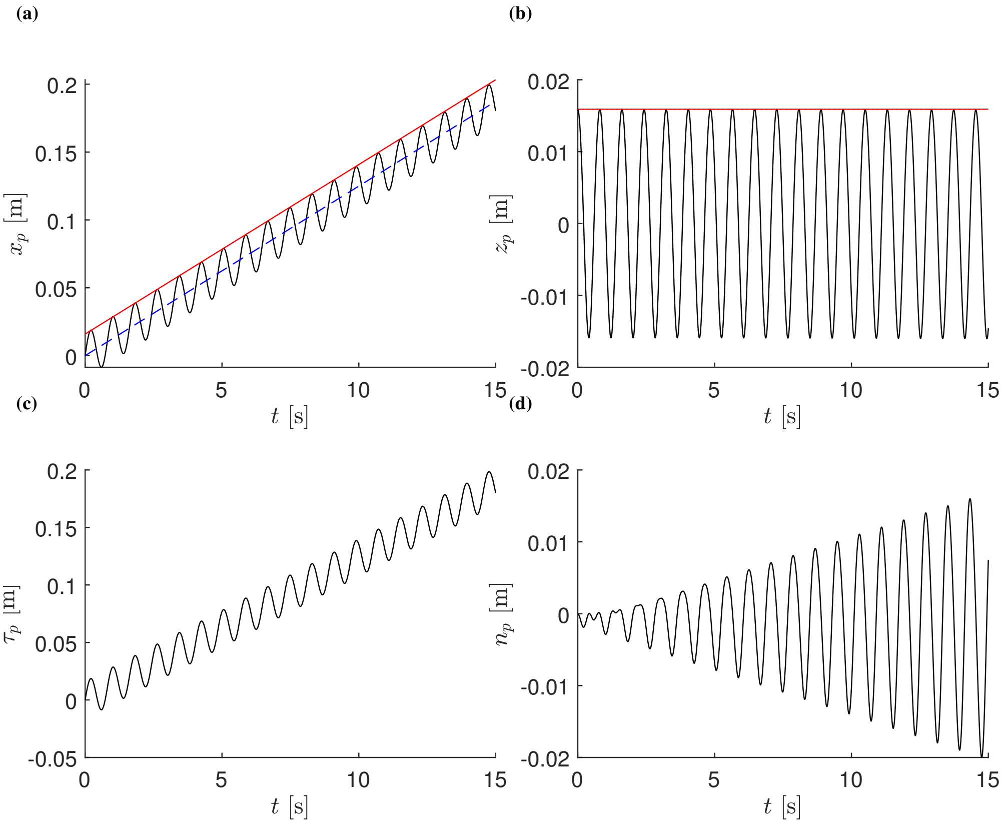

Figure 3.20: Trajectory of a perfectly Lagrangian tracer from numerical solution of our model with forcing provided by (3.48). The top two panels (a, b) display the horizontal and vertical motions $x_p(t)$ and $z_p(t)$ with the blue dashed line showing the theoretical Stokes drift displacement and the red lines the (superimposed) wave amplitudes. The bottom two panels (c, d) show the tracer particle positions in the (n, τ)-coordinate system.

Chapter 4

Conclusions and recommendations

4.1 Conclusions

4.1.1 General conclusions

Wave-induced transport of material in the ocean is highly important from environmental (e.g. microplastic pollution, sediment movement) and societal (searches for survivors of marine disasters, wreckage) perspectives. This thesis has presented advanced theoretical and experimental studies of the motions of particles by waves. Two categories of particles have been considered: tracers, which are small particles with the same density as water; and inertial particles, which are larger and may have different density to water. The detailed findings are summarised below.

4.1.2 Stokes drift and Eulerian mean flow under deep-water wave packets

A laboratory-based experimental study of Lagrangian trajectories underneath uni-directional, deep-water (Chapter 1) to intermediate-depth (Chapter 2) surface gravity wave packets demonstrated visually wave-induced Eulerian return flows and Stokes drifts. Observations of quasi-monochromatic, small-amplitude, non-breaking waves were in close agreement with leading-order solutions to the irrotational water wave equations. Stokes drift for groups has both a horizontal and a vertical component; the former results in a net displacement, whereas the latter causes a temporary positive set-up for particles located a small distance below the centre of a group, defined by a 'transition' depth. Such non-zero vertical Stokes drift is contentious when examining equations of the Craik and Leibovich [1976] type [McWilliams, 2016, Mellor, 2016], but has been predicted to affect Lagrangian buoy records [Herbers and Janssen, 2016, McAllister and van den Bremer, 2019]. For relatively short, quasi-monochromatic groups, the boundary layers do not have sufficient time to develop, and so streaming of Lagrangian particles [Long, 1953, Grue and Kolaas, 2017] does not occur. Short, quasi-monochromatic groups avoid set-up in a closed-flume return flow associated with periodic waves, which may transport vorticity, be difficult to control experimentally and could account for some of the confusion in the literature.

4.1.3 Extension to arbitrary depth

Using perturbation methods, an analytical solution has been established for wave-induced Eulerian return flow under arbitrary-depth wave packets. The solution generalises previous analytical solutions in the existing literature, which had assumed either shallow return flow or deep return flow. This allows seamless modelling of the return flow from the deep ocean to continental shelf.

Previous work by van den Bremer and Taylor [2015] has been extended by carefully examining the order in bandwidth of the set-down of finite-depth wave packets. The analysis introduces an extra term, analogous to flow through a convergent-divergent duct bounded by the set-down, which promotes a higher magnitude return flow as the set-down increases.

The theoretical analysis suggests that a wave-induced mean drift should be observable in experimental wave flumes (see Monismith et al. [2007], Grue and Kolaas [2017], van den Bremer and Breivik [2017] for discussions) with contributions from Stokes drift and Eulerian return flow. The displacement arising from Stokes drift is in the direction of wave propagation and decays with depth, whilst the displacement from the Eulerian return flow is constant with depth, thus equally affecting tracers at the surface or at depth.

A method has been established for extracting mean flows from wave-flume experiments using finite-depth wave packets without full second-order wave generation. In practice, difficulty arises from the error wave travelling at a similar speed to the wave packet, thus taking a long time to separate. The method utilises narrow-banded properties of quasi-monochromatic wave packets in removing erroneous error-wave and background motion.

The enhanced Eulerian return flow is likely to be largest in finite-depth coastal waters where the set-down is significant. Correct calculation of the Eulerian mean flow would improve the accuracy of estimates of particle transport in the coastal zone, by better representing the total wave-induced transport, particularly its dependence on depth. This is particularly important because the return flow displacement is in the opposite direction to the depth-decaying Stokes drift displacement, whilst being constant with depth.

4.1.4 Mechanism for the increased transport of large floating marine debris

An equation of motion has been derived (Chapter 3) for spherical inertial finite-sized floating marine debris, which uses a moving coordinate system that aligns with the free surface.

Physical mechanisms for increased drift of larger floating marine debris have been identified through a Stokes-like expansion of the equation of motion using viscous drag. The closed-form solution correctly reproduces results from numerical simulations of the equations when viscous drag is included. Both numerical and analytical solutions recover the Lagrangian limit as the object size tends to zero.

Two mechanisms have been suggested for the increased drift: the first is the change in magnitude of the linear orbits, and; the second is an out-of-phase variable submergence response resolved into the horizontal direction by the slope of the free surface. The second mechanism requires buoyancy to be modelled in a the direction normal to the free surface, with drag implemented in the same direction; the resulting component has a wave-averaged mean when multiplied by the slope of the free surface.

Laboratory wave flume experiments were carried out for a range of spherical object sizes and densities. The results show a similar trend with object size to numerical simulations using quadratic drag, but no discernible trend with density. This is likely due to the imperfect manufacturing of the objects, difficulty in controlling air flows, initial motion of the object, and potential inertia at packet scale. The theoretical predictions provided a satisfactory match to the experimental measurements without need for fitting parameters.

The experimental and numerical models considered in this thesis are both at laboratory scale, where a significant increase in drift is observed. The main driver for this increased drift is the object size relative to the wavelength. Thus, in the real ocean, where wavelengths range from $10-1000$ m, the increased drift effect will only be observable where shorter wavelengths are present, such as in gulfs or small seas; for example, in regular waves of wavelength 40 m, corresponding to the peak wind wave frequency [Toffoli and Bitner-Gregersen, 2017], a 1 m diameter object of density 950 kg/m^3 would experience an increased drift of 33%.

4.2 Impact of research

The experimental observations and analytical solution of wave-induced transport under wave packets presented in this thesis have validated the physical existence of Stokes drift almost two centuries after Stokes [1847] first derived the transport associated with waves [Monismith, 2020].

The closed-form parametric equation, which accounts for the effects of an objects inertia on its transport, could be implemented in larger ocean-scale models, such as that of Van Sebille et al. [2018]. The case for using wave model data, such as from WAVEWATCH III [Tolman et al., 2009], instead of assuming Stokes drift is proportional to wind forcing, to calculate the wave field and Stokes drift has been strengthened.

Differential transport due to size and inertia could lead to sorting of plastic particulate material in the ocean. This may provide an additional explanation for the distributions observed by Isobe et al. [2014], Kataoka and Akylas [2015], where smaller plastic was more likely to be offshore, compared with larger plastic onshore.

4.3 Recommendations for future work

Suggestions for future research are listed below:

- Theoretical modelling of the Eulerian return flow under wave packets in three dimensions using perturbation methods, allowing for an additional width of the group in the orthogonal direction to the wave propagation.

- Extension of the solution to Eulerian return flow under wave packets to include a sloping bottom boundary condition. Allowing the bottom boundary to change on the scale of the group would increase the applications where the model is valid, specifically closer to the shore.

- Experimental and theoretical investigation into the effect of combing currents with wave packets on the Eulerian return flow. Initially with the current orientated in the same direction as the wave propagation, then at an angle in three dimensions. Examining interactions that may lead to changes in return flow.

- Numerical and analytical modelling of different shaped inertial objects under wave action. Initially using spheroids, which can represent discs and rods, to examine the change in wave-induced transport. The drag will need special attention to get the correct result, which may require experimental modelling.

- Carry out larger-scale experimental modelling of the wave-induced drift of inertial objects in a large basin facility. Using objects with more uniform density distribution to reduce error bars and proceeding to test realistic ocean debris to examine the validity of the theoretical shape assumptions.

- Include wind and current forcing into the model of inertial floating marine debris. This would allow the balance between wind forcing and water forcing to be examined, which is of particular interest as objects become less dense and thus, more of the object is out of the water.

References

A. L. Andrady. Microplastics in the marine environment. *Mar. poll. Bull.*, 62 (8):1596–1605, 2011.

D. G. Andrews and M. E. McIntyre. An exact theory of nonlinear waves on a Lagrangian-mean flow. *J. Fluid Mech.*, 89:609–646, 1978.

F. Ardhuin, B. Chapron, and T. Elfouhaily. Waves and the air–sea momentum budget: Implications for ocean circulation modeling. *J. phys. oceanogr.*, 34 (7):1741–1755, 2004.

F. Ardhuin, A. D. Jenkins, D. Hauser, A. Reniers, and B. Chapron. Waves and operational oceanography: toward a coherent description of the upper ocean. *Eos Trans. American Geophys. Union*, 86(4):37–40, 2005.

F. Ardhuin, P. Brandt, L. Gaultier, C. Donlon, A. Battaglia, F. Boy, T. Casal, B. Chapron, F. Collard, S. Cravatte, et al. SKIM, a candidate satellite mission exploring global ocean currents and waves. *Front. Mar. Sci.*, 6, 2019.

R. A. Bagnold. Sand movement by waves: some small-scale experiments with sand of very low density. *J. Inst. Civil Engng.*, 27(4):447–469, 1947.

S. E. Belcher, A. L. M. Grant, K. E. Hanley, B. Fox-Kemper, L. Van Roekel, P. P. Sullivan, W. G. Large, A. Brown Andy, A. Hines, D. Calvert, A. Rutgersson, H. Pettersson, J. R. Bidlot, P. A. E. M. Janssen, and J. A. Polton. A global perspective on Langmuir turbulence in the ocean surface boundary layer. *Geophys. Res. Lett.*, 39(18), 2012.

O. Breivik, J. Bidlot, and P. A. E. M. Janssen. Approximate Stokes drift profiles in deep water. *J. Phys. Oceanogr.*, 44:2433–2445, 2014.

P. U. Brinch-Nielsen and I. G. Jonsson. Fourth order evolution-equations and stability analysis for Stokes waves on arbitrary water depth. *Wave Motion*, 8(455), 1986.

O. Bühler. *Waves and Mean Flows*. Cambridge University Press, Cambridge, UK, 2nd edition, 2014.

R. Calvert, C. Whittaker, A. Raby, P.H. Taylor, A.G.L. Borthwick, and T. S. van den Bremer. Laboratory study of the wave-induced mean flow and set-down in unidirectional surface gravity wave packets on finite water depth. *Phys. Rev. Fluids*, 4(11):114801, 2019.

K. H. Christensen and E. Terrile. Drift and deformation of oil slicks due to surface waves. *J. Fluid Mech.*, 620:313–332, 2009. doi: 10.1017/S0022112008004606.

M. Cole, P. Lindeque, C. Halsband, and T. S. Galloway. Microplastics as contaminants in the marine environment: a review. *Mar. Pollut. Bull*, 62 (12):2588–2597, 2011.

A. Cózar, F. Echevarrí, J. I. González-Gordillo, X. Irigoien, B. Úbeda, S. Hernández-León, Á. T. Palma, S. Navarro, J. García de Lomas, A. Ruiz, et al. Plastic debris in the open ocean. *P. Natl. Acad. Sci.*, 111(28):10239–10244, 2014.

A. D. D. Craik and S. Leibovich. A rational model for Langmuir circulations. *J. Fluid Mech.*, 73(3):401–426, 1976. doi: 10.1017/S0022112076001420.

J. R. Dalzell. A note on finite depth second-order wave-wave interactions. *Appl. Ocean Res.*, 21:105–111, 1999.

E. A. D'Asaro, J. Thomson, A. Y. Shcherbina, R. R. Harcourt, M. F. Cronin, M. A. Hemer, and B. Fox-Kemper. Quantifying upper ocean turbulence driven by surface waves. *Geophys. Res. Lett.*, 41(1):102–107, 1 2014. doi: 10.1002/2013GL058193.

A. Davey and K. Stewartson. On three dimensional packets of surface waves. *Proc. Roy. Soc. A*, 338:101–110, 1975.

R. Deigaard et al. *Mechanics of coastal sediment transport*, volume 3. World Scientific Publishing Company, 1992.

L. Deike, N. Pizzo, and W. K. Melville. Lagrangian transport by breaking surface waves. *J. Fluid Mech.*, 829:364–391, 2017.

P. Delandmeter and E. Van Sebille. The Parcels v2. 0 Lagrangian framework: new field interpolation schemes. *Geosci. Model Dev.*, 12(8):3571–3584, 2019.

M. H. DiBenedetto and N. T. Ouellette. Preferential orientation of spheroidal particles in wavy flow. *J. Fluid Mech.*, 856:850–869, 2018a.

M. H. DiBenedetto and N. T. Ouellette. Preferential orientation of spheroidal particles in wavy flow. *J. Fluid Mech.*, 856:850–869, 2018b.

M. H. DiBenedetto, N. T. Ouellette, and J. R. Koseff. Transport of anisotropic particles under waves. *J. Fluid Mech.*, 837:320–340, 2018.

M. H. DiBenedetto, J. R. Koseff, and N. T. Ouellette. Orientation dynamics of nonspherical particles under surface gravity waves. *Phys. Rev. Fluids*, 4: 034301, 2019.

D. Dobler, T. Huck, C. Maes, N. Grima, B. Blanke, E. Martinez, and F. Ardhuin. Large impact of Stokes drift on the fate of surface floating debris in the South Indian Basin. *Mar. Pollut. Bull.*, 148:202–209, 2019.

M. Drivdal, G. G. Broström, and K. H. Christensen. Wave-induced mixing and transport of buoyant particles: application to the Statfjord A oil spill. *Ocean Science*, 10(6):977–991, 2014. doi: 10.5194/os-10-977-2014.

K. B. Dysthe. Note on a modification to the nonlinear Schrödinger equation for application to deep water waves. *Proc. R. Soc. Lond. A*, 369:105–114, 1979.

I. Eames. Settling of particles beneath water waves. *J. Phys. Oceanogr.*, 38: 2846–2853, 2008.

M. Eriksen, L. C. M. Lebreton, H. S. Carson, M. Thiel, C. J. Moore, J. C. Borerro, F. Galgani, P. G. Ryan, and J. Reisser. Plastic pollution in the world's oceans: more than 5 trillion plastic pieces weighing over 250,000 tons afloat at sea. *PloS ONE*, 9(12):e111913, 2014.

G.Z. Forristall. Wave crest distributions: Observations and second-order theory. *J. Phys. Oceanogr.*, 30:1931–1943, 2000.

C. I. Fraser, A. K. Morrison, A. McC Hogg, E. C. Macaya, E. van Sebille, P. G. Ryan, A. Padovan, C. Jack, N. Valdivia, and J. M. Waters. Antarctica's ecological isolation will be broken by storm-driven dispersal and warming. *Nat. Clim. Change*, 8(8):704–708, 2018.

A. G. Fujimura, A. J. H. M. Reniers, C. B. Paris, A. L. Shanks, J. H. MacMahan, and S. G. Morgan. Numerical simulations of larval transport into a rip-channeled surf zone. *Limnol. and Oceanogr.*, 59(4):1434–1447, 2014.

R. Geyer, J. R. Jambeck, and K. L. Law. Production, use, and fate of all plastics ever made. *Sci. Adv.*, 3(7):e1700782, 2017.

M. C. Goldstein, M. Rosenberg, and L. Cheng. Increased oceanic microplastic debris enhances oviposition in an endemic pelagic insect. *Biol. Lett.*, 8(5): 817–820, 2012.

J. Groeneweg and G. Klopman. Changes of the mean velocity profiles in the combined wave-current motion described in a GLM formulation. *J. Fluid Mech.*, 370:271–269, 1998.

J. Grue and J. Kolaas. Experimental particle paths and drift velocity in steep waves at finite water depth. *J. Fluid Mech.*, 810:R1, 2017.

S. Haney, B. Fox-Kemper, K. Julien, and A. Webb. Symmetric and geostrophic instabilities in the wave-forced ocean mixed layer. *J. Phys. Oceanogr.*, 45(12): 3033–3056., 2015.

K. E. Hanley, S. E. Belcher, and P. P. Sullivan. A global climatology of wind–wave interaction. *J. Phys. Oceanogr.*, 40(6):1263–1282, 2010.

K. Hasselmann. On the non-linear energy transfer in a gravity wave spectrum. Part 1. *J. Fluid Mech.*, 12:481–500, 1962.

T. H. C. Herbers and T. T. Janssen. Lagrangian surface wave motion and Stokes drift fluctuations. *J. Phys. Oceonogr.*, 46(4):1009–1021, 2016.

G. Huang, Z. H. Huang, and A. W. K. Law. Analytical study on drift of small floating objects under regular waves. *J. Eng. Mech.-ASCE*, 142(6):06016002, 2016. doi: 10.1061/(ASCE)EM.1943-7889.0001067.

A. Isobe, K. Kubo, Y. Tamura, E. Nakashima, N. Fujii, et al. Selective transport of microplastics and mesoplastics by drifting in coastal waters. *Mar. Pollut. Bull*, 89(1):324–330, 2014.

S. Iwasaki, A. Isobe, S. Kako, K. Uchida, and T. Tokai. Fate of microplastics and mesoplastics carried by surface currents and wind waves: A numerical model approach in the Sea of Japan. *Mar. Pollut. Bull.*, 121(1-2):85–96, 2017.

J. R. Jambeck, R. Geyer, C. Wilcox, T. R. Siegler, M. Perryman, A. Andrady, R. Narayan, and K. L. Law. Plastic waste inputs from land into the ocean. *Science*, 347(6223):768–771, 2015.

C. E. Jones, K. Dagestad, Ø. Breivik, B. Holt, J. Röhrshrs, K. Christensen, M. Espeseth, C. Brekke, and S. Skrunes. Measurement and modelling of oil slick transport. *J. Geophys. Res.*, 121(10):7759–7775, 2016.

T. Kataoka and T. R. Akylas. On three-dimensional internal gravity wave beams and induced large-scale mean flows. *J. Fluid Mech.*, 769:621–634, 2015.

T. Kataoka and H. Hinata. Evaluation of beach cleanup effects using linear system analysis. *Mar. poll. bull.*, 91(1):73–81, 2015.

M. Kubota. A mechanism for the accumulation of floating marine debris north of Hawaii. *J. Phys. Oceanogr.*, 24(5):1059–1064, 1994.

K. L. Law. Plastics in the marine environment. *Annul. Rev. of Mar. Sci.*, 9: 205–229, 2017.

L. Lebreton, B. Slat, F. Ferrari, B. Sainte-Rose, J. Aitken, R. Marthouse, S. Hajbane, S. Cunsolo, A. Schwarz, A. Levivier, K. Noble, P. Debeljak, H. Maral, R. Schoeneich-Argent, R. Brambini, and J. Reisser. Evidence that the Great Pacific Garbage Patch is rapidly accumulating plastic. *Scientific Reports*, 8:4666, 2018.

L. Lebreton, M. Egger, and B. Slat. A global mass budget for positively buoyant macroplastic debris in the ocean. *Sci. Rep.*, 9(1):1–10, 2019.

P. J. Van Leeuwen and G. Klopman. A new method for the generation of second-order random waves. *Ocean Eng.*, 23(2):167–192, 1996.

S. Liubartseva, G. Coppini, R. Lecci, and E. Clementi. Tracking plastics in the Mediterranean: 2D Lagrangian model. *Mar. Pollut. Bull.*, 129(1):151–162, 2018.

R. R. Long. Some aspects of the flow of stratified fluids. a theoretical investigation. *Tellus*, 5:42–58, 1953.

M. S. Longuet-Higgins. The statistical analysis of a random, moving surface. *Phil. Trans. R. Soc. Lond. A*, 249(966):321–387, 1957.

M. S. Longuet-Higgins. A nonlinear mechanism for the generation of sea waves. *Proc. Roy. Soc. of Lond. A.*, 311(1506):371–389, 1969.

M. S. Longuet-Higgins and R.W. Stewart. Radiation stress and mass transport in gravity waves, with application to 'surf beats'. *J. Fluid Mech.*, 13:481–504, 1962a.

M.S. Longuet-Higgins. Mass transport in water waves. *Phil. Trans. R. Soc. Lond. A*, 245:535–581, 1953.

M.S. Longuet-Higgins and R.W. Stewart. Radiation stress and mass transport in gravity waves, with applications to 'surf beats'. *J. Fluid Mech.*, 13:481–504, 1962b.

M.S. Longuet-Higgins and R.W. Stewart. Radiation stresses in water waves; a physical discussion, with applications. *Deep-Sea Res.*, 2:529–562, 1964.

J. MacMahan, J. Brown, J. Brown, E. Thornton, A. Reniers, T. Stanton, M. Henriquez, E. Gallagher, J. Morrison, M. J. Austin, et al. Mean Lagrangian flow behavior on an open coast rip-channeled beach: A new perspective. *Mar. Geol.*, 268(1-4):1–15, 2010.

M. R. Maxey and J. J. Riley. Equation of motion for a small rigid sphere in a non-uniform flow. *Phys. Fluids*, 26(4):883–889, 1983.

M. L. McAllister and T. S. van den Bremer. Lagrangian Measurement of Steep Directionally Spread Ocean Waves: Second-Order Motion of a Wave-Following Measurement Buoy. *Journal of Physical Oceanography*, 49(12): 3087–3108, 12 2019. ISSN 0022-3670.

M. L. McAllister, T. A. A. Adcock, P. H. Taylor, and T. S. van den Bremer. The set-down and set-up of directionally spread and crossing surface gravity wave groups. *J. Fluid Mech.*, 835:131–169, 2018.

M. E. McIntyre. On the wave momentum myth. *J. Fluid Mech.*, 106:331–347, 1981.

M. E. McIntyre. A note on the divergence effect and the Lagrangian-mean surface elevation in periodic water waves. *J. Fluid Mech.*, 189:235–242, 1988.

J. C. McWilliams. Submesoscale currents in the ocean. *Proc. R. Soc. Lond. A*, 472:2189, 2016.

J. C. McWilliams and J.M. Restrepo. The wave-driven ocean circulation. *J. Phys. Oceanogr.*, 29:2523–2540, 1999.

J. C. McWilliams, J. M. Restrepo, and E. M. Lane. An asymptotic theory for the interaction of waves and currents in coastal waters. *J. Fluid Mech.*, 511: 135–178, 2004.

C. C. Mei, P. L. F. Liu, and T. G. Carter. Mass transport in water waves. Technical Report 146, MIT Rep. Ralph M. Parsons Lab. Water Resour. Hydrodynamics, 1972.

C. C. Mei, M. Stiassnie, and D. K.-P. Yue. *Theory and Applications of Ocean Surface Waves: part 2: Nonlinear Aspects.* World Scientific, 1989.

G. Mellor. On theories dealing with the interaction of surface waves and ocean circulation. *J. Geophys. Res. Oceans*, 121:4474–4486, 2016.

W. K. Melville and R. Rapp. The surface velocity field in steep and breaking waves. *J. Fluid Mech.*, 189:1–22, 1988.

S. Monismith. Stokes drift: Theory and experiments. *J. Fluid Mech.*, 884:F1, 2020.

S. G. Monismith, E.A. Cowen, H. M. Nepf, J. Magnaudet, and L. Thais. Laboratory observations of mean flows under surface gravity waves. *J. Fluid Mech.*, 573:131–147, 2007.

F. A. Morrison. *An introduction to fluid mechanics.* Cambridge University Press, 2013.

P. Nielsen. *Coastal bottom boundary layers and sediment transport*, volume 4. World Scientific Publishing Company, 1992.

P. Nielsen and T. Baldock. И-shaped surf beat understood in terms of transient forced long waves. *Coast. Eng.*, 57, 01 2010.

R. Nokes. *Streams 2.02: System theory and design.* University of Canterbury, Canterbury, New Zealand, 2014.

M. Okihiro, R.T. Guza, and R.J. Seymour. Bound infra-gravity waves. *J. Geophys. Res.*, 97:453–469, 1992.

V. Onink, D. Wichmann, P. Delandmeter, and E. Van Sebille. The role of Ekman currents, geostrophy, and Stokes drift in the accumulation of floating microplastic. *J. Geophys. Res.-Oceans*, 124(3):1474–1490, 2019.

J. Orszaghova, P. H. Taylor, A. G. L. Borthwick, and A. C. Raby. Importance of second-order wave generation for focused wave group run-up and overtopping. *Coast. Eng.*, 94:63–79, 2014.

C. Ostle, R. C. Thompson, D. Broughton, L. Gregory, M. Wootton, and D. G. Johns. The rise in ocean plastics evidenced from a 60-year time series. *Nat. Commun.*, 10(1):1–6, 2019.

M. Paprota, W. Sulisz, and A. Reda. Experimental study of wave-induced mass transport. *J. Hydraul. Res.*, 54(4):423–434, 2016.

G. Pasternak, D. Zviely, A. Ariel, E. Spanier, and C. A. Ribic. Message in a bottle–the story of floating plastic in the Eastern Mediterranean sea. *Waste Manage.*, 77:67–77, 2018.

L. Pellet, P. Christodoulides, S. Donne, C.J. Bean, and F. Dias. Pressure induced by the interaction of water waves with nearly equal frequencies and nearly opposite directions. *Ther. Appl. Mech. Lett.*, 2017.

D. H. Peregrine. Water waves, nonlinear Schrödinger equations and their solutions. *J. Aust. Math Soc.*, 25:16–43, 1983.

N. Pizzo and W. Melville. Vortex generation by deep-water breaking waves. *J. Fluid. Mech.*, 734(198-218), 2013.

N. E. Pizzo. Surfing surface gravity waves. *J. Fluid Mech.*, 823:316–328, 2017.

J. M. Restrepo and J. M. Ramirez. Transport due to transient progressive waves. *J. Phys. Oceanogr.*, 49(9):2323–2336, 2019.

J. Röhrs, K. H. Christensen, L. R. Hole, G. Broström, M. Drivdal, and S. Sundby. Observation-based evaluation of surface wave effects on currents and trajectory forecasts. *Ocean Dynam.*, 62(10):1519–1533, 2012.

R. R. Rumer, R. D. Crissman, and A. Wake. *Ice transport in great lakes.* Great Lakes Environmental Research Laboratory, National Oceanic and . . . , 1979.

F. Santamaria, F. Boffetta, M. Martins Afonso, A. Mazzino, M. Onorato, and D. Pugliese. Stokes drift for inertial particles transported by water waves. *Europhys. Lett.*, 102(1):14003, 2013.

H. A. Schäffer. Second-order wavemaker theory for irregular waves. *Ocean Eng.*, 23:47–88, 1996.

J. Sharma and R. G. Dean. Second-order directional seas and associated wave forces. *Proc. Offshore Tech. Conf.*, 4:2505–2514, 1981.

H. H. Shen and Y. Zhong. Theoretical study of drift of small rigid floating objects in wave fields. *J.waterw. Port C-ASCE*, 127(6):343–351, 2001.

P. Sherman and E. Van Sebille. Modeling marine surface microplastic transport to assess optimal removal locations. *Environ. Res. Lett.*, 11(1):014006, 2016.

J. A. Smith. Observed variability of ocean wave Stokes drift, and the Eulerian response to passing groups. *J. Phys. Oceanogr.*, 36:1381–1402, 2006.

V. Sriram, T. Schlurmann, and S. Schimmels. Focused wave evolution using linear and second order wavemaker theory. *Appl. Ocean Res.*, 53:279–296, 2015.

G. G. Stokes. On the theory of oscillatory waves. *Trans. Camb. Philos. Soc.*, 8:441–455, 1847.

P. P. Sullivan and J. C. McWilliams. Dynamics of winds and currents coupled to surface waves. *Annu. Rev. Fluid Mech.*, 42:19–42, 2010.

I. A. Svendsen. Mass flux and undertow in a surf zone. *Coast. Eng.*, 8(4): 347 – 365, 1984. ISSN 0378-3839. doi: http://dx.doi.org/10.1016/0378-3839(84)90030-9.

C. Swan. Convection within an experimental wave flume. *J. Hydraul. Res.*, 28: 273–282, 1990.

C. Swan and J. F. A. Sleath. A second approximation to the time-mean Lagrangian drift beneath progressive gravity waves. *Ocean Eng.*, 1:65–79, 1990.

The WAVEWATCH III ® Development Group. User manual and system documentation of WAVEWATCH III ® version 5.16. Tech. Note 329, NOAA/NWS/NCEP/MMAB, 2016. 326 pp. + Appendices.

A. Toffoli and E. M. Bitner-Gregersen. *Types of ocean surface waves, wave classification*, pages 1–8. Wiley Online Library, 2017.

Hendrik L Tolman et al. User manual and system documentation of WAVEWATCH III TM version 3.14. Technical Report 276, MMAB/NCEP/NOAA, 2009.

J. A. Trinanes, M. J. Olascoaga, G. J. Goni, N. A. Maximenko, D. A. Griffin, and J. Hafner. Analysis of flight MH370 potential debris trajectories using ocean observations and numerical model results. *J. Oper. Oceanogr.*, 9(2): 126–138, 2016.

M. Umeyama. Eulerian-Lagrangian analysis for particle velocities and trajectories in a pure wave motion using particle image velocimetry. *Phil. Trans. R. Soc. A*, 370(1964):1687–1702, 2012.

T. S. van den Bremer and Ø. Breivik. Stokes drift. *Phil. Trans. R. Soc. Lond. A*, 376:20170104., 2017.

T. S. van den Bremer and P. H. Taylor. Estimates of Lagrangian transport by surface gravity wave groups: the effects of finite depth and directionality. *J. Geophys. Res.*, 120(4):2701–2722, 2015.

T. S. van den Bremer and P. H. Taylor. Lagrangian transport for two-dimensional deep-water surface gravity wave groups. *Proc. R. Soc. A*, 472 (20160159), 2016.

T. S. Van Den Bremer, C. Whittaker, R. Calvert, A. Raby, and P.H. Taylor. Experimental study of particle trajectories below deep-water surface gravity wave groups. *J. Fluid Mech.*, 879:168–186, 2019.

T. S. van den Bremer, H. Yassin, and B. R. Sutherland. Lagrangian transport by vertically confined internal gravity wavepackets. *J. Fluid Mech.*, 864: 348–380, 2019.

T. S. van den Bremer, C. Whittaker, R. Calvert, A. Raby, and P. H. Taylor. Experimental study of particle trajectories below deep-water surface gravity wave groups. *J. Fluid Mech.*, under review.

M. van Dyke. *An album of fluid motion.* The Parabolic Press, Stanford, USA, 1982.

E. Van Sebille, S. M. Griffies, R. Abernathey, T. P. Adams, P. Berloff, A. Biastoch, B. Blanke, E. P. Chassignet, Y. Cheng, C. J. Cotter, E. Deleersnijder, K. Döös, H. F. Drake, S. Drijfhout, S. G. Gary, A W. Heemink, J. Kjellsson, I. M. Koszalka, M. Lange, C. Lique, G. A. MacGilchrist, R. Marsh, C. G. Mayorga Adame, R. McAdam, F. Nencioli, C. B. Paris, M. D. Piggott, J. A. Polton, S. Rühs, S. A.A.M Shah, M. D. Thomas, J. Wang, P. J. Wolfram, L. Zanna, and J. D Zika. Lagrangian ocean analysis: Fundamentals and practices. *Ocean Model.*, 121:49–75, 2018.

E. van Sebille, S. Aliani, K. Lavender Law, N. Maximenko, J. Alsina, M. Bergmann A. Bagaev, B. Chapron, I. Chubarenko, A. Cózar, P. Delandmeter, M. Egger, B. Fox-Kemper, S. Pascal Garaba, L. Goddijn-Murphy, D. Hardesty, M. Hoffman, A. Isobe, C. Jongedijk, M. Kaandorp, L. Khatmullina, A. A. Koelmans, T. Kukulka, C. Laufkötter, L. Lebreton, D. Lobelle, C. Maes, V. Martinez-Vicente, M. A. Morales Maqueda, M. Poulain-Zarcos, E. Rodriguez, P. G. Ryan, A. Shanks, W. J. Shim, G. Suaria, T. S. van den Bremer M. Thiel, and D. Wichmann. The physical oceanography of the transport of floating marine debris. *Environ. Res. Lett.*, 15(2):023003, 2020.

Erik van Sebille, Chris Wilcox, Laurent Lebreton, Nikolai Maximenko, Britta Denise Hardesty, Jan A van Franeker, Marcus Eriksen, David Siegel, Francois Galgani, and Kara Lavender Law. A global inventory of small floating plastic debris. *Environ Res Lett*, 10(12):124006, 2015. doi: 10.1088/1748-9326/10/12/124006.

A. Wallet and F. Ruellan. *Houille Blanche*, 5:483–489, 1950.

A Webb and B Fox-Kemper. Wave spectral moments and Stokes drift estimation. *Ocean Model*, 40:273–288, 2011. doi: 10.1016/j.ocemod.2011.08.007.

A. Webb and B. Fox-Kemper. Impacts of wave spreading and multidirectional waves on estimating Stokes drift. *Ocean Model.*, 96:49–64, 2015.

J. E. Weber. Attenuated wave-induced drift in a viscous rotating ocean. *J. Fluid Mech.*, 137:115–129, 1983.

J. E Weber and E. Førland. Effect of the air on the drift velocity of water waves. *J.Fluid Mech.*, 218:619–640, 1990.

J. E. Weber and O. Saetra. Effect of film elasticity on the drift velocity of capillary–gravity waves. *Phys. Fluids*, 7(2):307–314, 1995.

J. E. H. Weber. Do we observe Gerstner waves in wave tank experiments? *Wave Motion*, 48(4):301–309, 2011.

C. N. Whittaker, C. J. Fitzgerald, A. C. Raby, P. H. Taylor, J. Orszaghova, and A. G.L. Borthwick. Optimisation of focused wave group runup on a plane beach. *Coast. Eng.*, 121:44–55, 2017.

C. Wilcox, B. D. Hardesty, and K. L. Law. Abundance of floating plastic particles is increasing in the western North Atlantic Ocean. *Environ. Sci. Tech.*, 54(2):790–796, 2019.